NUREG/CR-1851
SAND80-0764
AN
Printed February 1982

Reactor-Physics Design Calculations for the ACPR Upgrade

Paul S. Pickard, Jay P. Odom

Prepared by
Sandia National Laboratories
Albuquerque, New Mexico 87185 and Livermore, California 94550
for the United States Department of Energy
under Contract DE-AC04-76DP00789

Prepared for
U. S. NUCLEAR REGULATORY COMMISSION

Available from
GPO Sales Program
Division of Technical Information and Document Control
U.S. Nuclear Regulatory Commission
Washington, D.C. 20555

and

National Technical Information Service
Springfield, Virginia 22161

NUREG/CR--1851

DE82 016737

NUREG/CR-1851
SAND80-0764
AN

REACTOR-PHYSICS DESIGN CALCULATIONS FOR THE ACPR UPGRADE

P. S. Pickard and J. P. Odom

Sandia National Laboratories
Albuquerque, New Mexico 87185
operated by
Sandia Corporation
for the
U. S. Department of Energy

Manuscript Submitted: December 1981
Date Published: March 1982

Prepared for
Division of Accident Evaluation
Office of Nuclear Regulatory Research
U. S. Nuclear Regulatory Commission
Washington, DC 20555
Under Memorandum of Understanding DOE 40-550-75
NRC FIN No. A1032

CONTENTS

CONTENTS--cont'd.

FIGURES

TABLES

1. REACTOR PHYSICS DESIGN CALCULATIONS FOR THE ACPR UPGRADE

1.1 Introduction

This report describes the reactor physics calculations performed for the upgrade of the Annular Core Pulse Reactor (ACPR).[1] The ACPR has been in operation since 1967 and has been utilized for a variety of simulation and reactor safety experiments involving both transient and steady-state operations. The limitation in performing such experiments in the ACPR has been the degree to which realistic reactor safety and nuclear effects simulation conditions could be created. The motivation for the ACPR Upgrade was to increase pulse and steady-state performance with a sufficiently harder neutron energy spectrum to allow a wider range of tests to be performed.

1.2 Original ACPR Capabilities

In the pulse mode the original ACPR operated with initial periods as short as 1.3 msec with a FWHM of 4.5 msec, and a total neutron fluence in the central irradiation cavity of 2.0×10^{15} n/cm^2 for a maximum pulse. In the steady-state mode, the reactor operated at 600 kW (1.2×10^{13} n/cm-sec). The performance and description of the original ACPR is summarized in Table 1.2-1. In this configuration, the ACPR was utilized for a variety of nuclear weapons-related and LMFBR safety experiments. Prompt burst energetics (PBE) tests on single-pin geometries were performed with energy depositions in 20 percent enriched UO_2 approaching 3000 J/g in suitably moderated samples with non-prototypic surface/centerline depression ratios in the range of 1.6-1.8, depending on the containment used. Post-accident heat removal studies utilizing intrinsic fission heating of debris beds or molten pools to simulate decay heat were performed at powers up to approximately 1.0 percent of prototypic average operating fuel powers. Fuel coolant interaction studies (FCI) and effective equation-of-state experiments (EEOS) were also initiated.

Although a considerable range of simulation and safety experiments could be performed in the original ACPR, the relatively soft spectrum and relatively low neutron fluence effectively limited PBE tests to single-pin geometries. When multi-pin geometries were considered, strong self-shielding effects in enriched samples produced severe non-prototypic heating profiles. An increase in the total pulse fluence and a significant hardening of the spectrum would be required in order to address the desired range of

TABLE 1.2-1

ACPR DESCRIPTION AND PERFORMANCE

Minimum Initial Period	1.3 msec
FWHM Maximum Pulse	4.5 msec
Peak Power Maximum Pulse	14,000 MW
Total Fluence	2.0×10^{15} n/cm^2
Maximum Temperature Rise in Fuel	900°C (550°C average)
Maximum Steady-State Power	600 KW (1.2×10^{13} n/cm^2 sec)
Fraction of Neutron Fluence above 10 keV	0.52
Fuel Elements	12 w/o U in U-$ZrH_{1.6}$ 20 percent enriched U Stainless steel 304 clad 15" active fuel length 156 fuel elements
Control Rods	6 fuel followed control rods 3 transient control rods

transient experiments in ACPR. The range of decay heat conditions of interest in PAHR studies extend well above the 1.0 percent of FFTF average operating power attainable with the current ACPR. An increase in the steady-state power level to 2MW would increase the decay heat simulation capability to greater than 3 percent, allowing more realistic simulation of decay heat conditions following a severe disruptive accident. EEOS and FCI experiments and nuclear effects simulation studies would similarly benefit from the more uniform deposition profiles and increased fluence available with an upgraded facility.

1.3 Objectives of the ACPR Upgrade

The performance objectives of the ACPR Upgrade project were the improvement of pulse fluence and steady-state flux. The goal set for the upgraded facility was to achieve a performance improvement factor of 2.6 times the original ACPR pulse fluence. It was also desired to obtain the pulse fluence improvement with the least possible degradation in the minimum reactor period and pulse width. The performance goal for steady-state power was an increase from 600 KW to 2 MW.[1]

1.4 ACPR Upgrade Core Concepts

Several potential approaches to ACPR performance improvement were identified in early studies. Only a brief summary of the basic features of the various approaches examined will be reported here. A complete summary of these preliminary studies is included in Reference 2.

The most straightforward approach to the upgrade was to utilize the U-$ZrH_{1.6}$ fuel in a larger more dilute fissile concentration core configuration. The advantages of this approach were a large negative temperature coefficient, the simplicity of a single region core design, and a possible reduction in the fuel development effort. Subsequent test programs did not confirm the latter advantage. The disadvantages were the very soft neutron energy spectrum and a relatively low performance improvement factor. Studies indicated that a factor of 1.5-1.7 might be achieved with peak adiabatic fuel temperatures of 1100-1200°C. This performance improvement was not acceptable, and the single region hydride core was not considered further.

The second approach, which received considerable attention, was the two-region core concept. The reactor core would consist of an inner region of high temperature, high heat capacity fuel, such as UO_2-BeO or UC-ZrC-C, capable of absorbing a large nuclear pulse, with a lower temperature outer U-$ZrH_{1.5}$ fueled region to provide an adequate negative temperature coefficient. This approach was evaluated in detail for several fuel enrichments and core configurations. The studies indicated that the UO_2-BeO/U-$ZrH_{1.5}$ system could achieve performance improvement factors

of 2.3-2.6 with less than 2 msec minimum periods, at peak temperatures of 1100-1400°C in the high heat capacity fuel. The UC-ZrC-C/U-$ZrH_{1.5}$ system was shown to have somewhat lower performance potential with maximum fuel temperature in the range of 2200°C.

The two region core approach had the advantage of maintaining a high negative temperature coefficient with a harder spectrum while approaching the desired performance level. The performance attainable depends on the allowable hydride fuel temperature which was assumed to be 1000°C for the two region core studies. The two region core has the disadvantages of requiring multiple fuel fabrication and development efforts for the complex core and the introducion high thermal stresses in the fuel at the two region interface.

The suitability of this approach for the ACPR Upgrade in the final analysis depended strongly on the attainable hydride fuel temperature. The fuels testing program indicated that the desired temperatures ($\simeq$ 1100°C) were probably not attainable routinely in the U-$ZrH_{1.5}$ fuel as presently fabricated.

The third core concept evaluated was a single region core utilizing the UO_2-BeO fuel. The advantages of this approach are in higher pulse fluence, reduced fuel stress, and core design simplicity. The primary concern with this approach was the pulse width attainable with the reduced negative temperature coefficient. The survey calculations performed to evaluate this approach were reported in Reference 3 and are summarized in Chapter 2. The results of this study showed that the use of lower enrichment fuel and non-moderating reflector elements allowed the dynamics of the single region system to compare favorably with the two

region cases. The UC-ZrC-C fuel material was not considered for the single region core due to a smaller negative temperature coefficient and the extremely high temperature required in the fuel to achieve performance goals.

The core design approaches summarized above were examined in detail by parameterizing fuel enrichment, core size and configuration. The single region core fueled with UO_2-BeO provided superior pulse performance, reduced operating fuel stress, allowed more overall core design flexibility, and was the most attractive design choice for the ACPR Upgrade. The pulse width for this system is larger than comparable two region core designs, but the increase was considered acceptable in comparison with the performance advantages.

1.5 Cross-Section Generation

The neutron cross sections generated for the ACPR Upgrade design studies used ENDF/B data processed by the AMPX code system.[4,5] The AMPX processor has the capability to perform resonance calculations, cell or spectral weighting, group collapsing and temperature dependent calculations. The majority of cross-section data was ENDF/B version III or IV. Low mass number nuclei, H, Be, and C were generated with the appropriate ENDF/B scattering kernals for water, beryllia, and graphite. Resonance calculations were included for all uranium isotopes at the appropriate temperatures using the Nordheim resonance routines in AMPX. Resonance calculations were also performed for cladding materials where appropriate.

All calculations were performed for each fuel composition and temperature, using a 1D S_N cell model. All cross-section sets were generated for three temperatures: 300, 900, and 1200 K. All cells were calculated using zero current conditions for both boundaries. Unique cell structures were not modeled for the fuel cells on boundaries or adjacent control elements. Cross sections utilized in the reflector and cavity regions were region (spectrally) weighted with a cell spectrum. The majority of the cross-section sets were generated in a 9-group format, with some sets generated in an 18-group format for comparison purposes. The group energy structure is given in Table 1.5-1.

TABLE 1.5-1

Cell Calculation Group Structure

9-Group Set

Group	Energy Range
1	1.35 to 14.9 MeV
2	0.408 to 1.35 MeV
3	9.12 to 408 KeV
4	0.130 to 9.12 KeV
5	2.38 to 130 eV
6	0.65 to 2.38 eV
7	0.16 to 0.65 eV
8	0.06 to 0.16 eV
9	0.005 to 0.06 eV

18-Group Set

1	4.49 to 14.9 MeV	12	0.65 to 1.29 eV
2	1.35 to 4.49 MeV	13	0.30 to 0.65 eV
3	0.743 to 1.35 MeV	14	0.16 to 0.30 eV
4	0.408 to 0.743 MeV	15	0.10 to 0.16 eV
5	0.123 to 0.408 MeV	16	0.06 to 0.10 eV
6	9.12 to 123. KeV	17	0.02 to 0.06 eV
7	0.961 to 9.12 KeV	18	0.005 to 0.02 eV
8	130. to 961. eV		
9	17.6 to 130. eV		
10	2.38 to 17.6 eV		
11	1.29 to 2.38 eV		

1.6 Computational Methods

The computer codes used for reactor criticality and flux distributions were primarily the discrete ordinants codes DTF[6] and TWOTRAN.[7] All design calculations were performed with the two-dimensional TWOTRAN. Calculations to determine eigenvalue, flux, fission distributions, and temperature effects were generally performed in R-Z geometry, while control rod worths, slotted core configurations, and azimuthally-dependent quantities were determined in R-Θ geometry. Neutron generation times were calculated with the monte carlo code KENO-II.[8] These monte carlo calculations also gave estimates of eigenvalues and flux distributions. Detailed calculations of fission density peaking in selected locations, control rod worths, and confirmatory calculations were performed with the monte carlo code MORSE.[9] Kinetics calculations were performed with two coupled kinetics-heat transfer codes. Detailed pulse shapes and feedback effects were calculated with a 1D space-time diffusion-1D heat transfer code, SAK.[10] Longer term transients were computed with a coupled point kinetics-1D heat transfer code PK1D.[10] All temperature-dependent neutron cross sections were generated with AMPX.

2. CORE DESIGN PARAMETER STUDIES

2.1 Design Constraints

Parametric studies were performed to evaluate the sensitivity of reactor performance and characteristics to core design parameters. The survey calculations performed to evaluate the single region core design utilized the same design constraints and operational goals as the earlier two-region core design studies. Core size and fuel loading ranges are summarized in Table 2.1-1. Core size was restricted by the current grid plate to 6 full rows of fuel. Fuel loadings were limited to less than 30 w/o UO_2 in BeO, which was taken to be an upper limit fuel composition for acceptable mechanical properties in the fuel material. The relatively high fissile loading in the UO_2-BeO fuel elements requires reflector elements to control fission density peaking at the outer fuel surface. These reflector elements also serve to reduce the neutron generation time. Survey calculations examined only stainless steel and graphite reflector elements.

TABLE 2.1-1

CORE SIZE AND FUEL LOADING FOR

SINGLE REGION BeO-UO_2 CORE DESIGNS

Core Size (# Elements)	w/o $^{235}UO_2$	w/o $^{238}UO_2$	w/o UO_2	Reflector*
132	13.0	6.0	19.0	SS/G
132	14.8	14.0	28.8	G
180	6.5	6.0	12.5	SS/G
180	7.6	14.0	21.6	SS/G
234	4.5	6.0	10.5	SS/G
234	5.3	14.0	19.3	SS/g

* SS -- Stainless Steel Dummy Elements

G -- Graphite Dummy Elements

2.2 Neutron Flux, Energy Spectrum and Fission Density

Homogeneous reactor calculations using cell weighted cross section sets in the 2D S_N code TWOTRAN were used to evaluate basic flux and fission distributions and fuel loading for the range of core configurations given in Table 2-1.

Relative fission density profiles for 4, 5, and 6-row core designs are shown in Figure 2.2-1. The relatively small 4 row core (132 elements) shows pronounced fission density peaking due to high fuel loading. The larger core designs show milder fission density distributions indicating lower thermal stresses in the BeO fuel. Calculations were performed with 9 group cross sections generated from ENDFB-III and IV data. The actual fuel loading required for an excess reactivity of 6% is shown for all core designs in Figure 2.2-2. The low enrichment small core designs require up to 16 w/o $^{235}UO_2$ when reflected with stainless steel elements; the larger high enrichment core designs require only 6 w/o $^{235}UO_2$ using the stainless reflector elements. (The range of fuel loadings considered for the two region core designs was 9.5 to 11.5 w/o $^{235}UO_2$.) Overall core performance (pulse fluence) increases with reduced fuel loading and larger core size and local peaking effects are also reduced. The effects of increasing ^{238}U loading and stainless steel reflecting elements requires an increased ^{235}U concentration. Both of these design options are directed toward reducing pulse widths and initial periods.

The neutron energy spectrum for a UO_2-BeO core is compared to a two region core and the current ACPR in Figure 2.2-3. The reduced fuel concentration in the single region core results in a slightly

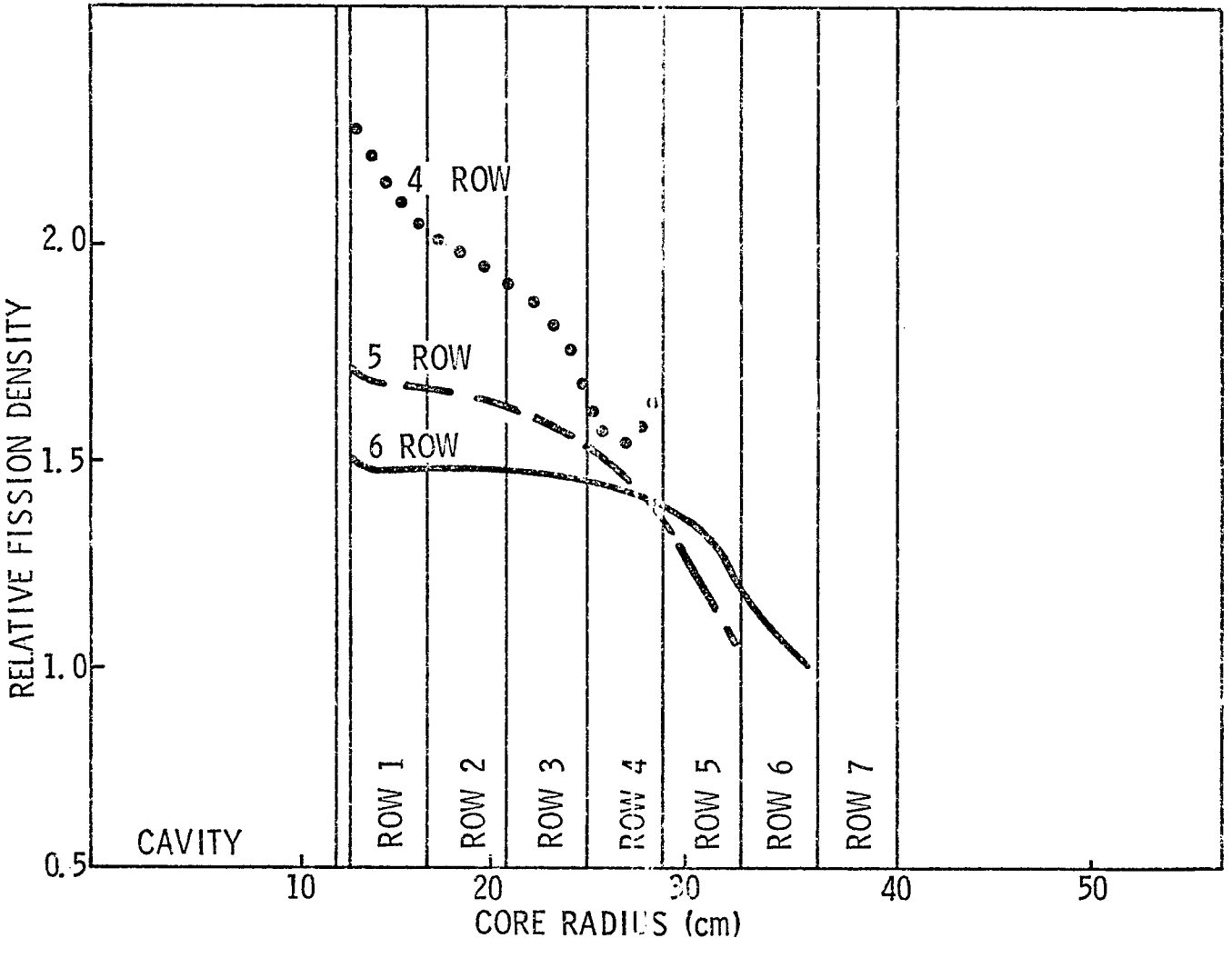

FIGURE 2.2-1. RELATIVE FISSION DENSITY FOR SINGLE REGION UO_2-BeO CORE DESIGNS. (STAINLESS STEEL REFLECTOR)

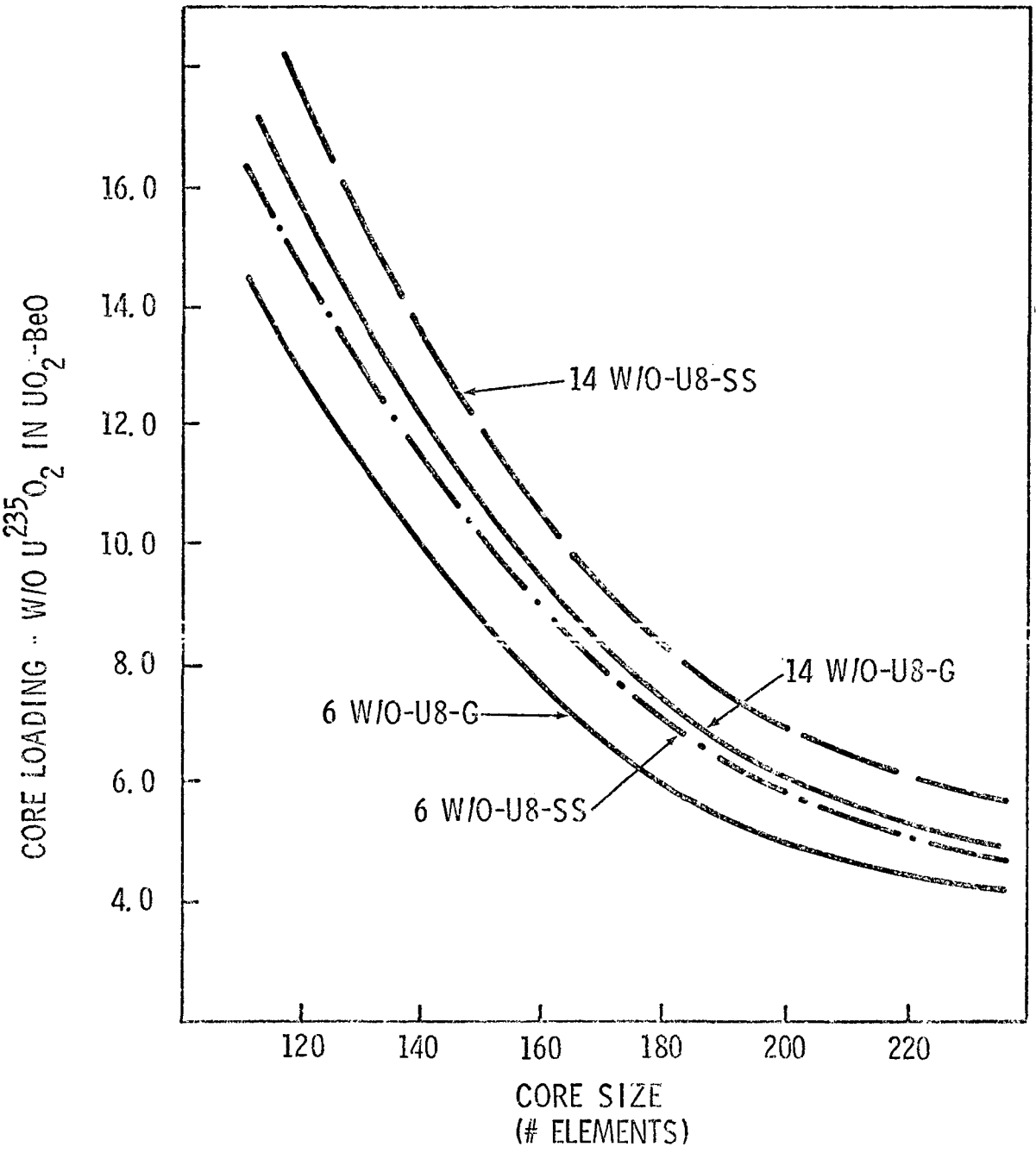

FIGURE 2.2-2. U^{235} LOADING FOR SINGLE REGION UO_2-BeO CORE.

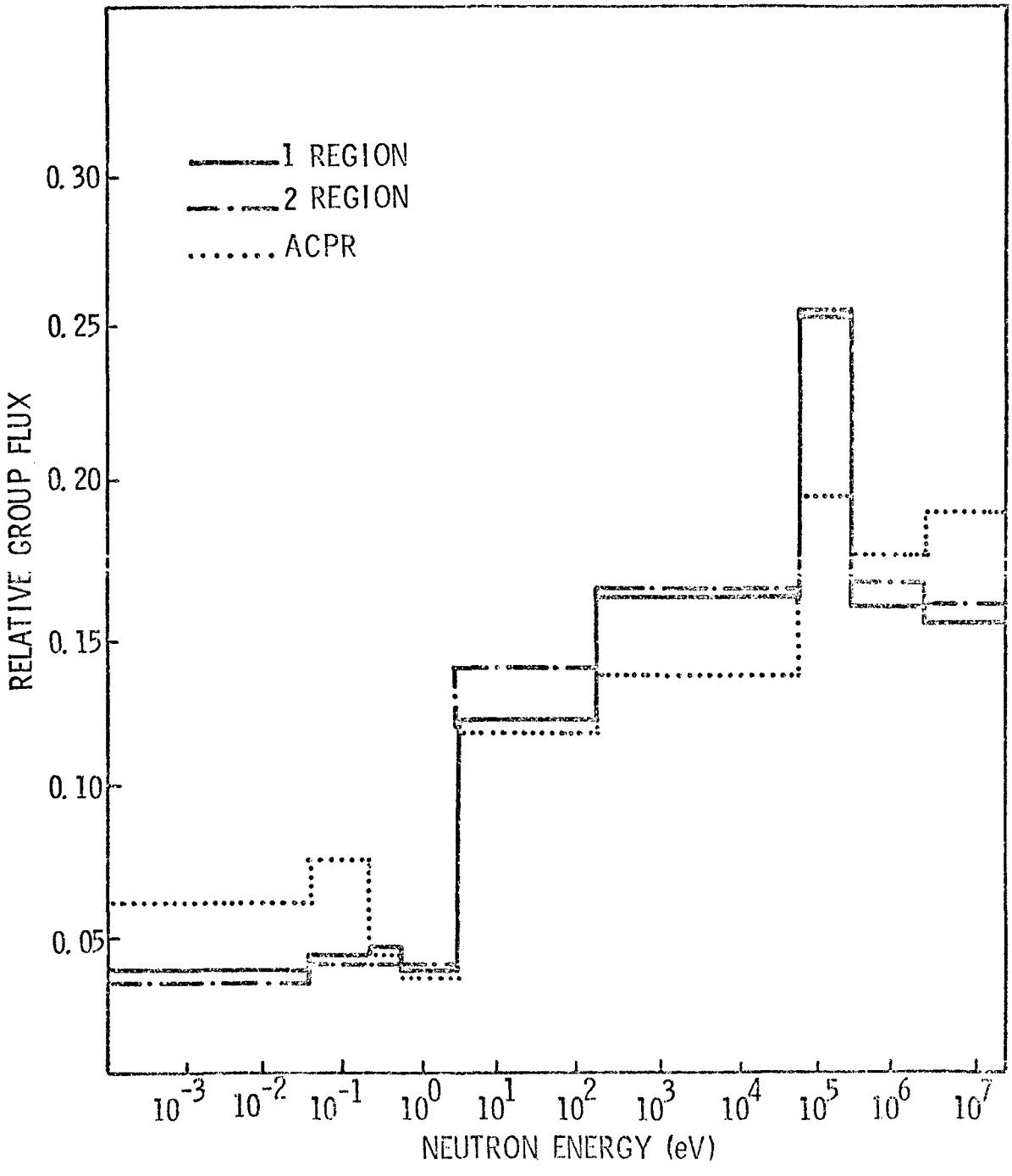

FIGURE 2.2-3. CAVITY FLUX SPECTRUM COMPARISON.

softer cavity spectrum than the two-region core. The neutron spectrum is still considerably harder than the current ACPR spectrum.

2.3 Neutron Pulse Fluence Performance

The pulse performance improvement factor for the variety of designs examined in the survey calculations is shown in Figure 2.3-1. The core designs with the more moderating reflector and highest enrichment have the lowest fuel concentrations and the highest performance potential for a given core size. It is apparent that core designs exceeding about 200 elements will be able to meet the performance goal of 2.6 at 1200°C maximum adiabatic fuel temperature.

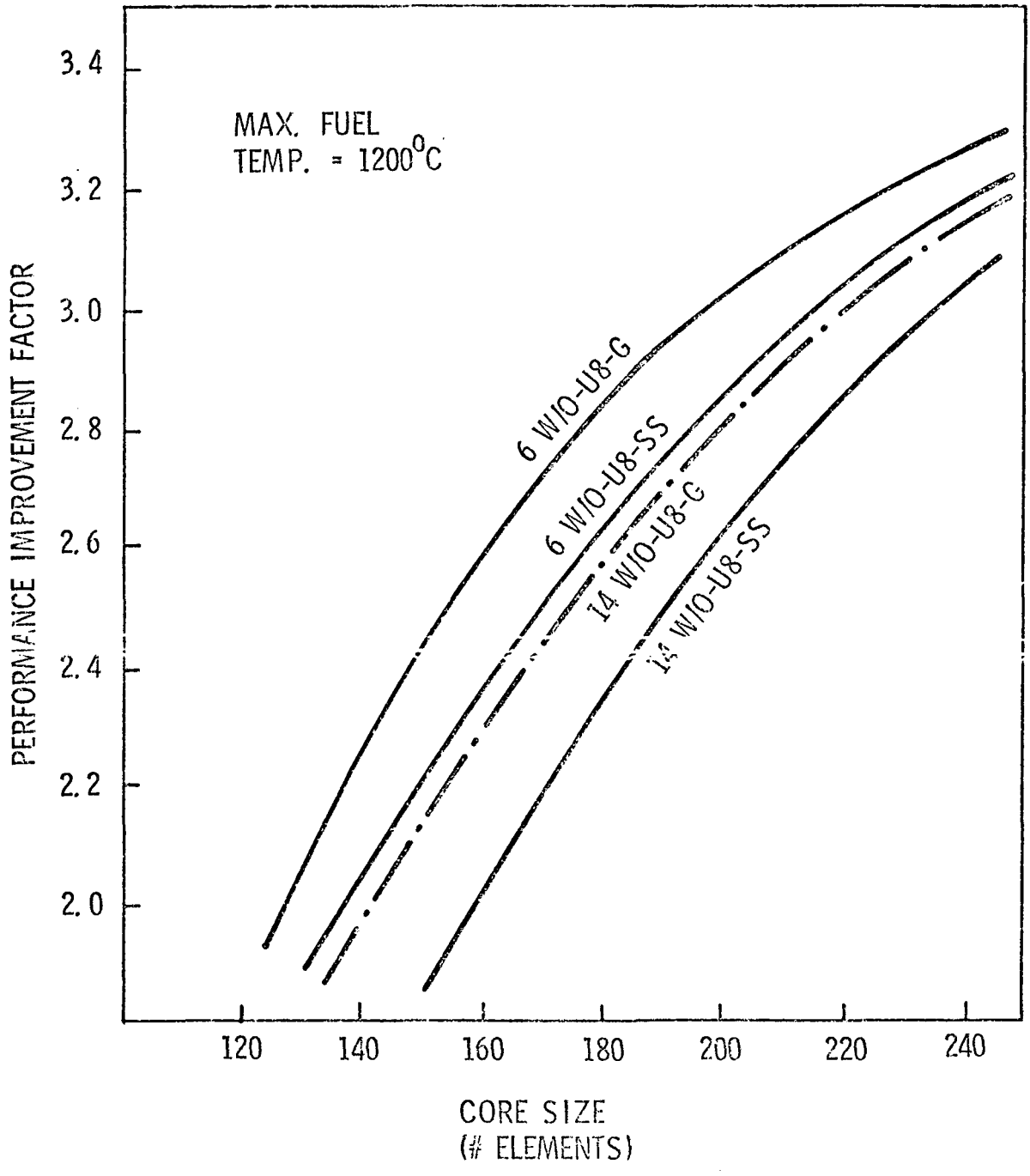

FIGURE 2.3-1. PERFORMANCE IMPROVEMENT FACTOR FOR THE SINGLE REGION UO_2-BeO CORE FOR A MAXIMUM ADIABATIC FUEL TEMPERATURE OF 1200°C.

2.4 Reactor Kinetics Parameters

Analysis of reactor kinetics was performed using two dimensional S_N calculations to determine reactivity loss with temperature, and monte carlo techniques to evaluate the neutron generation time. These results were used in a point kinetics model to estimate minimum initial periods and pulse widths. The results of the S_N calculations for the fuel temperatures coefficient of reactivity shown in Figure 2.4-1 are average values over the temperature range of 27°C to 627°C which is the approximate average core temperature range for the UO_2-BeO fuel. The magnitude of the fuel temperature coefficient for the single region cores is in the range of -0.3 to -0.6 ¢/°C. The temperature coefficient for the current ACPR is -1.35 ¢/°C. The longer initial periods and greater pulse widths indicated by the reduced temperature coefficient can be mitigated to some degree by a reduction in the neutron generation time, ℓ. The hydride based fuels are characterized by a significantly greater negative temperature coefficient, but the very low fissile concentration and soft neutron spectrum also resulted in a long neutron generation time for core designs with hydride fueled regions. Values for ℓ calculated for the two region cores were in the range of 36-43 μsec. The neutron generation times for all core designs were calculated using the monte carlo code KENO-II. The results are shown in Figure 2.4-2 for the variety of core designs examined in the survey calculations. The higher ^{238}U concentrations and less moderating reflector materials result in reduced generation times. The magnitude of this reduction as a function of design parameters

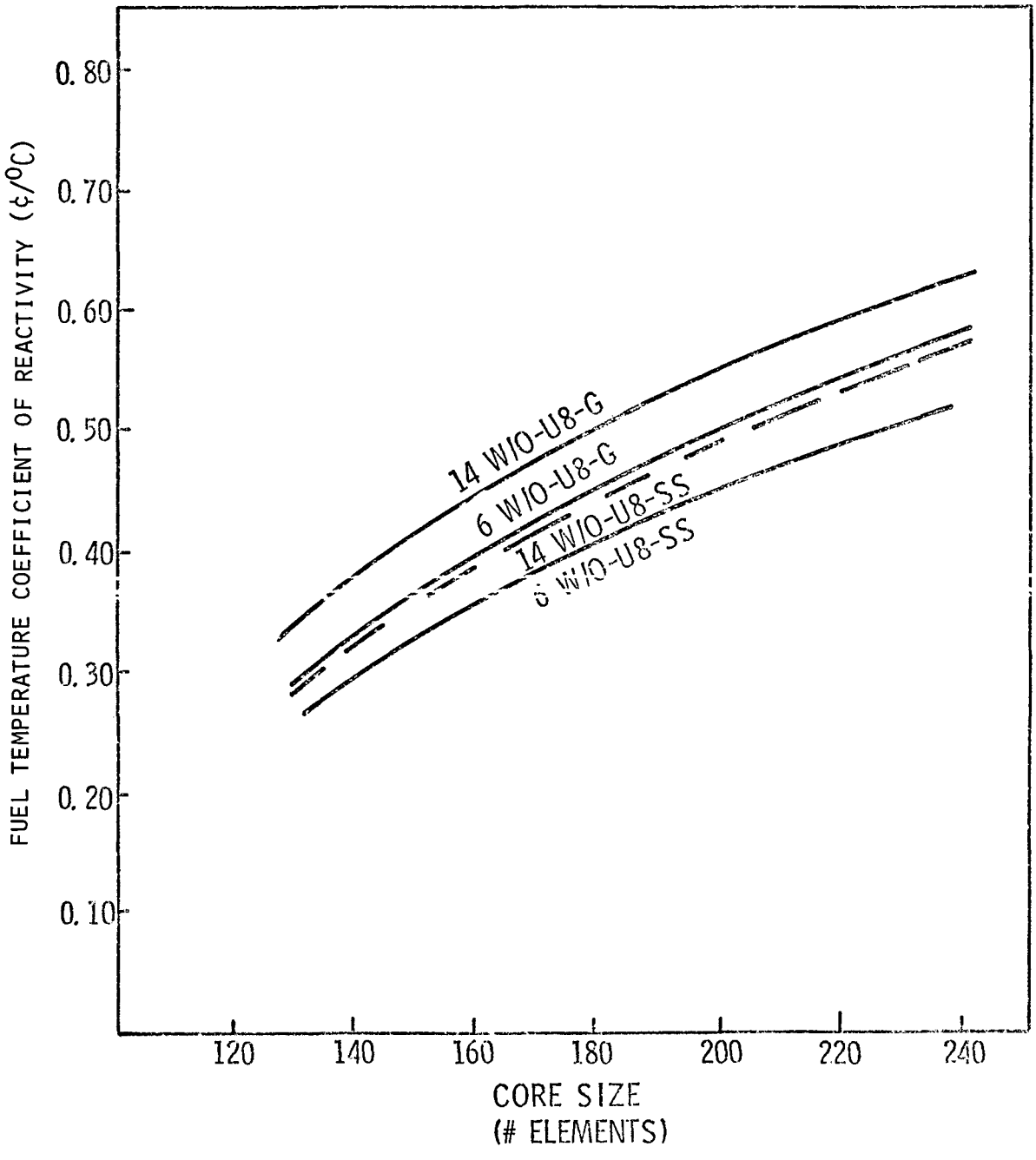

FIGURE 2.4-1. FUEL TEMPERATURE COEFFICIENT OF REACTIVITY FOR SINGLE REGION UO_2-BeO CORE.

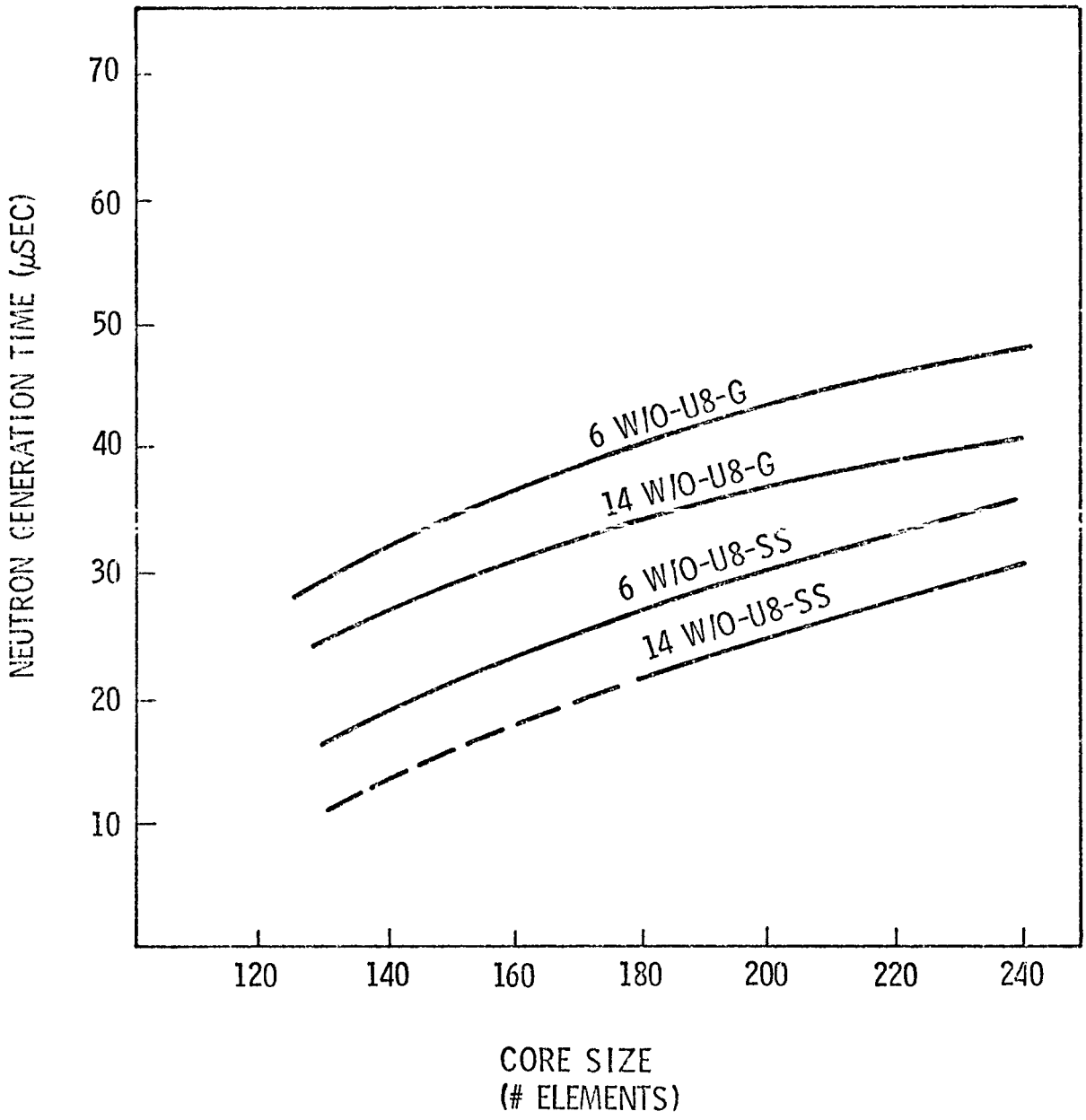

FIGURE 2.4-2. NEUTRON GENERATION TIMES FOR SINGLE REGION UO_2-BeO CORES. (MONTE CARLO AT 27°C)

is most significant for the smaller cores where the reflector influence is strongest.

The combined effect of reflector, ^{238}U content, core size, and fissile concentration on the minimum initial period are shown in Figure 2.4-3. The stainless steel reflected designs show the expected trend of initial period increasing with core size. For this approach, increasing core size causes a larger increase in neutron generation time than the accompanying increase in temperature feedback due to the reduction in fissile content.

The opposite trend is observed for the graphite reflected core designs. The decrease in initial period with increasing core size is due to the influence of the soft reflector. The neutron generation time is dominated by soft reflector neutrons so that the increase in generation time is less significant than the increase in the temperature feedback due to more dilute fissile concentrations for the larger cores. The initial period, however, remains greater for the graphite reflectors. Figure 2.4-3 illustrates the diminishing effect of the reflector on reactor kinetics as the core size increases.

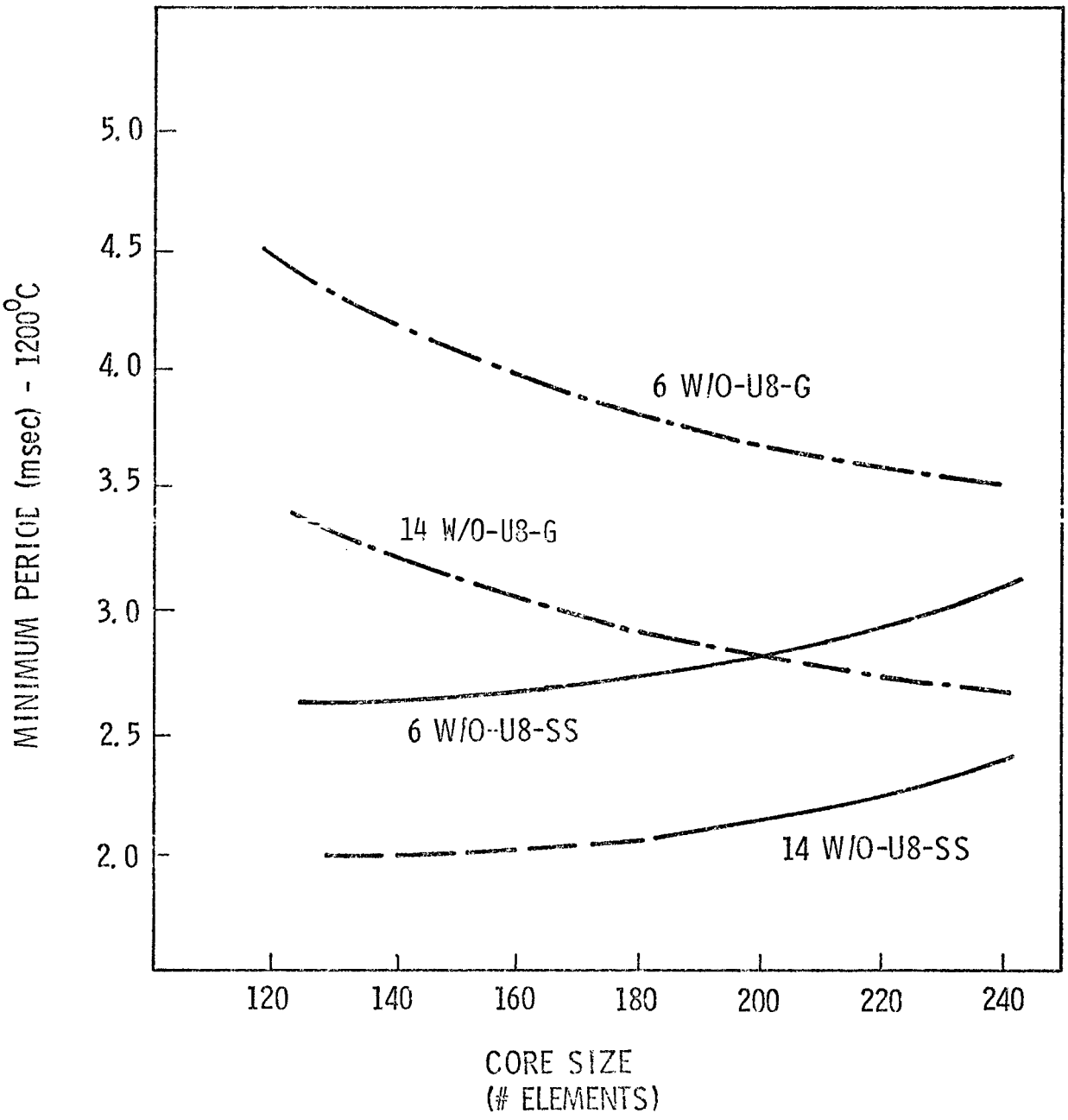

FIGURE 2.4-3. INITIAL PERIOD FOR SINGLE REGION UO_2-BeO CORES FOR 1200°C MAXIMUM ADIABATIC FUEL TEMPERATURE.

2.5 Reactor Performance and Kinetics Summary

The combined effects of design parameters on kinetics and performance is shown in Figure 2.5-1. The solid lines represent an approximation for a continuous change in reflector properties from stainless steel to graphite. It is apparent that the performance goal of 2.6 requires a core size of about 5 rows for the slower core designs, and about 5 1/2 rows for the faster core designs. For a maximum adiabatic fuel temperature of 1200°C, the minimum initial period is only slightly longer than that attainable with a two-region core design. All survey core designs had 6% excess reactivity and had a fuel height of 50.8 cm.

The same performance-period data is shown in Figure 2.5-2 for a maximum adiabatic fuel temperature of 1400°C. The results of the UO_2-BeO fuels testing program indicate that the maximum permissible peak adiabatic temperature in the fuel under test conditions is in the range of 1200-1400°C. The maximum permissible fuel temperature under operating conditions in the reactor is expected to be increased somewhat due to reduced stress levels in the fuel pellets. The ratio of calculated maximum principal stresses for the fuel pellet tests and the anticipated reactor conditions are shown as of function of core size (fissile concentration) in Figure 2.5-3. These approximate calculated stresses are based on adiabatic fission density profiles measured in fuel pellet tests and monte carlo calculations for reactor operating conditions.

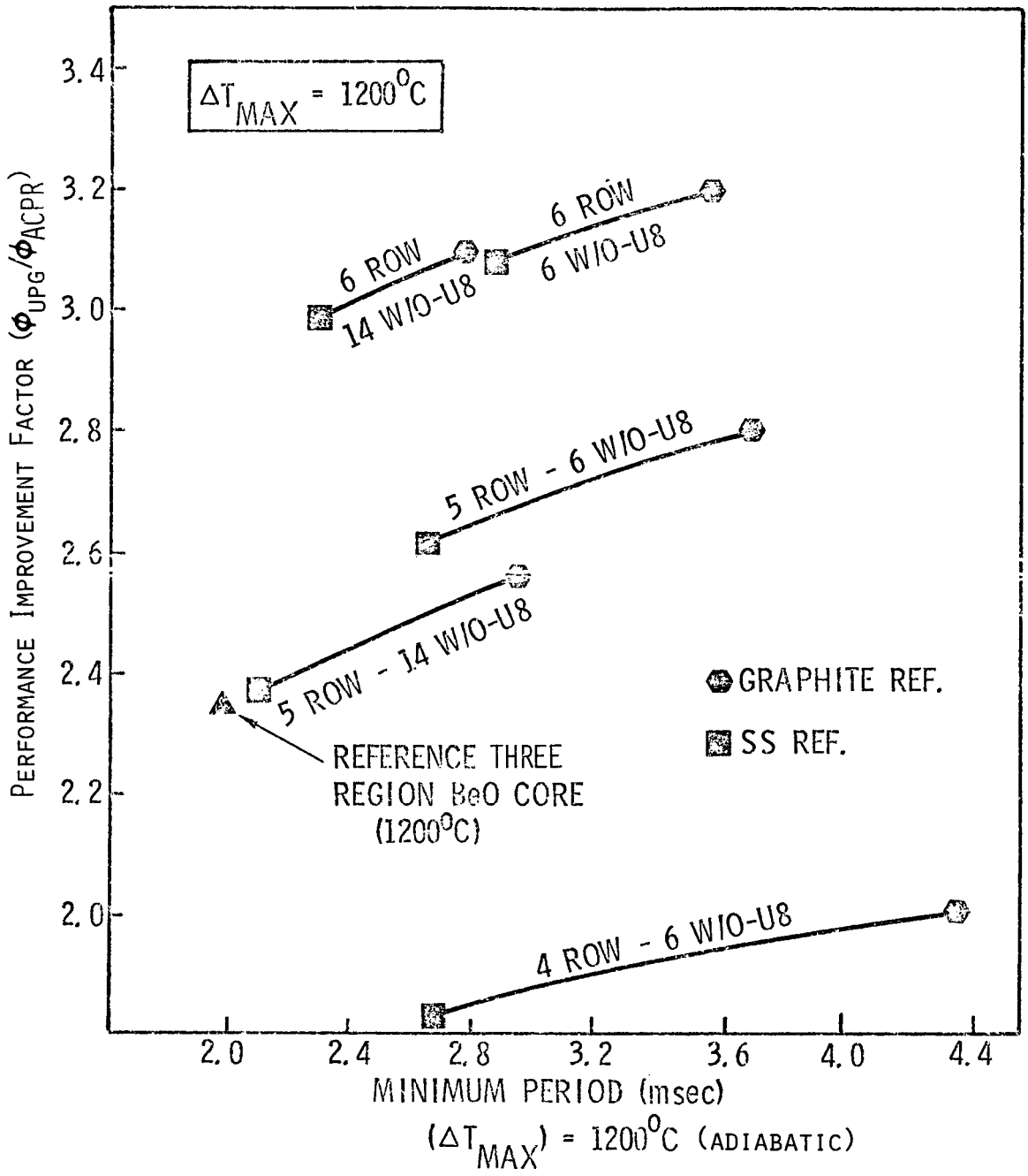

FIGURE 2.5-1. PERFORMANCE IMPROVEMENT AND INITIAL PERIOD FOR SINGLE REGION UO_2-BeO CORES.

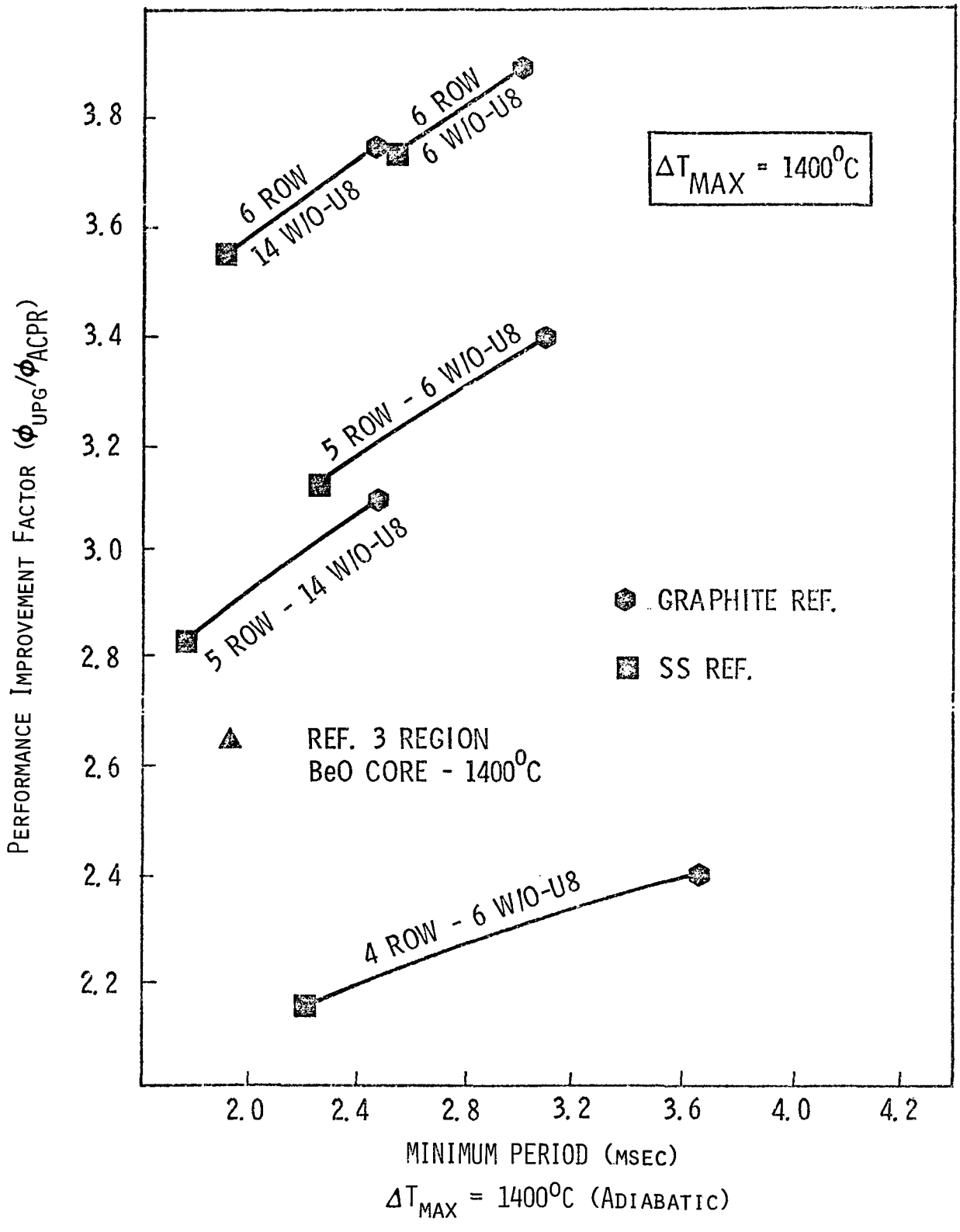

FIGURE 2.5-2. PERFORMANCE IMPROVEMENT AND INITIAL PERIOD FOR SINGLE REGION CORE (1400°C).

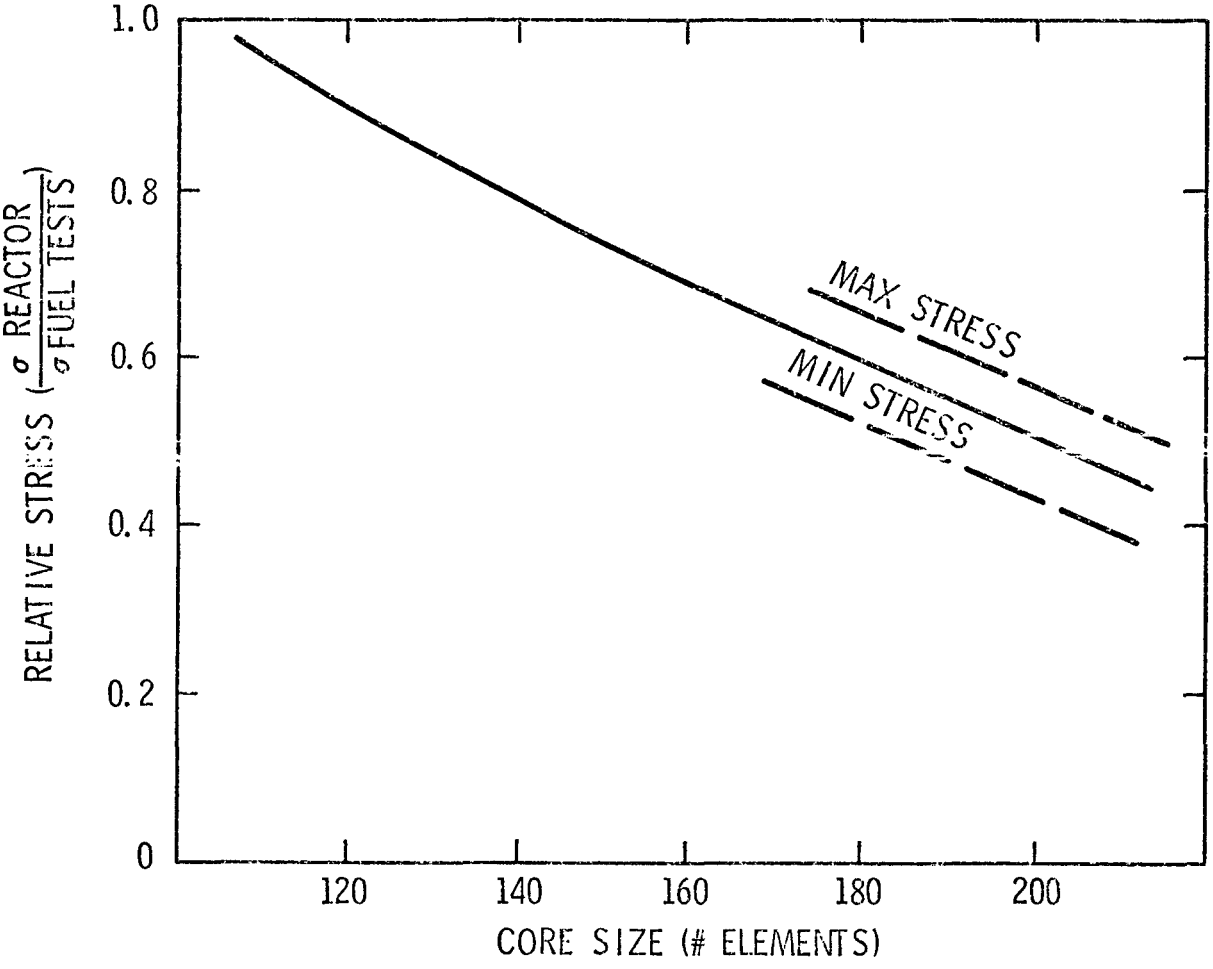

FIGURE 2.5-3. RATIO OF APPROXIMATE THERMALLY INDUCED STRESSES FOR OPERATING CONDITIONS TO FUEL PELLET TEST CONDITIONS.

Based on these survey calculations, final core design calculations focused on a nominal 200 element core using nickel reflecting elements and 21.5 w/o UO_2 in a BeO matrix. Enrichment for the final core design is 35% to achieve sufficient Doppler feedback to provide a relatively narrow pulse. Chapter 3 summarizes these design calculations.

3. ACPR UPGRADE CORE DESIGN

3.1 Core Geometry and Dimensions

The ACPR Upgrade core geometry is identical to the original ACPR grid plate arrangement. This configuration effectively limits the number of fuel elements that could be considered to less than 234 element positions (6 rows). The grid plate vertical spacing limits the effective fuel height to about 52 cm. The fuel element diameter and pitch are 3.747 cm and 4.171 cm, respectively. Based on these design constraints, a two-dimensional R-Z model of the Upgrade was developed for the final core design studies as shown in Figure 3.1-1. Material identification and volume fractions for each material are given in Appendix 1. A summary of important reactor design specifications is given in Table 3.1-1.

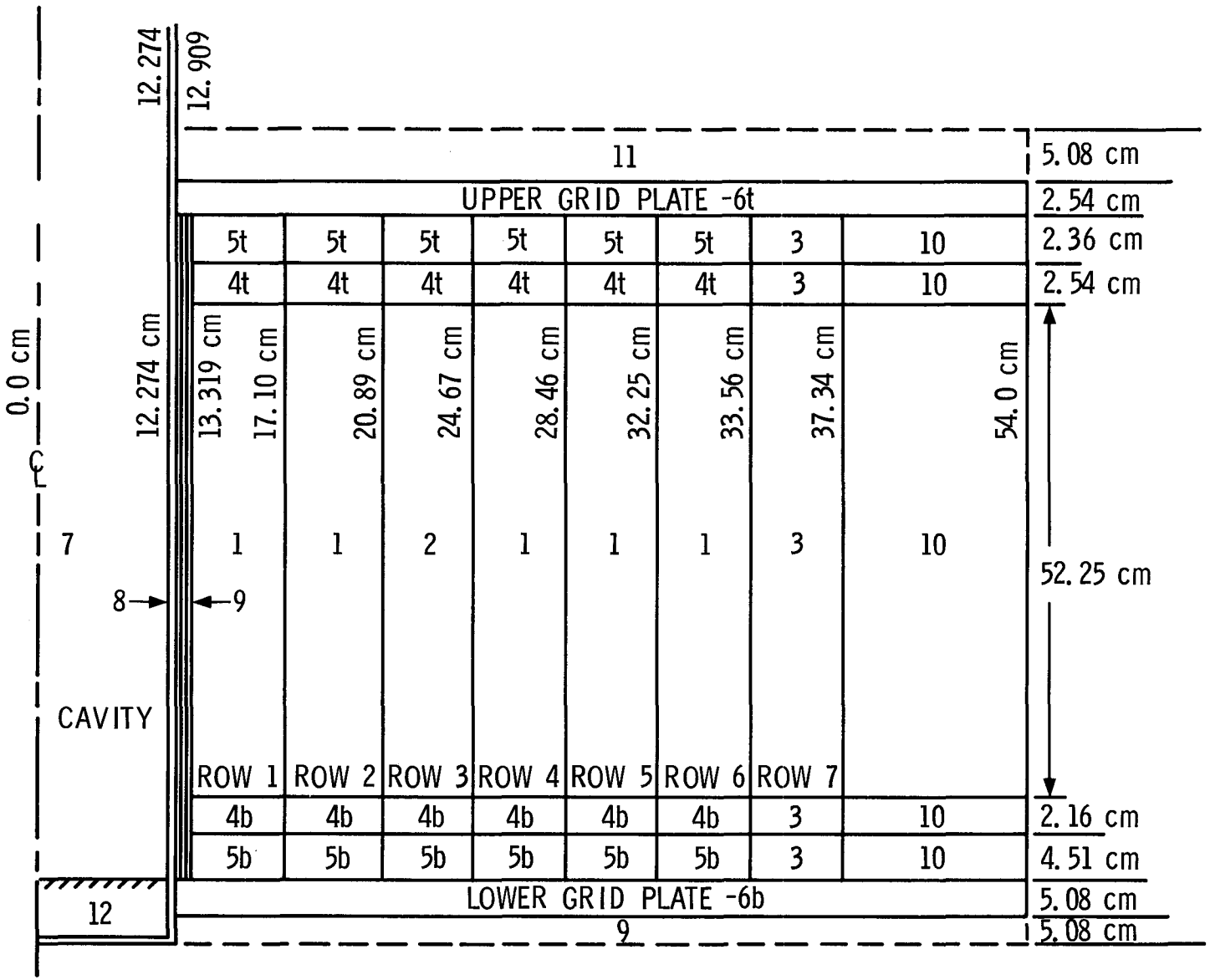

FIGURE 3.1-1. HOMOGENIZED R-Z MODEL OF ACPR UPGRADE GEOMETRY.
(MATERIAL ASSIGNMENTS - APPENDIX A).

TABLE 3.1-1

ACPR UPGRADE DESIGN SPECIFICATIONS

Fuel	UO_2 - BeO 21.5 w/o UO_2 in BeO 35% Enrichment
Cell Volume - Fractions	fuel - 0.554 clad - 0.0392 liner - 0.0320 coolant - 0.268
Core Geometry	
Cell Area	15.06 cm^2
Lattice	Hexagonal
Pitch	4.171 cm
# Elements	200
Fuel Element Diameter	3.747 cm
Homogenized Radii Inner/Outer	13.319/33.56 cm
Fuel Height	52.25 cm
Control Rods	
Regulating	6
Pulse	3
Safety	2

3.2 Eigenvalue Calculations

Eigenvalue calculations were performed for the ACPR Upgrade using several different calculational models and cross section sets. Most calculations were performed with the discrete ordinates code TWOTRAN using R-Z geometry. Confirmatory calculations were performed with monte carlo codes using both an R-Z geometry and the correct hexagonal lattice. The results of these eigenvalue calculations are summarized in Table 3.2-1. The spread in the results of the various models (excluding the MORSE model) is about 1.2%. The MORSE model was primarily used for fission density peaking effects and was not included in final eigenvalue estimates. The maximum desired reactivity excess for the Upgrade is \$8.00, which is equivalent to k = 1.062. For the majority of applications, the predicted core eigenvalue was taken as the lower value in Table 3.2-1 of k = 1.054, which results in \$7.0 excess reactivity in a cold clean configuration.

The sensitivity of the eigenvalue calculations to cross section weighting and fuel loading uncertainties was also examined. The results of these calculations are plotted in Figure 3.2-1. Cross section weighting errors of 10% result in eigenvalue changes of only 0.3%. Fuel loading uncertainties of 10% result in eigenvalue changes of about 1.0%. Since fuel composition is known to within $\leq$0.5%, the potential error introduced from these sources is not significant.

Uncertainties in the predicted eigenvalue from other sources were considered to be potentially significant. Cross section values, particularly resonance and scattering kernal calculations,

TABLE 3.2-1

EIGENVALUE CALCULATIONS FOR REFERENCE ACPR UPGRADE

CORE CONFIGURATIONS*

	Calculation	Code	Energy Groups	Eigenvalue
1.	2D, (R-Z), P_1, S_4	TWOTRAN	9	1.067
2.	2D, (R-Z), P_1, S_8	TWOTRAN	9	1.059
3.	2D, (R-Z), P_1, S_4	TWOTRAN	18	1.059
4.	2D, (R-Z), Monte Carlo (R-Z)	KENO-II	9	1.054 ± 0.006
5.	3D, Monte Carlo** Hexagonal	MORSE	9	1.085 ± 0.01
6.	3D, Monte Carlo (X-Y-Z)	KENO-II	9	1.057

*300°K
3 Tansient Rod Voids
8 Fuel Followers
187 Fuel Elements
Empty Cavity
Ni Reflector Elements

**Fission Density Peaking Model

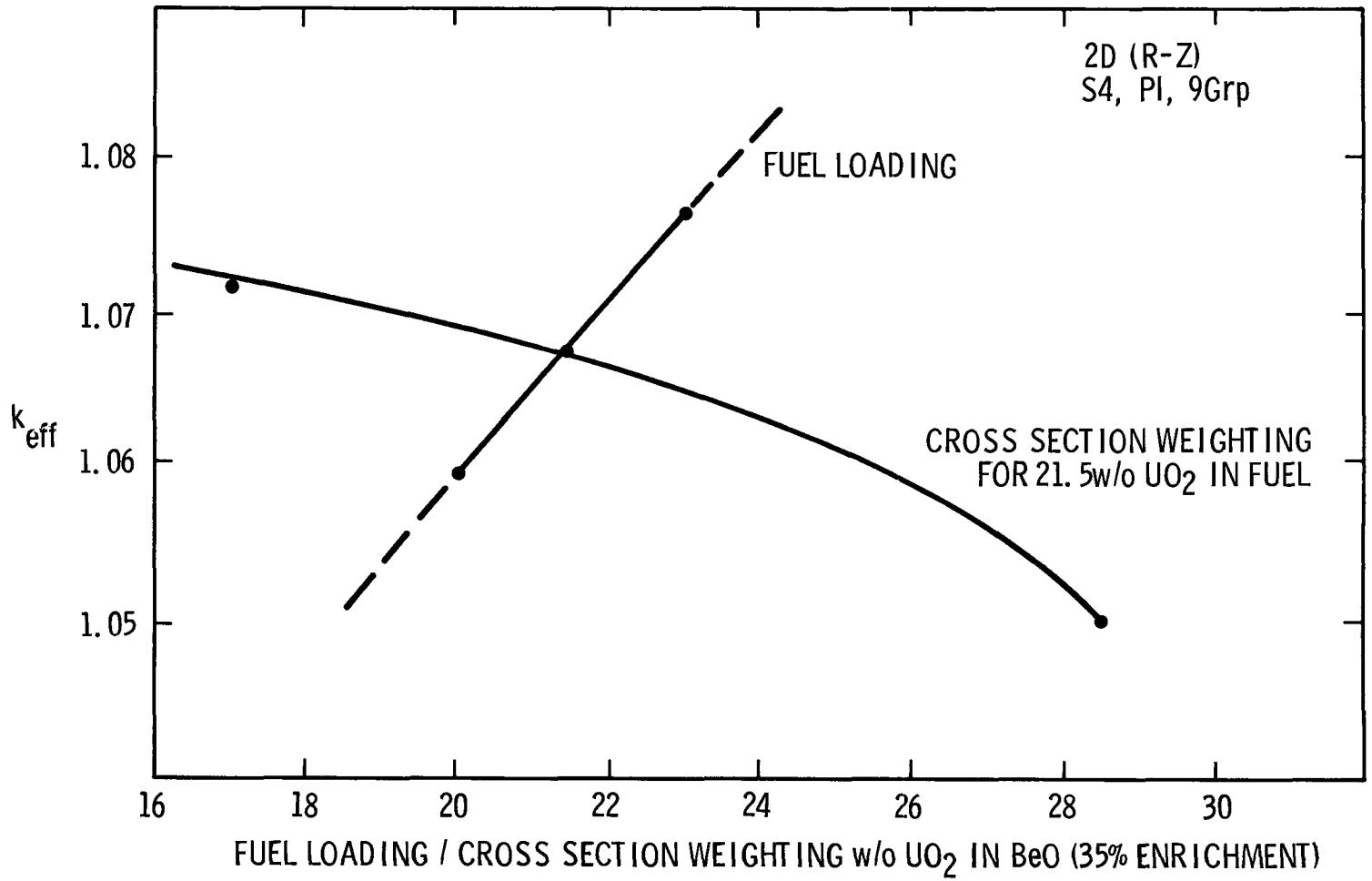

FIGURE 3.2-1. SENSITIVITY OF ACPR UPGRADE EIGENVALUE TO FUEL LOADING AND CROSS SECTION WEIGHTING.

modeling simplifications and uncertainties in dimensions and composition require consideration. Although the magnitude of these effects is difficult to assess predictively, calculations performed on the ACPR (Appendix 3) showed a 2% discrepancy between best estimate calculations and the measured multiplication constant. It was felt that this discrepancy should be accounted for in the upgrade estimates of excess reactivity even though different fuel materials are involved. Therefore, although actual eigenvalue calculations are given in this text, an approximate 2% multiplication difference was allowed for in estimates of fuel requirements and critical size.

The effective multiplication constant for the UO_2-BeO core as a function of the number of fuel elements is shown in Figure 3.2-2. The multiplication of the water-reflected core is shown for comparison. The Ni reflecting elements decrease reactivity about \$5.00 for a 140 element core and about \$2.50 for a 200 element core. The estimate of the number of elements required for critical using the lower eigenvalue estimates from S_N calculations is approximately 148. If a correction factor for the multiplication constant is utilized from ACPR calculations (2%), the estimate of water-reflected critical size is approximately 155 elements.

Figure 3.2-3 shows the average worth of a fuel element on the outer edge of the core for both water and nickel reflected configurations. The outer fuel elements are more valuable in the Ni-reflected configuration due to greater leakage effects with the Ni reflector elements. Fuel cell cross sections used in the outer rows were the same as those used in the interior core regions

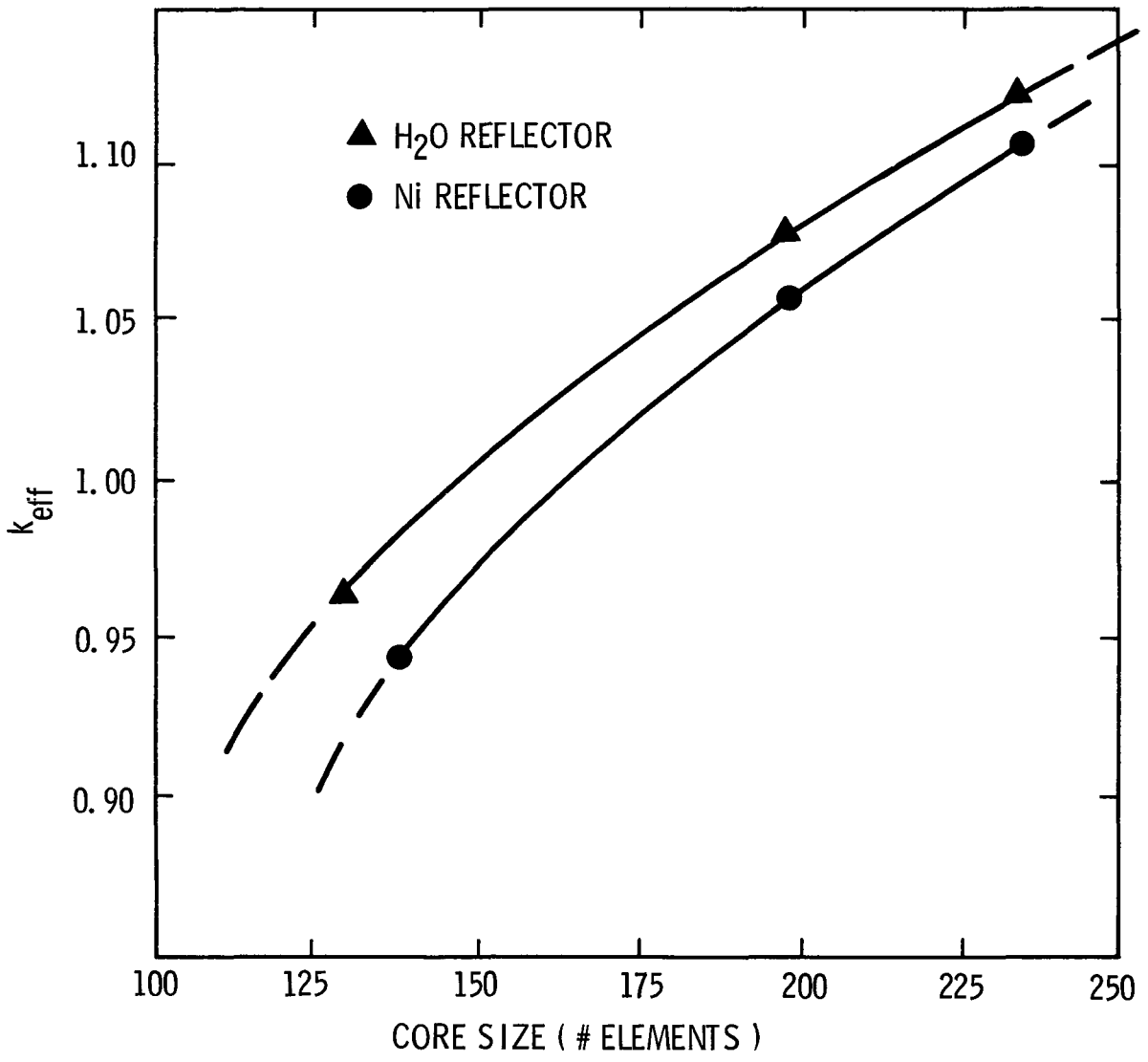

FIGURE 3.2-2 CORE MULTIPLICATION FOR NICKEL AND WATER REFLECTED CONFIGURATIONS USING TWØTRAN (S_8). (CORE SIZE INCLUDES FUEL AND VOID FOLLOWERS OF CONTROL ELEMENTS.)

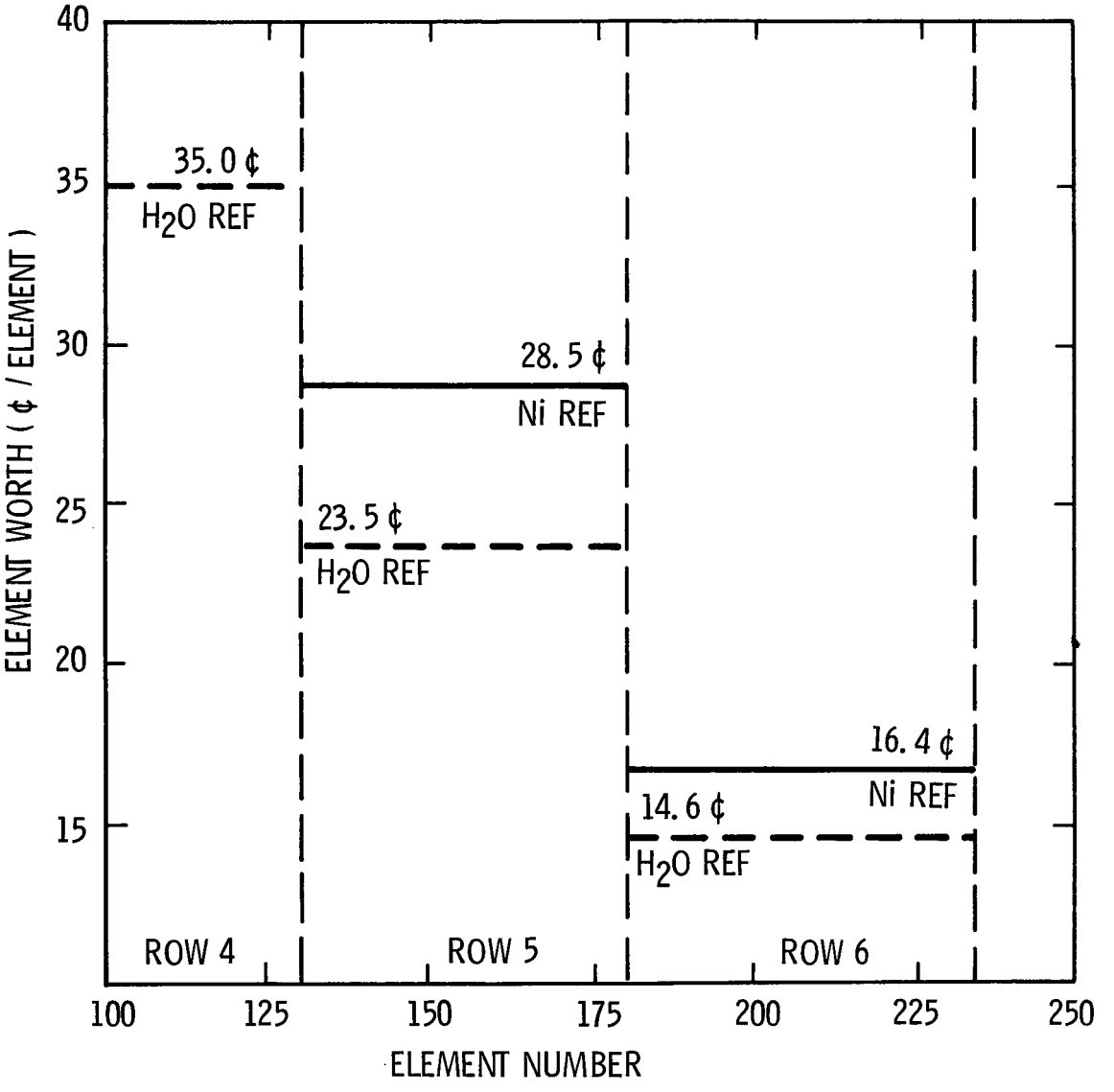

FIGURE 3.2-3. WORTH OF OUTER FUEL ELEMENTS ADDED TO WATER AND NICKEL REFLECTED CORE CONFIGURATIONS.

which were weighted with a slightly harder spectrum cell than appropriate for the fuel cells adjacent the water reflector region. The opposite is true for fuel cells adjacent the Ni reflector region. Preliminary analysis of this approximation indicated that the values shown in Figure 3.2-3 would not be altered significantly by using corrected cross section sets for the outer fuel cells.

3.3 Fission Density and Flux Distributions

Fission density distributions were calculated with homogeneous S_N calculations in R-Z geometry and with both heterogeneous discrete and homogeneous monte carlo calculations using a hexagonal lattice. The results obtained from these calculations are summarized in Figure 3.3-1. All calculations show the highest average fission density by a slight amount to be in row 1, with a generally comparable overall spatial dependence. The location of the actual peak fission density within a cell is in row 2. These effects are treated in Section 3.4.

Neutron flux distributions were determined with homogeneous, R-Z, S_N calculations. Figure 3.3.2 shows the radial distribution of the total flux along with the thermal (0.005-0.06 eV) and fast (1.35-14.9 MeV) group fluxes. The fluxes plotted in Figure 3.3-2 are at the axial midplane of the core. The axially-dependent flux at the center of the cavity is plotted in Figure 3.3-3. The fluxes shown in this figure are for an empty cavity with no axial cavity reflectors.

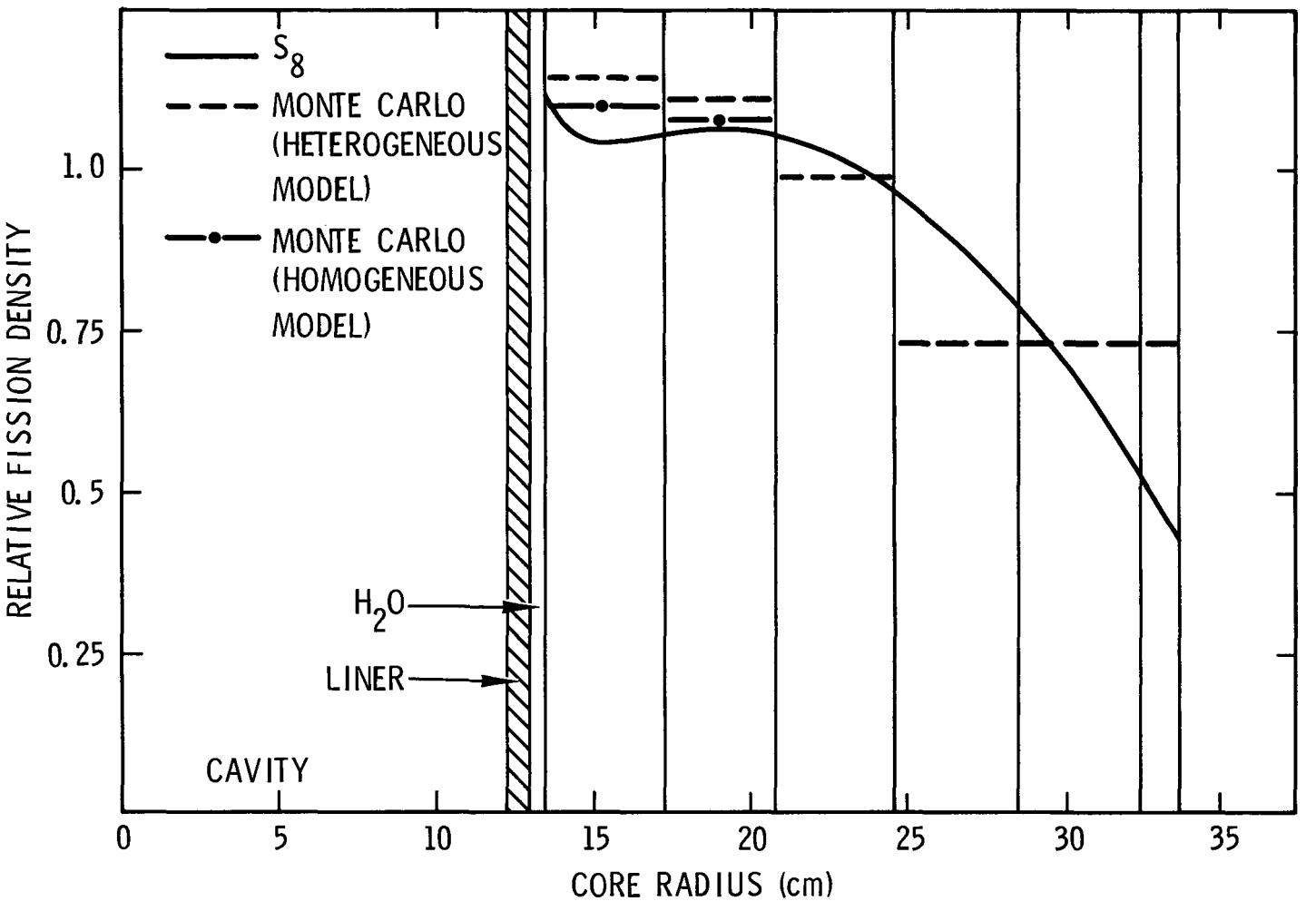

FIGURE 3.3-1. FISSION DENSITY DISTRIBUTION FOR ACPR UPGRADE (AXIAL MIDPLANE, TWOTRAN, S_8, P_1, 9 Grp and MORSE 9 Grp).

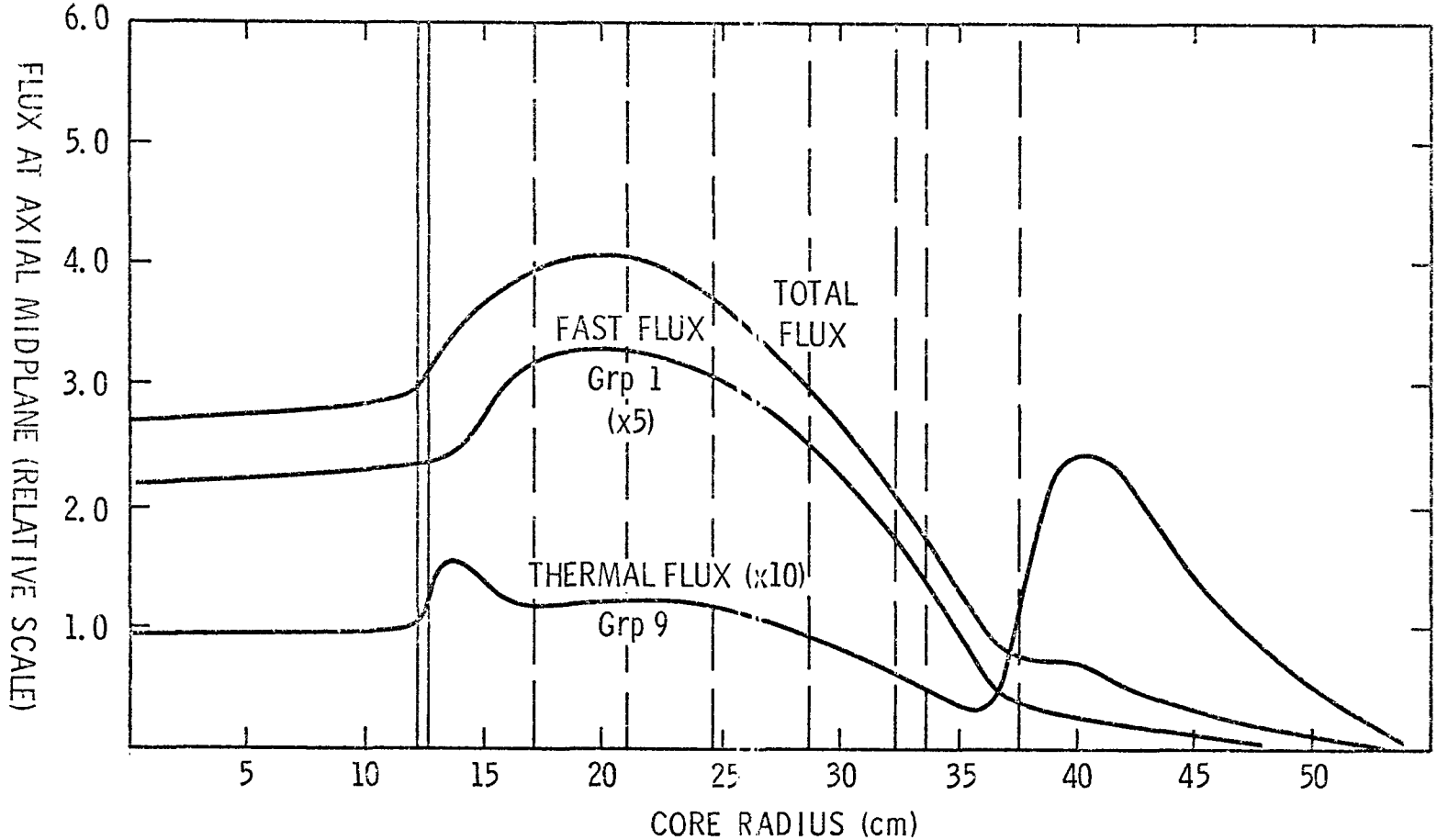

FIGURE 3.3-2. FLUX AT AXIAL MIDPLANE IN ACPR UPGRADE. (TWØTRAN, S_8, P_1 9 Grp, Grp 1 14.9→1.35 MeV, Grp 9; 0.005→0.06 eV.)

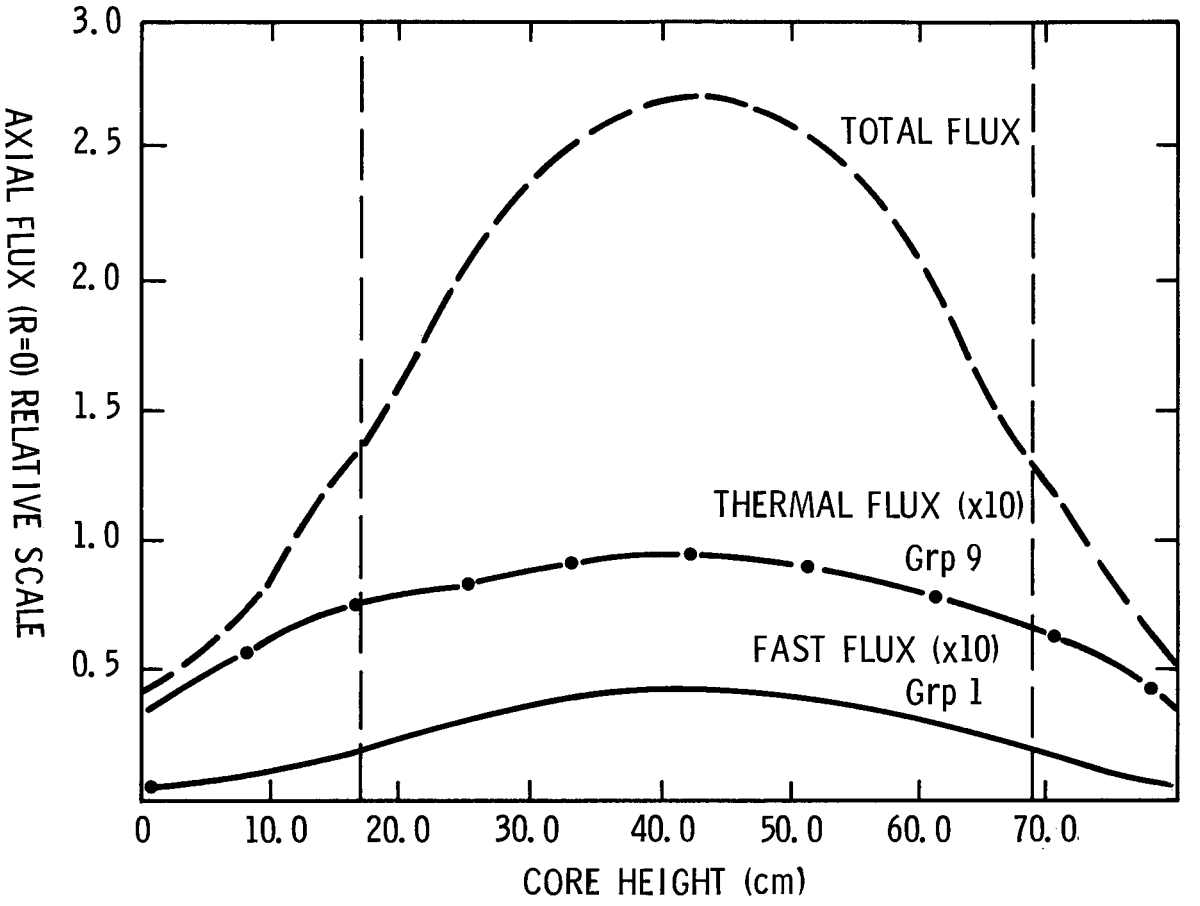

FIGURE 3.3-3. AXIAL FLUX IN CAVITY OF ACPR UPGRADE
(TWØTRAN, S_8, P_1, 9 Grp)

3.4 Fission Density Peaking Calculations

The homogenized S_N and monte carlo calculations used to estimate flux and fission densities and eigenvalues do not account for the local fission density peaking effects present in a specific cell. To assign a maximum adiabatic temperature to a given performance level, cell peaking factors were computed at relevant positions in the core. The majority of these calculations were based on the correct hexagonal lattice array modeled in three dimensions using monte carlo analysis.

Estimates of cell peaking effects were also obtained with 1D S_N cell calculations in the 123 fine group structure. The one-dimensional S_N cell calculations were performed as part of the cross section generation calculations. The XSDRNPM module in AMPX was used with a 123 group cross section library generated from ENDFB data. An S_4, P_1, 123 group cell calculation was performed for each temperature and composition under consideration. The results of this calculation for the 21.5%, 35% enriched UO_2-BeO fuel cell are given for 300°K and 1200°K in Figure 3.4-1. The peak/ave fission density at 300°K is 1.24. The 1D-S_N cell calculation was performed with zero current boundary conditions simulating an infinite array of neighboring fuel cells. The cell fission density distributions as a function of fuel loading are shown in Figure 3.4-2.

The cell fission density distributions determined from S_N analysis represent an average cell in a large array of fuel cells. The position of the cell in the core, as well as the treatment of the hexagonal geometry of the cell, require a more flexible

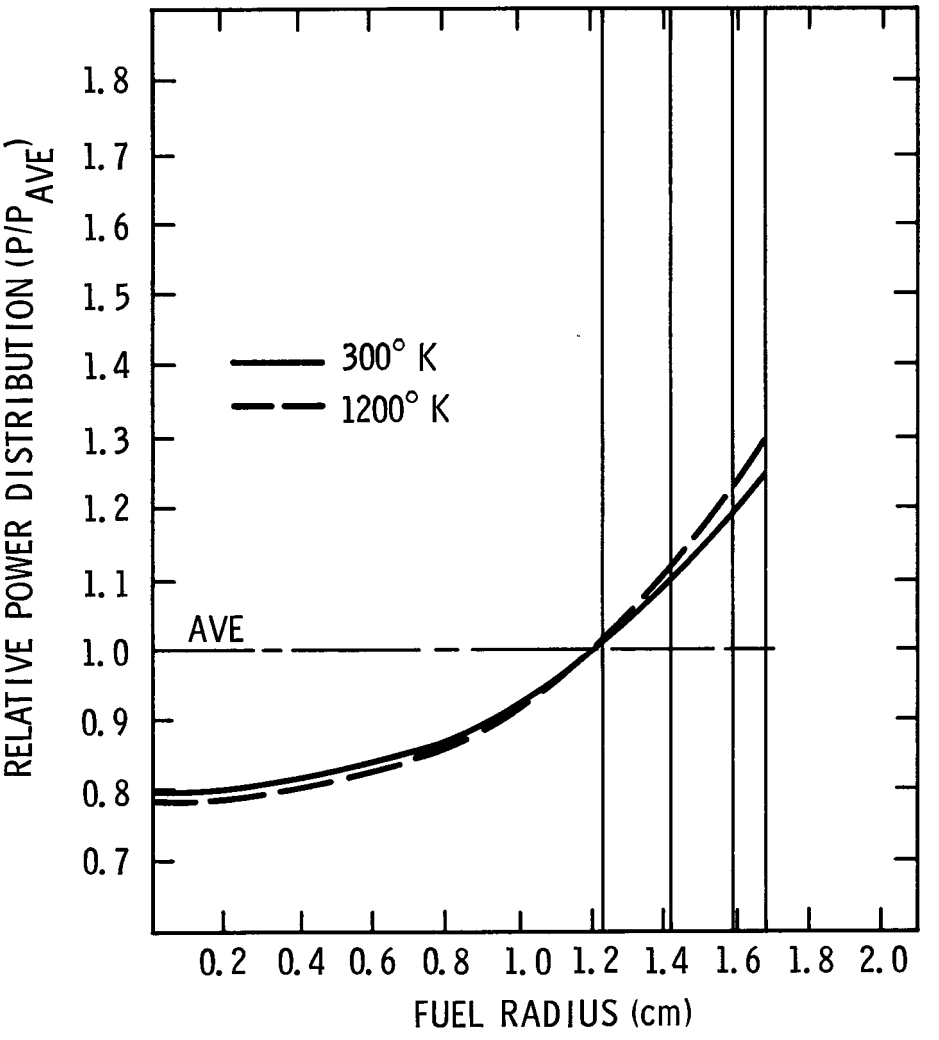

FIGURE 3.4-1. FISSION DENSITY DISTRIBUTIONS IN 21.5 W/o, 35% ENRICHED UO_2 - BeO FUEL CELL AT 300° AND 1200° K.

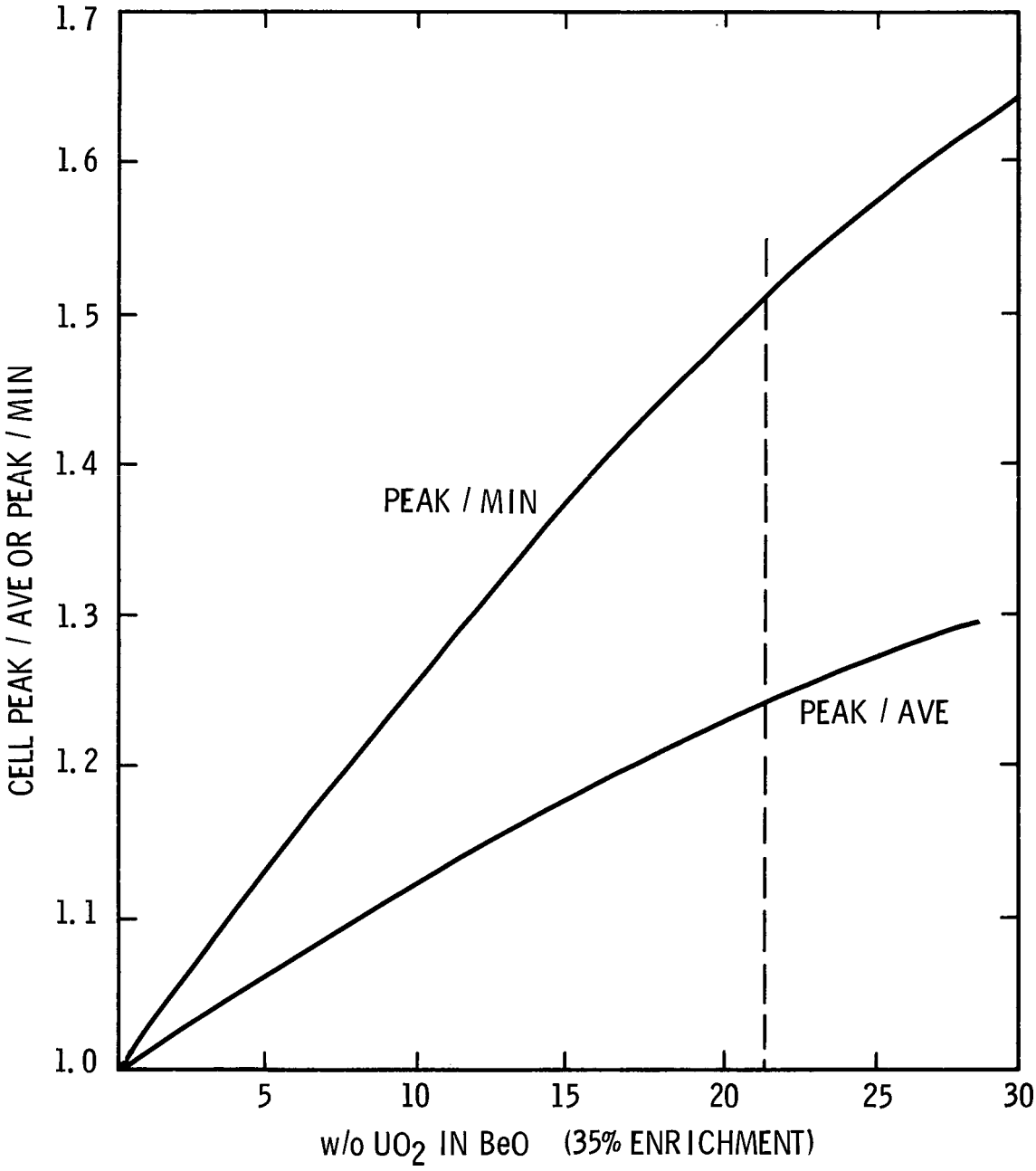

FIGURE 3.4-2. CELL CALCULATIONS FOR 35% ENRICHED UO_2 - BeO (1D-S_4-P_1) 300°K.

geometric model. A three-dimensional monte carlo model was constructed to determine cell profiles as a function of core positions using the hexagonal lattice. A schematic of this model is shown in Figure 3.4-3. The monte carlo analysis was used for a variety of core configurations to establish the location of the more severe fission density profiles. As shown in Figure 3.4-3, the profiles examined include a row 1 element on the hexagonal flat, a row 2 element adjacent the regulating rod, and a row 3 element adjacent the transient rod void. Profiles were calculated for combinations of regulating, transient and safety rods in and out.

For the purpose of determining cell fission density profiles, the core was modeled as one-twelfth of the full core. This model does not fully account for the presence of both the fuel follower of the safety rod and the transient rod void. The simultaneous treatment of both cells was not considered necessary when analyzing the localized fission density peaking effects of specific cells.

The calculations performed to determine the average fission density in a fuel cell in comparison with the core average fission density were performed with a one-sixth core model which does correctly account for the localized interactive effects of the transient and safety rods. This model is shown schematically in Figure 3.4-4, along with the fuel cell numbering scheme used to identify the location of each fuel cell.

The results of the calculations using the model of Figure 3.4-4 for average fission density ratios are summarized in Table

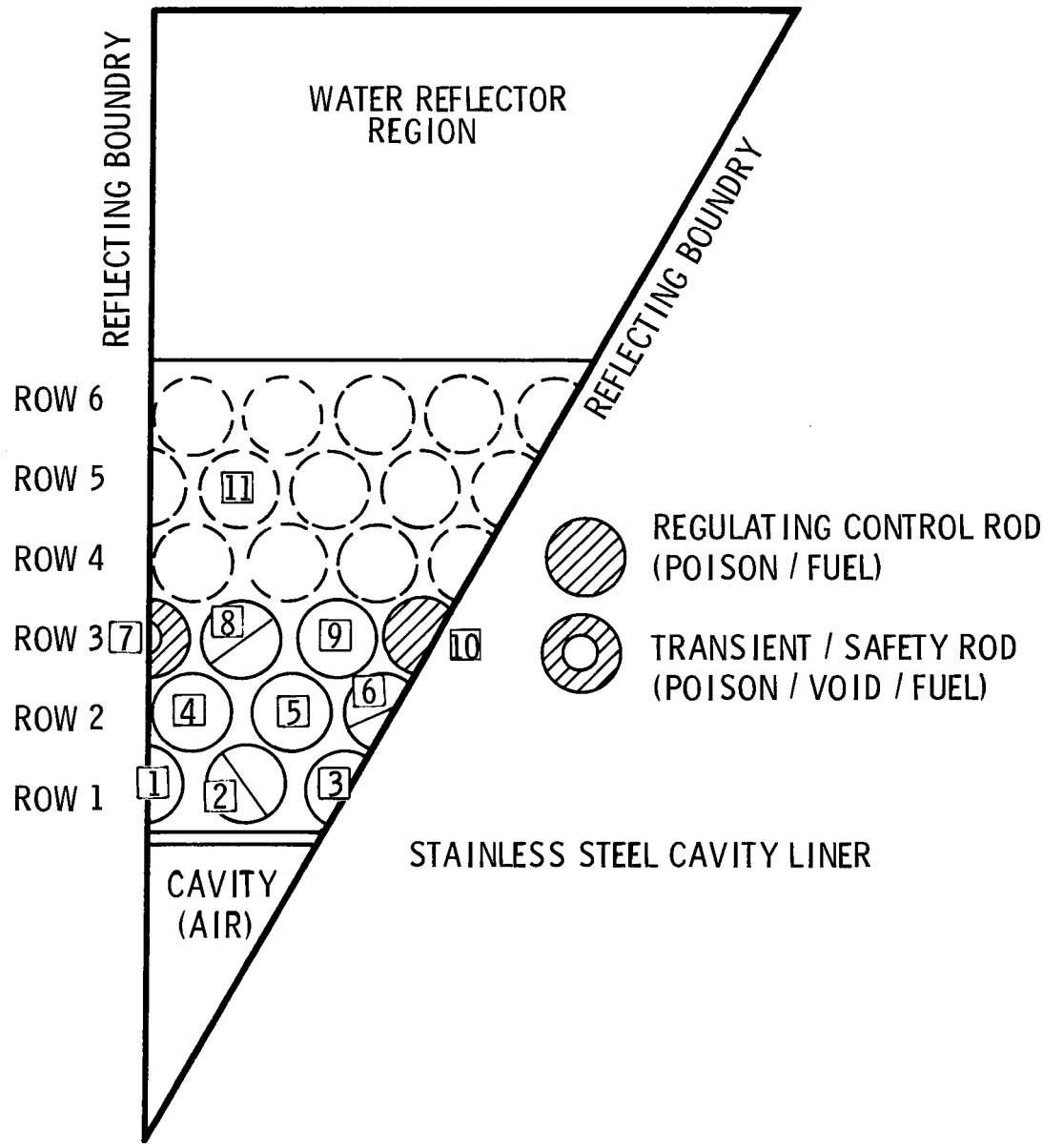

FIGURE 3.4-3. HEXAGONAL CORE MODEL USED IN MONTE CARLO ANALYSIS OF CELL FISSION DENSITY PEAKING FACTORS.

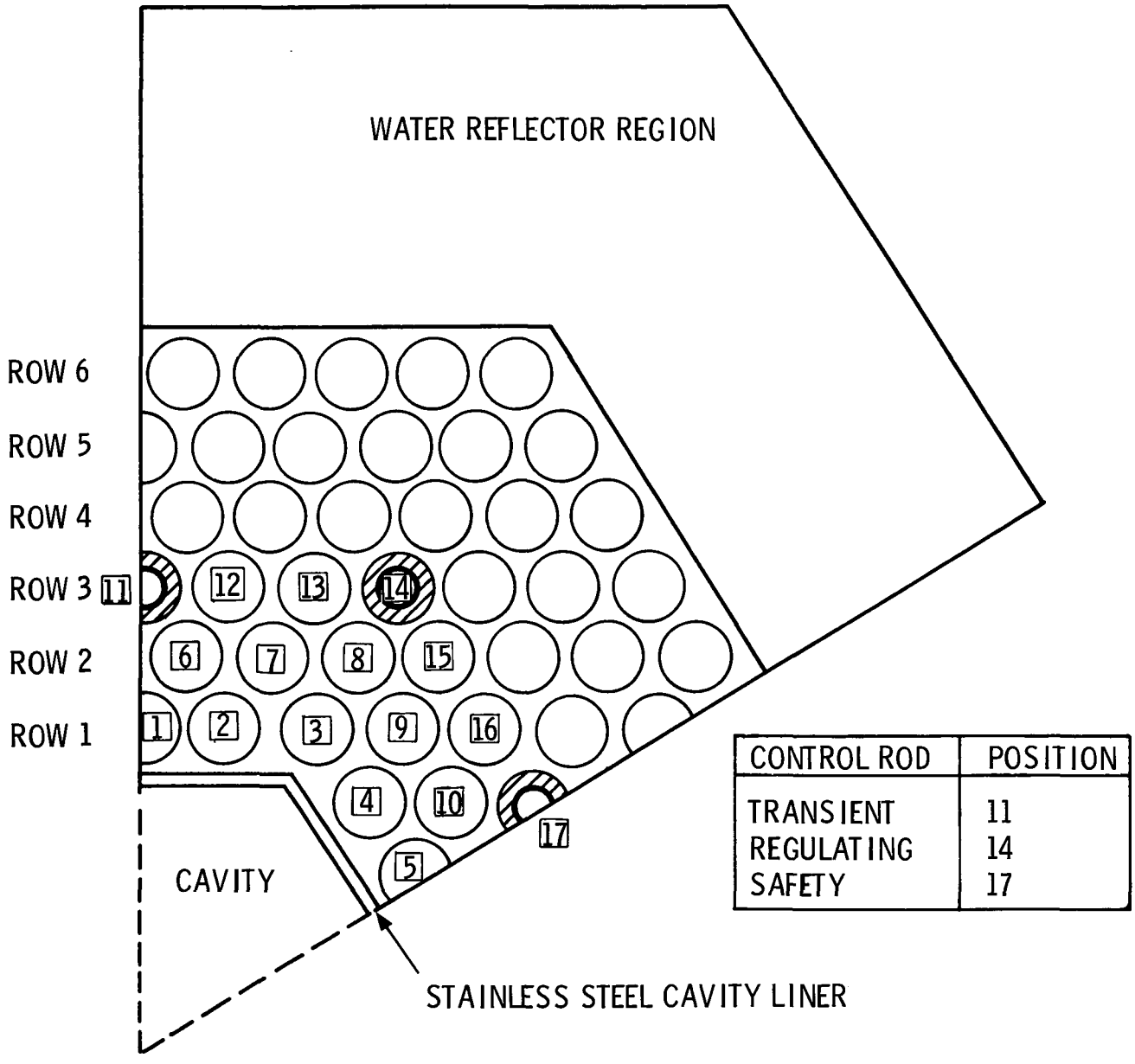

CONTROL ROD	POSITION
TRANSIENT	11
REGULATING	14
SAFETY	17

FIGURE 3.4-4. HEXAGONAL CORE MODEL USED IN MONTE CARLO ANALYSIS OF CELL AVERAGE TO CORE AVERAGE FISSION DENSITY RATIOS.

3.4-1. Three basic configurations were examined for a) regulating rod bank in, b) regulating rod bank out, and c) 2.54 cm polyethylene moderator in the cavity (rod bank out). All cases modeled a transient rod void and a safety rod fuel position. The highest average cell fission density occurs in the a row 2 element adjacent the transient rod void with a cell-to-core average of 1.46 with the regulating rod bank in. The fission density at this position is highest due to excess water in the transient rod cell in comparison with other elements. The effect of moderating experiments in the cavity primarily affects the row 1 elements, while the insertion of regulating rods tends to increase the average fission density on the hexagonal flats relative to the corner elements. These results have an associated statistical uncertainty of approximately 5.0%.

The results of the fission density cell profile calculations are summarized in Table 3.4-2. The most severe profiles occurring in the cells are in the elements adjacent the transient rod void followers when the regulating rods are fully in. A moderating experiment in the cavity of up to 1" of polyethylene does not produce a more severe profile in row 1 elements than occurs in Row 3, but the peak fission density does occur in row 1 due to the average fission density shift to row 1 under these conditions.

Calculated fission density profiles obtained for several representative fuel cell locations are shown in Figure 3.4-5. The overall core peak/average fission density values required for reactor kinetics studies and SAR analysis were determined from the data contained in Tables 3.4-1 and 3.4-2. Using the cell

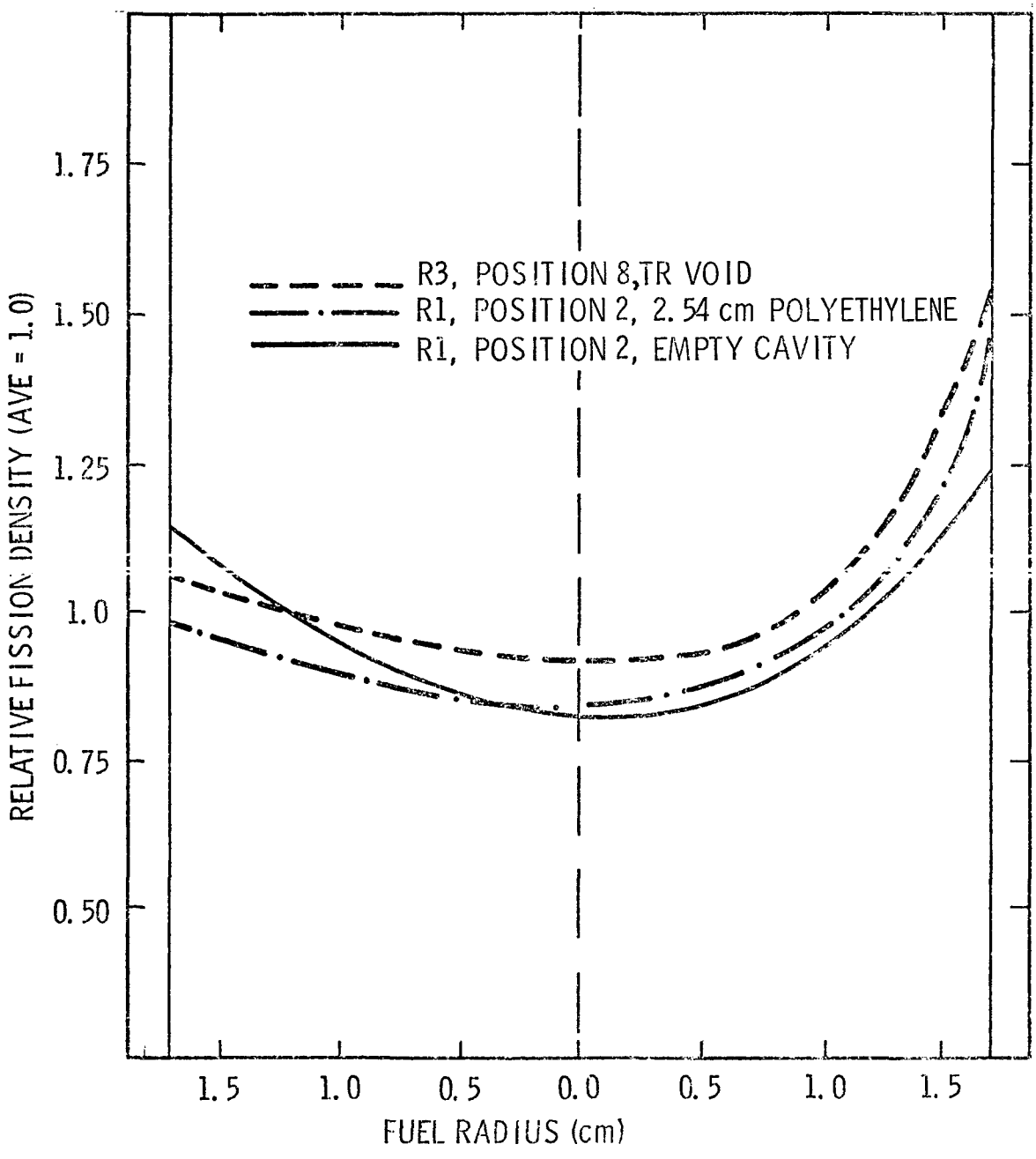

FIGURE 3.4-5. RELATIVE FISSION DENSITY PROFILES IN REPRESENTATIVE FUEL ELEMENT POSITIONS. (ALL PROFILES NORMALIZED TO AN AVERAGE FISSION DENSITY OF 1.0, MORSE - 9Grp.)

TABLE 3.4-1
CELL AVERAGE TO CORE AVERAGE FISSION DENSITY RATIOS A_{cell}/A_{core}

Cell Position Figure 3.4-4	Core Configuration		
	RR Bank Out Empty Cavity	RR Bank In Empty Cavity	RR Bank Out 2.54 cm Poly
	Cell Average/Core Average Fission Density		
1	1.28	1.40	1.31
2	1.31	1.35	1.38
3	1.37	1.38	1.35
4	1.31	1.37	1.35
5	1.27	1.41	1.23
Row 1 Average	1.32	1.38	1.35
6	1.35	1.46	1.28
7	1.23	1.25	1.16
8	1.19	1.07	1.12
9	1.22	1.25	1.18
10	1.23	1.30	1.17
Row 2 Average	1.24	1.38	1.19
11	Void	Void	Void
12	1.27	1.36	1.26
13	1.10	0.99	1.06
14	0.96	Poison	0.98
15	1.12	0.91	1.09
16	1.10	1.17	1.18
17	1.15	1.21	1.16
Row 3 Average	1.11	1.11	1.12
Rows 4,5,6 Average	0.82	0.80	0.83

TABLE 3.4-2

FISSION DENSITY PEAKING FACTORS FOR
ACPR UPGRADE FUEL CELLS
(MORSE, 9 Grp, Hexagonal Lattice)

Row	Position (Fig. 3.4-3)	P/A Fuel Cell	Core Configuration			
			TR	SR	RR	Cavity (Empty/Poly)
1	1	1.28	--	out	out	Emp
1	1	1.37	--	out	out	1.27 cm
1	1	1.42	--	out	out	2.54 cm
1	1	1.28	--	out	in	Emp
2	6	1.31	--	out	in	Emp
2	6	1.24	out	--	in	Emp
2	4	1.40	out	--	out	Emp
3	8	1.47	out	--	out	Emp
3	8	1.51	out	--	in	Emp
3	8	1.25	--	out	out	Emp
3	8	1.25	--	out	out	1.27 cm
3	8	1.26	--	out	out	2.54 cm
3	8	1.25	--	in	out	Emp

fission density profiles from Table 3.4-2, and applying these factors to the average cell-to-core fission density ratio of Table 3.4-1, results in a core peak-to-average fission density or power factor. The calculated core peak-to-average values are given in Table 3.4-3 for representative cell locations and core configurations. The most severe peaking occurs in the vicinity of the transient rod void, although the highest average cell power may occur in row 1, depending on the position of the control rod banks. The approximate two-dimensional S_N calculations agree reasonably well with the monte carlo calculations. Kinetics calculations are summarized in Chapter 4 which give the core temperature peak/average when the effects of temperature equilibration and heat loss to the clad and coolant are included.

TABLE 3.4-3 CALCULATED CORE PEAK/AVERAGE FISSION DENSITY FACTORS

Calculations Type	Core Configuration	Cell*(P/A) (Radial)	$(P/A)^*_{Cell}$	A_{cell}/A_{core}	$(P/A)_{Core}$	Peak Position (Fig. 3.4-4)
S_8 - 300K	RR, SR, TR - OUT	1.24	1.59	1.29	2.05	Row 1
S_8 - 300K	ST, TR-OUT/RR-IN	1.24	1.59	1.39	2.21	Row 1
S_8 - 300K	RR, SR, TR - OUT	1.29	1.65	1.27	2.10	Row 1
MC - 300K	RR, SR, TR - OUT	1.28	1.64	1.37	2.25	3
		1.40	1.79	1.35	2.42	6
		1.47	1.88	1.27	2.39	12
MC - 300K	ST, TR-OUT/RR-IN	1.28	1.64	1.41	2.31	5
		1.40	1.79	1.46	2.61	6
		1.51	1.93	1.36	2.62	12
MC - 300K	RR, SR, TR - OUT	1.42	1.82	1.38	2.51	2
	(2.54 cm Poly)	1.40	1.79	1.28	2.29	6
		1.47	1.88	1.26	2.37	12

*Axial P/A = 1.28 (all cases)

3.5 Neutronic Performance Calculations

Pulse and steady-state performance estimates were made from both S_N and monte carlo calculations. Performance estimates obtained from static calculations were generally based on flux/-unit power or fluence/unit energy yield. Temperatures assigned to a given transient energy release in these cases are based only on heat capacity and represent an adiabatic temperature. A separate heat transfer calculation is required to provide an estimate of the actual temperature occurring during the pulse. Coupled neutronic-heat transfer calculations have been done to augment the performance and temperature estimates obtained from static calculations, and these results are summarized in Chapter 4.

The heat capacity of the UO_2-BeO fuel material is shown in Figure 3.5-1. The heat capacity was calculated from literature data for UO_2 and BeO. The results were obtained for 21.5 w/o UO_2 in BeO with both constituents at 99% of theoretical density. The small UO_2 particle size ($\simeq 1\mu$) and uniform dispersal allowed full credit to be taken for the BeO matrix heat capacity during the few msec wide pulses.

The energy available from fission is approximately 200 MeV, of which 190 MeV/fission was assumed to be effective in heating the fuel material during the millisecond time frame of the pulse. Steady-state power generation rates were based on 200 MeV/fission.

Pulse fluence estimates determined from S_N and monte carlo results are summarized in Table 3.5-1. The monte carlo and higher quadrature order S_N results agree reasonably well and represent the more accurate models. The peak/ave factors used to obtain

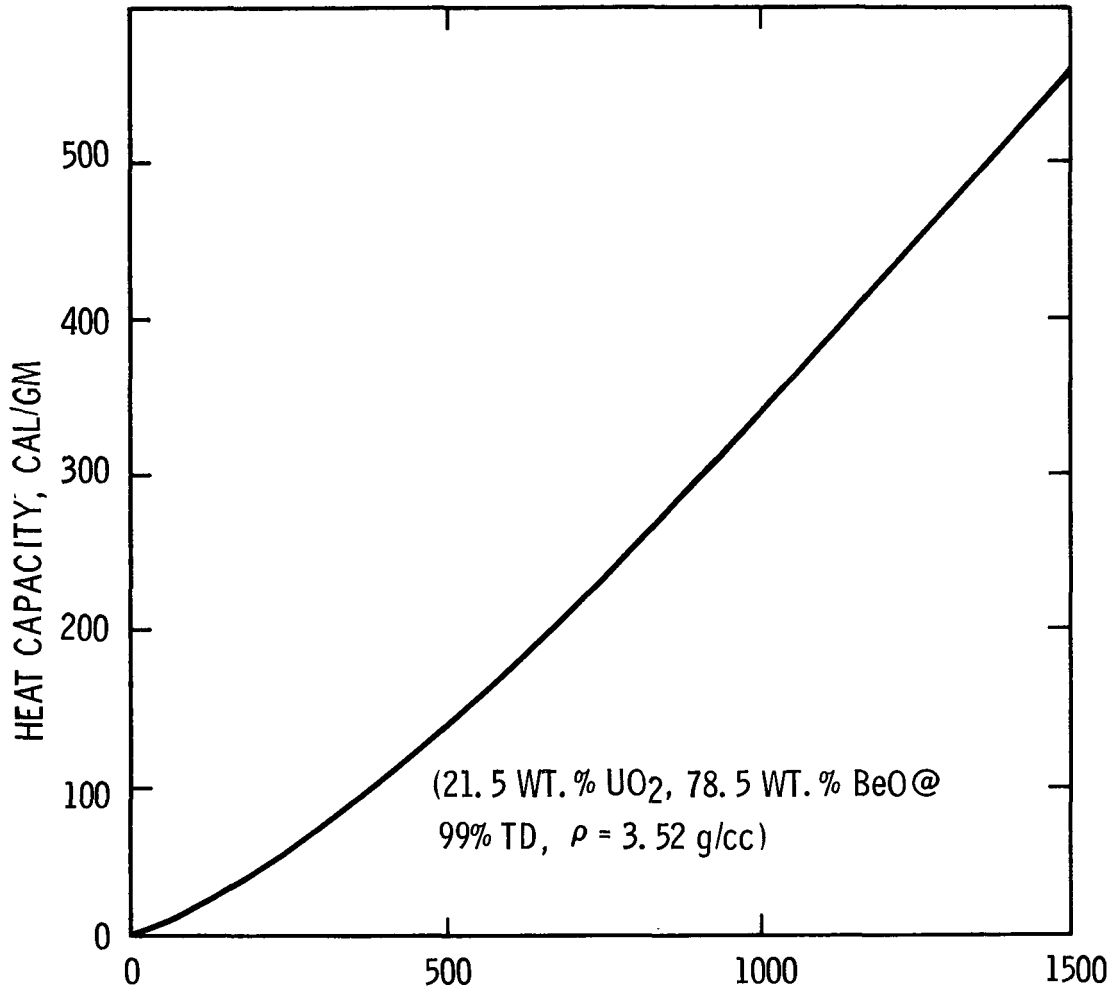

FIGURE 3.5-1 HEAT CAPACITY OF BeO-UO_2 FUEL

TABLE 3.5-1

PULSE FLUENCE CALCULATIONS FOR ACPR UPGRADE

Calculational Model	Cavity Fluence*/Yield (n/cm^2/MW-sec)	Cavity Fluence* (n/cm^2) 300 MW-sec	Adiabatic Temperature Rise 300 MW sec (198 Element Core) ΔT_{Ave} (°C)	Adiabatic Temperature Rise 300 MW sec (198 Element Core) ΔT_{Max} (°C)	Core Peak/Ave (Table 3.4-3)
2D-S_4-P_1-9G (300 K)	1.76×10^{13}	5.27×10^{15}	730°C (3465)	1380°C (7380)	2.13
2D-S_4-P_1-9G (700 K)	1.81×10^{13}	5.41×10^{15}	730°C (3465)	1390°C (7450)	2.15
2D-S_8-P_1-9G (300 K)	2.05×10^{13}	6.14×10^{15}	730°C (3465)	1340°C (7105)	2.05
2D-S_4-P_1-18G (300 K)	1.75×10^{13}	5.25×10^{15}	730°C (3465)	1380°C (7380)	2.13
2D Monte Carlo-9G (300 K)	2.0×10^{13}	6.00×10^{15}	730°C (3465)	1520°C (8385)	2.42

*Minimum Fluence at Cavity Centerline

the peak adiabatic temperature estimates are taken from Table 3.4-1.

Since a significant fraction of the total energy release occurs in the "tail" of the pulse, the actual peak temperatures calculated with heat transfer are reduced considerably from the adiabatic values shown in Table 3.5-1. (See Chapter 4.)

Estimates of steady-state performance were based on 200 MeV per fission using both S_N and monte carlo calculations. The results of these calculations are shown in Table 3.5-2. The temperatures occurring in the core as a function of power level are shown in Figure 3.5-2. The heat transfer model used for the ACPR Upgrade fuel element is described in detail in Chapter 4, Section 3.

TABLE 3.5-2

STEADY-STATE PERFORMANCE ESTIMATES FOR ACPR UPGRADE

Calculational Model	Flux/Power (n/cm^2-sec/MW)	Flux (n/cm^2 sec @2MW)
2D - S_4 - P_1 - 9G (300°K)	1.67×10^{13}	3.34×10^{13}
2D - S_4 - P_1 - 9G (900°K)	1.72×10^{13}	3.44×10^{13}
2D - S_8 - P_1 - 9G (300°K)	1.95×10^{13}	3.90×10^{13}
2D - Monte Carlo (300°K)	1.90×10^{13}	3.80×10^{13}

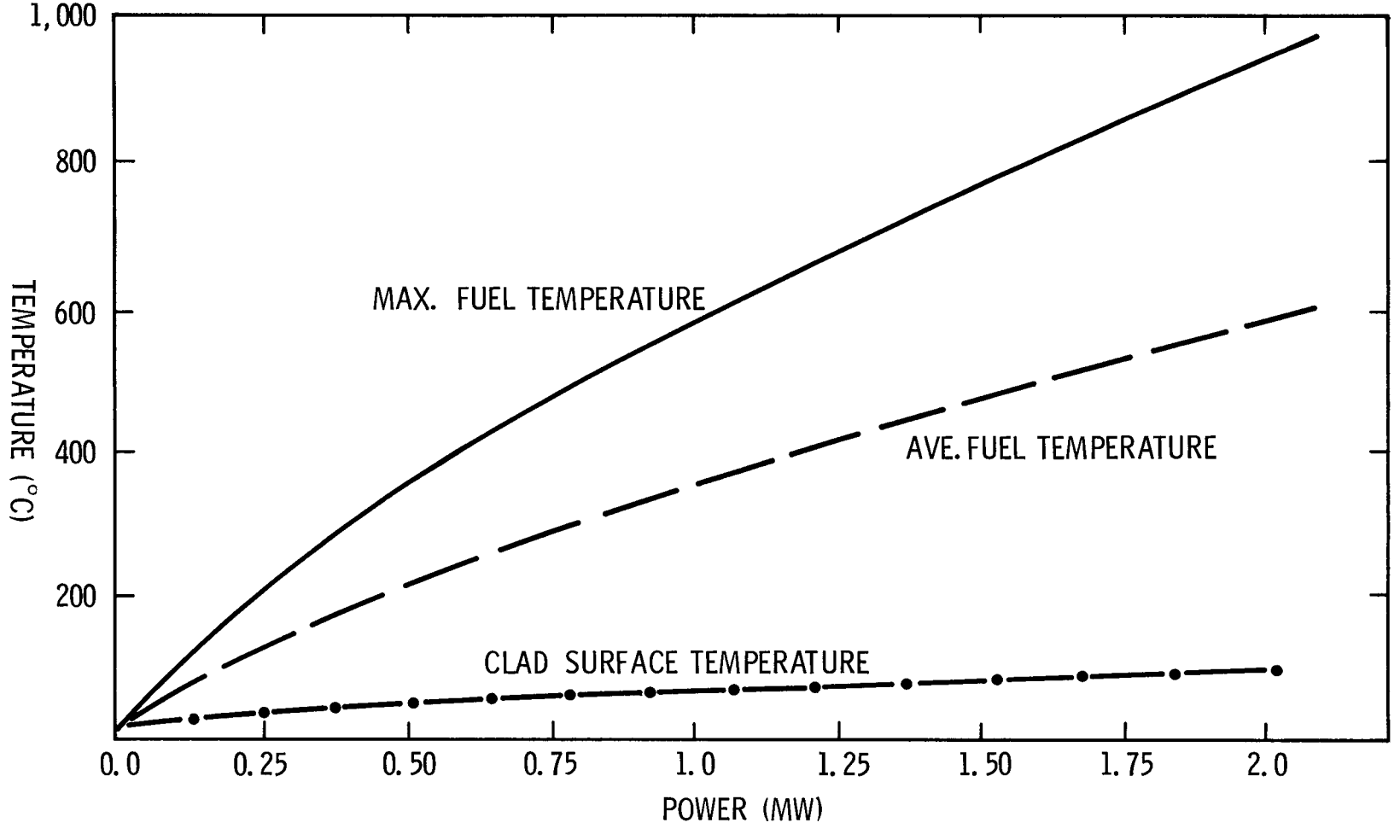

FIGURE 3.5-2. STEADY STATE FUEL AND CLAD TEMPERATURES (BASED ON HEAT TRANSFER MODEL OF CHAPTER 4, SECTION 3).

3.6 Prompt Temperature Coefficient of Reactivity

The prompt temperature coefficient of reactivity for the ACPR Upgrade is due primarily to Doppler broadening of ^{238}U resonances and the spectral shift caused by the prompt heating of the BeO matrix. The Upgrade fuel element design utilizing a niobium liner (cup) does not produce a significant overall prompt axial fuel expansion effect. The reactivity effect from the limited, prompt expansion has been examined, and it is not calculated to be significant in comparison with other reactivity feedback effects. Clad and liner expansion effects were not included in the overall prompt coefficient determination.

Coolant density and temperature effects arise from prompt γ-heating of the essentially stagnant coolant in the core region during the pulse. This effect is potentially a significant contributor to the overall prompt negative temperature coefficient, particularly if some coolant voiding occurs. The ACPR Upgrade core design is strongly undermoderated, and these effects will produce negative feedback in addition to that calculated for Doppler and spectral effects. These coolant temperature feedback effects will be discussed later in this Section.

Temperature-dependent cross sections required for the calculation of temperature reactivity effects were calculated with AMPX using ENDF/B cross section data. Cell-weighted cross section sets were for temperatures of 300, 900, and 1200 K. Low mass number materials, H, Be, O, were computed with the appropriate thermal scattering kernals. Resonance calculations were performed for ^{235}U and ^{238}U for each temperature set. A

cell-weighting calculation was performed for each temperature. The cross sections were collapsed over the cell spectrum to 9 and 18 group sets.

Although there is some uncertainty in any of the cross sections used in these calculations, the BeO thermal cross sections may be particularly significant. These thermal cross sections do not significantly affect estimates of core eigenvalue, fission density, flux, or neutron generation times but primarily influence estimates of temperature feedback efects. There appears to be no experimental data which would allow definitive confirmation of the accuracy of the cross section data used in the temperature dependent calculations. Three cross section sets were generated and used to provide estimates of the temperature coefficient of reactivity. Two of these sets were based on the BeO (molecular) scattering kernal, and the third was based on Be and oxygen scattering data from an older data set distributed by RSIC with the XSDRN cross section code.

The fuel temperature reactivity coefficient was calculated using both TWOTRAN and the one-dimensional diffusion code SAK.

The reactivity temperature results obtained from 2D S_N calculations used uniform temperature cross section sets for the entire core. The core average temperature is taken as the temperature of the cross section set.

The results obtained from the one-dimensional diffusion analysis provides temperature distributed cross sections based on an interpolation table for the cross sections. The diffusion results display the same temperature dependence but give generally 5%

higher results for the fuel reactivity coefficient. The results of these calculations are summarized in Table 3.6-1. The temperature dependence of these negative temperature coefficients is shown in Figure 3.6-1 for the BeO cross section sets. The range exhibited by these calculations (-0.38 → -0.48¢/°C) is about 20%. In view of the lack of experimental data available to verify these results, the approach taken in the Upgrade core design has been to utilize both the lower and intermediate values for kinetics studies.

The analytic forms of the feedback functions based on fuel temperature effects are given below.

$$\alpha_{Fuel}(¢/°C) = -0.50 + 0.00017\Delta T \ , \qquad (BeO - 1)$$

$$\alpha_{Fuel}(¢/°C) = -0.43 + 0.00012\Delta T \ . \qquad (BeO - 2)$$

Kinetics calculations for the ACPR Upgrade are summarized in Chapter 4.

Calculations were also performed to evaluate the void coefficient of reactivity and the bulk coolant temperature coefficient. The void coefficient was calculated by assuming a uniform void distribution throughout the core. This calculation provides an estimate of the discrete void coefficient as long as the void does not significantly alter core homogeneity. Unique cell cross sections were generated for each void fraction and the results can be summarized by the relation,

$$\alpha_{void} = -35¢/(\% \text{ coolant void})$$

TABLE 3.6-1

FUEL TEMPERATURE COEFFICIENT OF REACTIVITY* FOR ACPR UPGRADE USING VARIOUS CROSS SECTION SETS AND ANALYTIC MODELS

Calculation	Cross Section Set	Temperature Range (°C)	α(¢/°C)
(R-Z), S_4, P_1 9 Grp	BeO-1	27 - 627°C	-0.44
(R-Z), S_4, P_1 18 Grp	BeO-1	27 - 627°C	-0.45
1D - Diffusion 5 Grp	BeO-1	27 - 627°C	-0.48
(R-Z), S_4, P_1 9 Grp	BeO-2	27 - 627°C	-0.38
(R-Z), S_4, P_1 9 Grp	BeO-1	627 - 927°C	-0.35
(R-Z), S_4, P_1 9 Grp	BeO-2	627 - 927°C	-0.33
(R-Z), S_4, P_1 9 Grp	Be	27 - 627°C	-0.47

*Based on Doppler broadening and thermal spectral effects.

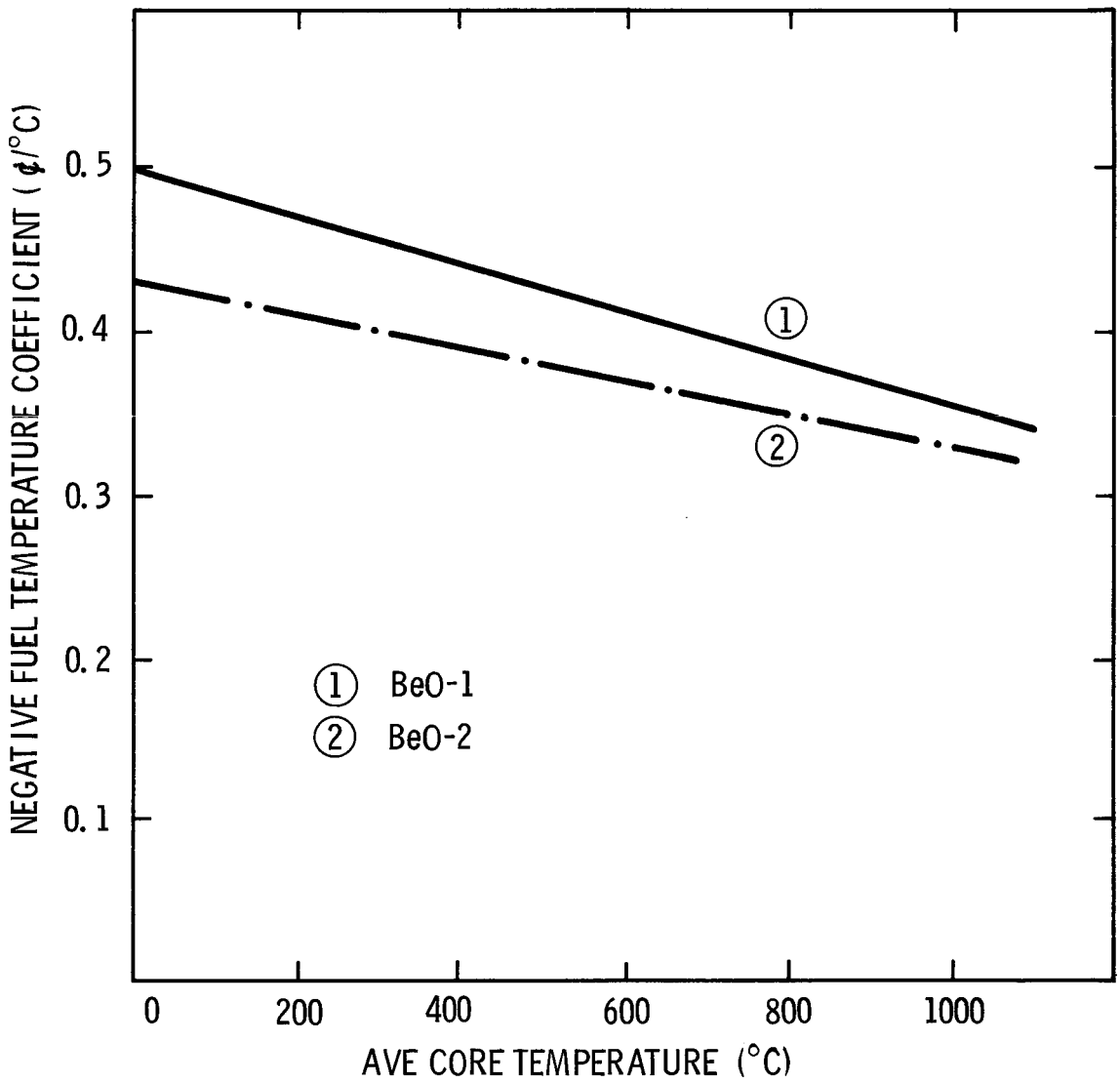

FIGURE 3.6-1. PROMPT NEGATIVE FUEL TEMPERATURE COEFFICIENT OF REACTIVITY DUE TO DOPPLER AND SPECTRAL EFFECTS FOR ACPR UPGRADE (TWØTRAN, S4, P_1, 9Grp.)

The coolant temperature coefficient due to thermal spectrum changes was calculated using two cell cross section sets with water at 300°K and 375°K. The results can be described by

$$\alpha_{coolant} = -0.70 \text{ (¢/°C rise in coolant temperature)}$$

An approximate value for the total (spectral hardening and coolant density) negative temperature effect due to coolant heating can be estimated from the above two coefficients to be,

$$\alpha_{coolant} = (-0.7)_{spectral} + (-1.70)_{density}$$

$$= -2.40 \text{ (¢/°C rise in coolant)}$$

where an average value of 0.049%/°C decrease in coolant density has been used.

Although the actual contribution of the coolant temperature and density effects to the overall negative temperature coefficient depend to some degree on the actual transient under consideration, it is apparent that the additional negative feedback from coolant/-moderator effects can be significant. A preliminary estimate of the effect of gamma heating of the coolant during a single pulse can be made based on approximate gamma heating estimates. Assuming the gamma heating per unit energy release in the core to be similar to the hydride core, a value of 0.15°C/MJ is obtained. The ACPR Upgrade core design results in approximately 2°C average adiabatic temperature rise in the fuel per MJ of core energy release. Gamma heating effects in the coolant result in an approximate ratio of 0.075 for coolant-to-core fuel temperature rise.

The total contribution to the prompt negative temperature coefficient from gamma heating of the coolant is then estimated to be,

$$\alpha_{\substack{\text{prompt} \\ \text{moderator}}} \cong -0.18 \text{ ¢/°C} .$$

The total negative temperature coefficient in the core is the sum of the fuel and moderator temperature effects and is estimated to be in the range of -0.56 to -0.66 ¢/°C for the range of 27-627°C indicated in Table 3.6-1. These estimates assume stagnant coolant and are therefore not necessarily applicable to slow transients. More sophisticated models for the correct treatment of both fuel and moderator temperature feedback effects should be developed for specific operational modes.

3.7 Neutron Generation Time

The neutron generation time was calculated with monte carlo techniques in R-Z geometry. The effect of core temperature, control rods, and cavity moderation were also examined. The results of these calculations are summarized in Table 3.7-1. All results listed in Table 3.7-1 utilized 9 group cell-weighted cross sections. The 300°K, empty cavity result of 24 μsec has been used in point kinetics analysis for the ACPR Upgrade. The effect of temperature on the calculation of the generation time is small, and temperature effects were neglected in kinetics calculations.

The sensitivity of the neutron generation time to changes in fissile loading is also shown in Table 3.7-1. A change in fissile loading of 0.5 w/o UO_2 results in approximately a 5% change in the calculated generation time. Since fuel composition is expected to have significantly better tolerance than 0.5 w/o UO_2, the effect on reactor kinetics was neglected.

The presence of the nickel reflector elements at the outer edge of the fuel results in a reduction in the number of slow reflector neutrons which reenter the core and cause a reduction in the generation time. If the nickel elements are removed and replaced with a water-filled region, the generation time increases to 35.4 μsec. Additional studies of reflector effects are in in Section 3.10.

TABLE 3.7-1

ACPR UPGRADE NEUTRON GENERATION TIME

(KENO-II - 9 Grp)

Core Configuration	Neutron Generation Time (μsec)	Multiplication Constant
300°K - Empty Cavity	24.0	1.056 ± 0.006
900°K - Empty Cavity	23.4	1.014 ± 0.005
300°K - 1.5 cm Poly Annulus in Cavity	27.0	1.051 ± 0.006
300°K - 2.5 cm Poly Annulus in Cavity	27.3	1.033 ± 0.005
300°K - $8.5 Control Rod Bank in Core	23.8	0.995 ± 0.006
300°K - Water Reflector	35.4	1.064 ± 0.006
Fissile Loading Sensitivity 300°K		
20 w/o	26.4	1.053 ± 0.005
21.5 w/o	24.0	1.056 ± 0.006
23.0 w/o	22.4	1.062 ± 0.006

3.8 Neutron Energy Spectrum

The neutron energy spectrum for the ACPR Upgrade was calculated with 2D - S_N analysis using 9- and 18-group cross section sets. The energy group structure for these sets is shown in Table 1.5-1. The empty cavity neutron energy spectrum for the ACPR Upgrade is shown in Figure 3.8-1. The fraction of neutrons in the empty cavity at energies greater than E are plotted vs. E in Figure 3.8-2. The fraction of neutrons in the cavity greater than 10 keV is 0.58. The effect of temperature on the neutron energy spectrum at low neutron energies is shown in Figure 3.8-3 for a 9-group calculation. The lowest energy group (< 0.06 eV) is depleted in neutrons and serve as a source for the two higher energy groups increase. (This effect is responsible for about one-third of the negative temperature coefficient from fuel temperature effects.)

The differential energy flux spectrum for the ACPR Upgrade is shown in Figure 3.8-4. The 18-group cross section set was used with an S_4, P_1 TWOTRAN R-Z model for this calculation. The differential flux spectrum is reasonably well characterized by a 1/E dependence over most of the energy range.

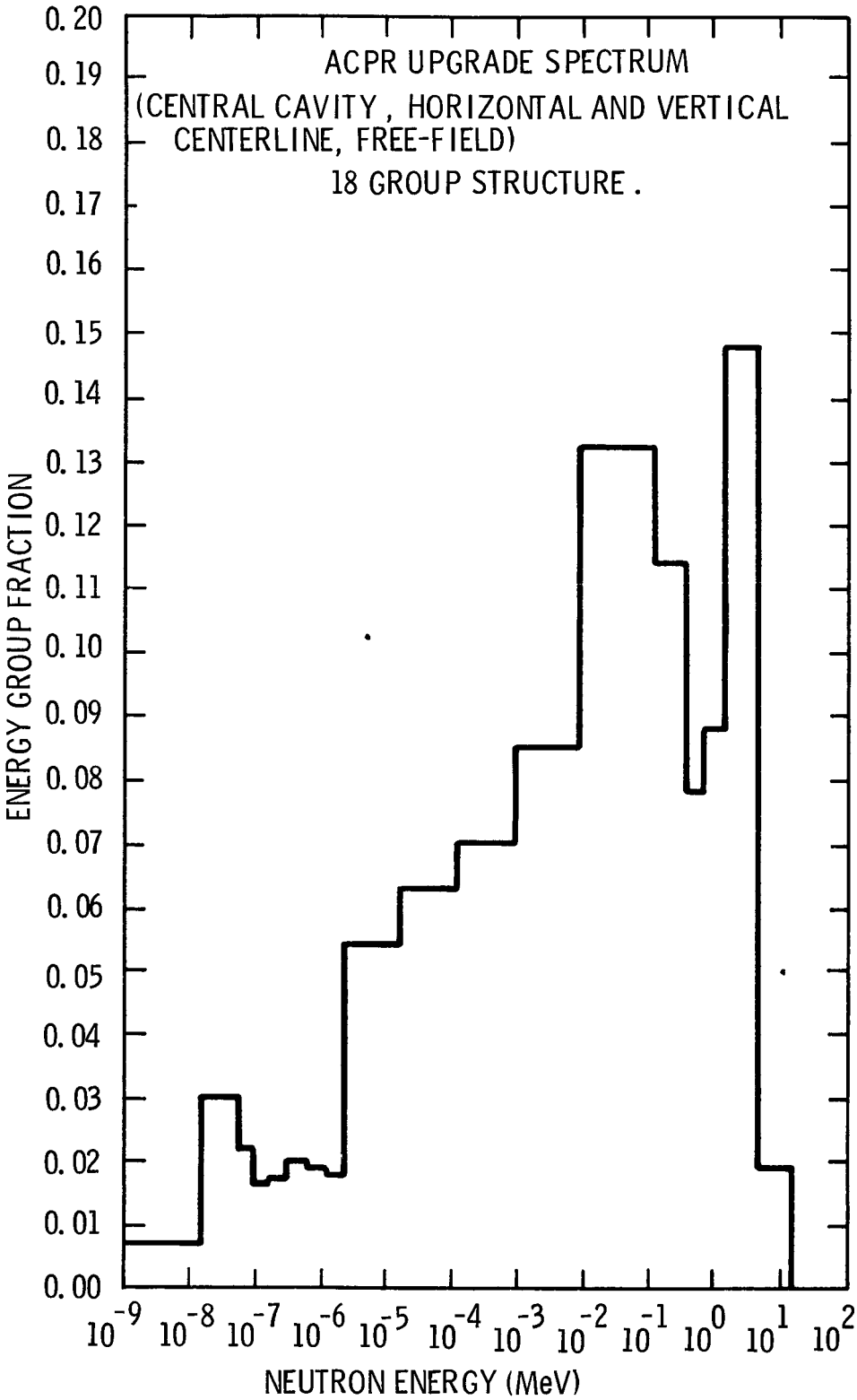

FIGURE 3.8-1. CAVITY FLUX SPECTRUM IN ACPR UPGRADE (TWØTRAN-S_4, P_1, 18Grp.)

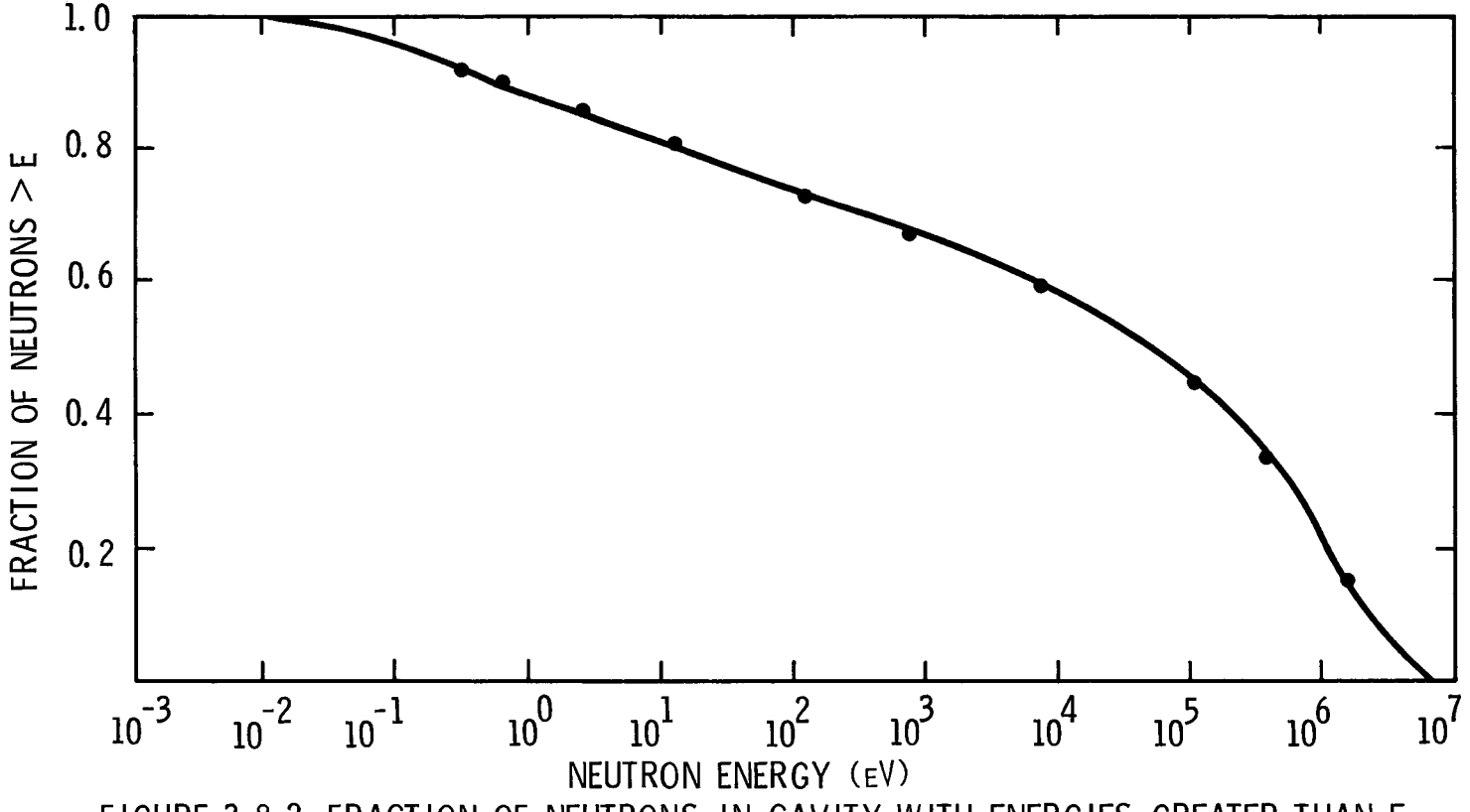

FIGURE 3.8-2. FRACTION OF NEUTRONS IN CAVITY WITH ENERGIES GREATER THAN E.

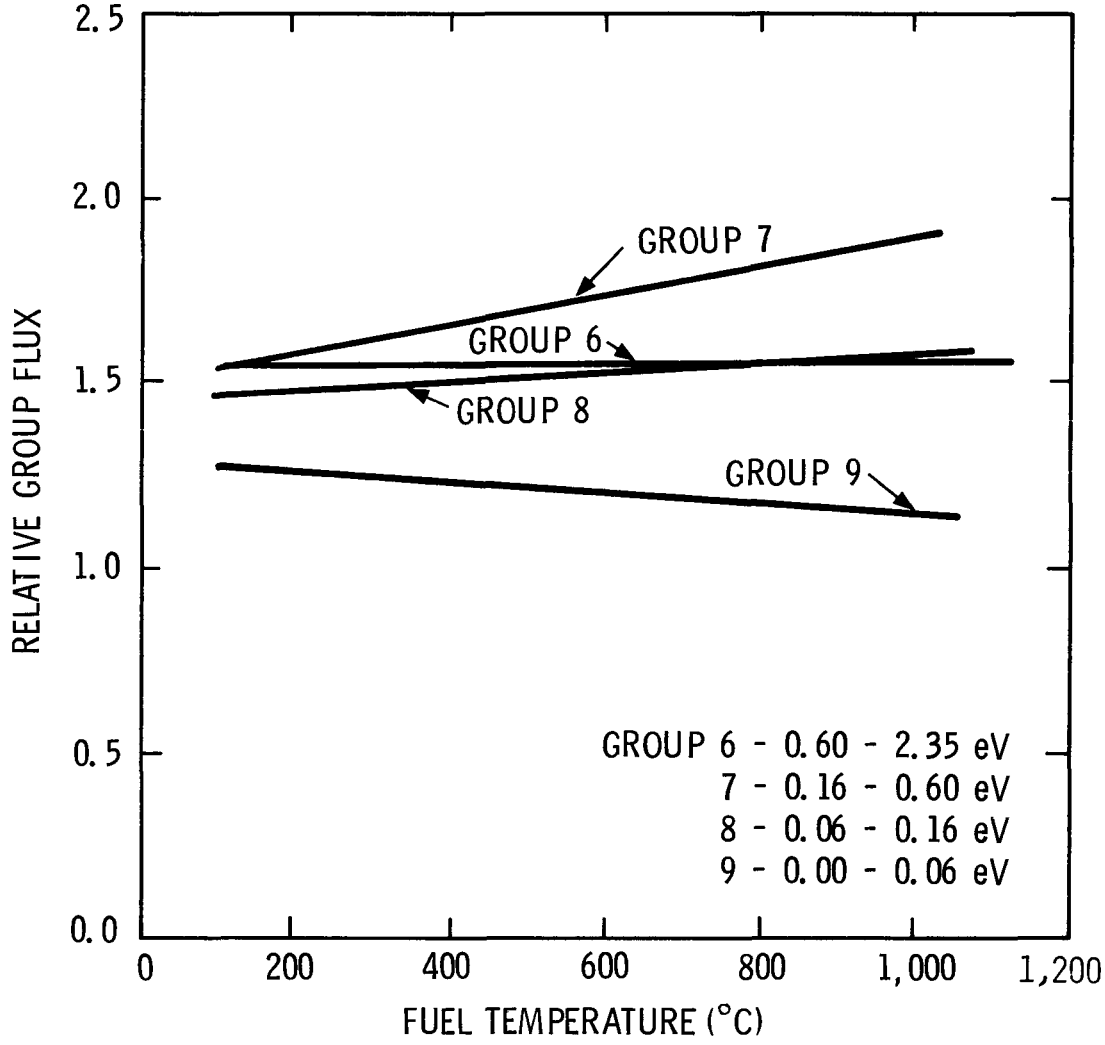

FIGURE 3.8-3. TEMPERATURE EFFECT VERSUS ENERGY DEPENDENT FLUX IN FUEL REGION.

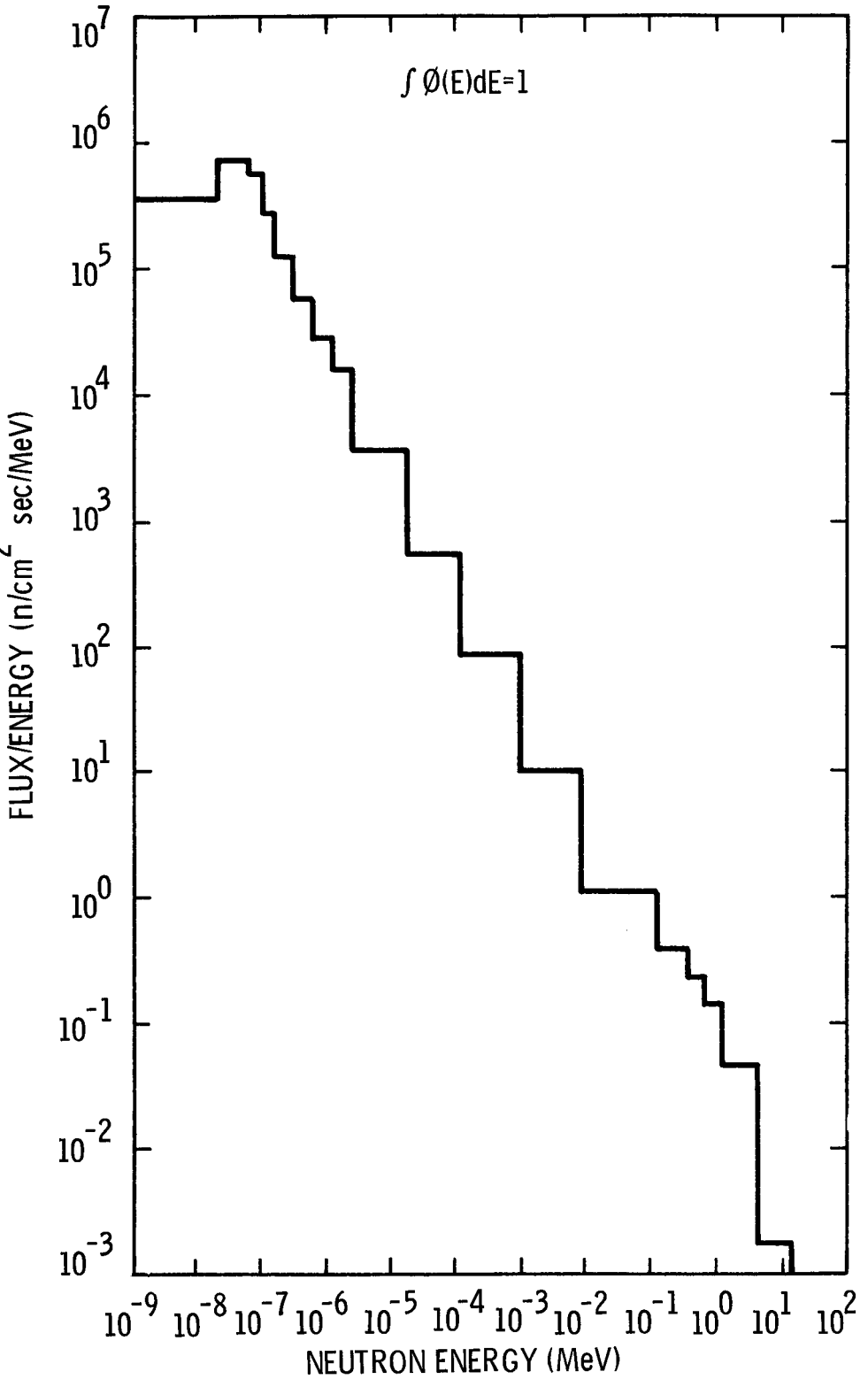

FIGURE 3.8-4. DIFFERENTIAL ENERGY FLUX FOR ACPR UPGRADE

3.9 Control Rod Worth Calculations

The ACPR Upgrade has 11 control elements located in the third hexagonal row. There are 6 fuel followed regulating rods located on the hexagonal corners, and 3 void followed transient or pulse rods located on alternate hexagonal flats. Of the 3 remaining hexagonal flat positions, 2 positions are utilized for fuel followed safety rods. The maximum desired worths for the control rods are:

Regulating -- \$12.00, (6 Rods),

Transient -- \$ 3.20, (3 Rods),

Safety -- \$ 2.50. (2 Rods).

Calculations of rod worth were performed with both S_N and monte carlo codes. The treatment of the correct geometry was considered to be the most important aspect of the analysis and the monte carlo calculations were given the highest priority.

A schematic diagram of the regulating and transient rod calculational models is given in Figure 3.9-1. The safety rod is modeled as a regulating rod with a different radius poison section. The monte carlo analysis modeled the rod bank as opposed to individual rods to improve statistics. The poison composition was B_4C at 95% of theoretical density.

The results of the control rod studies are plotted in Figure 3.9-2 as a total bank worth vs. radius of the poison section. The regulating rods require a poison section radius of 1.6 cm to maintain a bank worth of \$12.00. Although the statistical uncertainty is large, the lower end of the regulating curve indicates the worth of fuel vs. void on a third row corner is

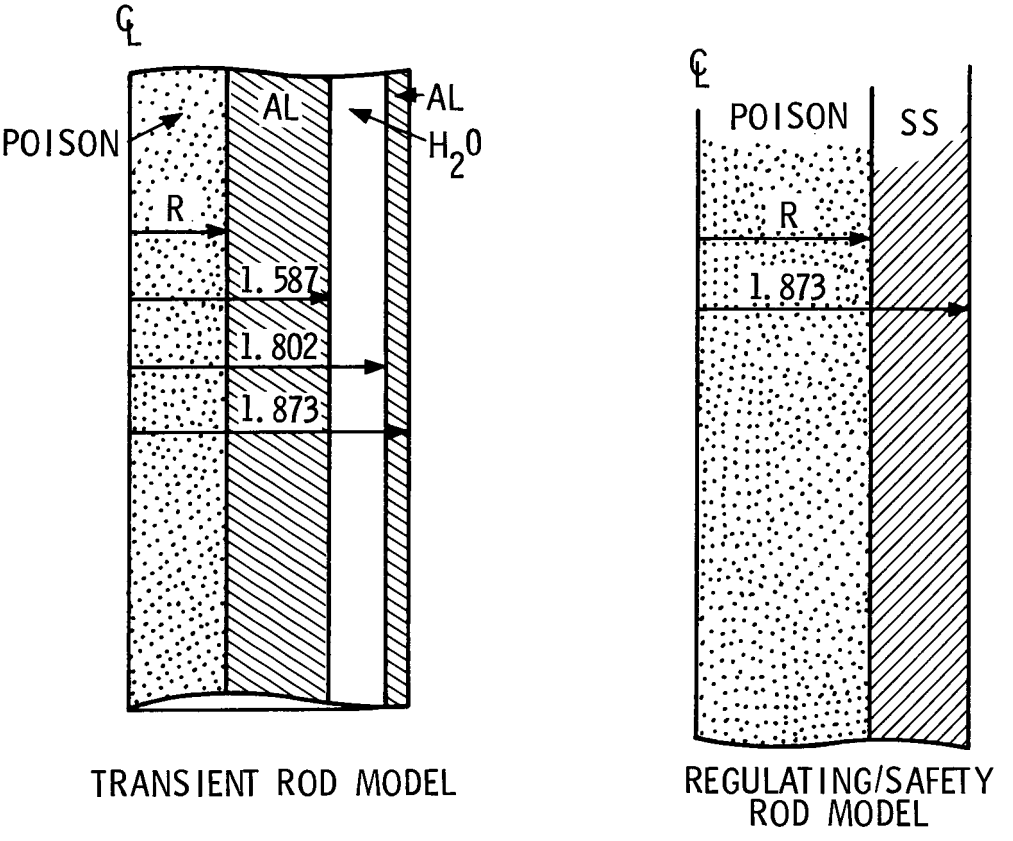

FIGURE 3.9-1. CALCULATIONAL MODELS FOR ACPR UPGRADE CONTROL ELEMENTS

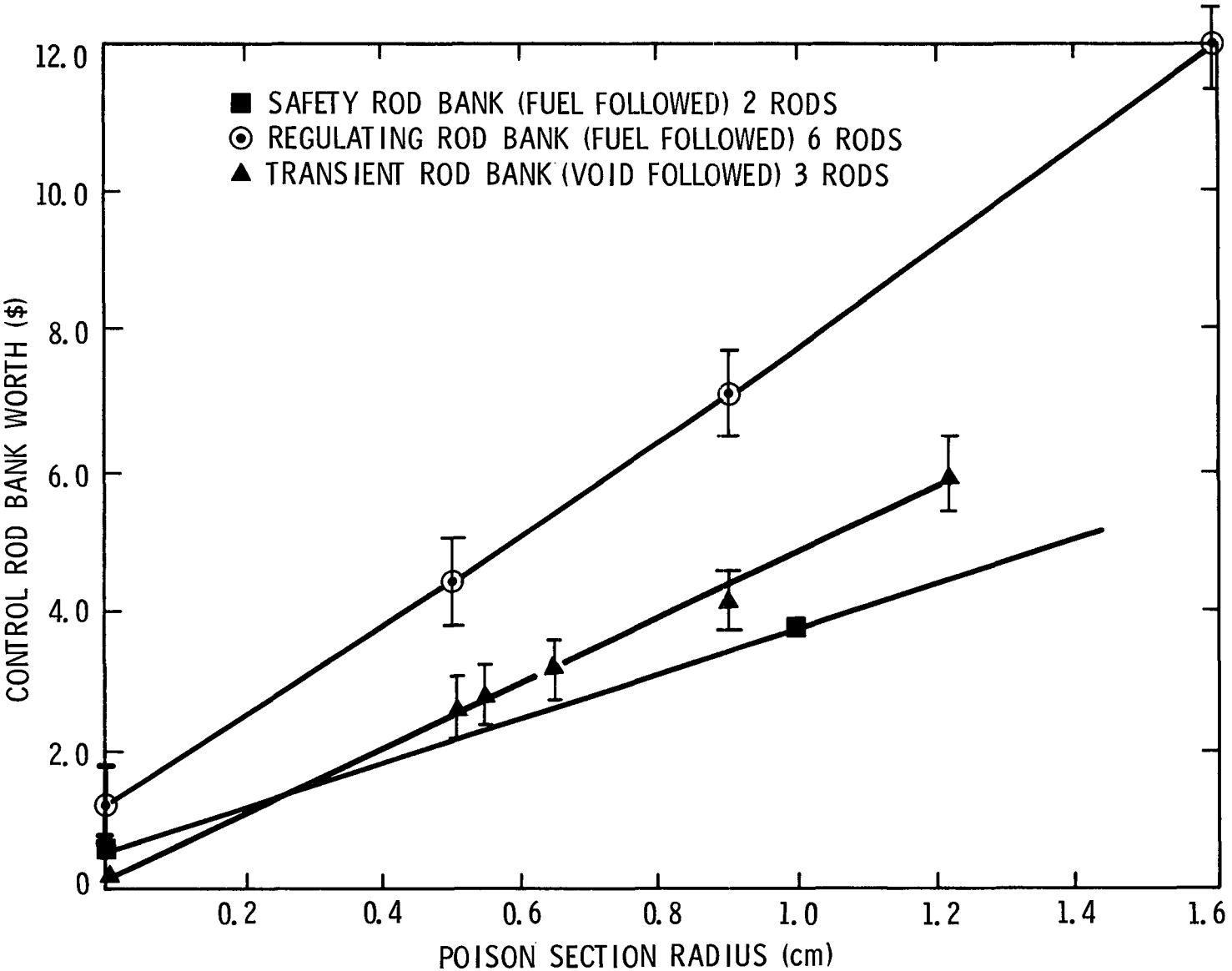

FIGURE 3.9-2. HEXAGONAL LATTICE MONTE CARLO CALCULATIONS FOR ACPR UPGRADE CONTROL BANK REACTIVITY WORTH.

approximately $0.20. The transient rod bank worth of $3.20 requires a poison radius of only 0.65 cm. The safety rod poison section utilizes the transient rod poison section. The final control rod poison sections were designed to somewhat lower reactivity worths for the initial core configuration using values of 0.57 cm and 1.46 cm for the transient and regulating rod poison sections, respectively. These radii correspond to bank worths of $11.0, $2.8, and $2.5 for the regulating, transient, and safety rod banks, respectively.

The shape of the axial reactivity worth curve for the regulating rod bank was examined by homogenizing the 6 rods in a 2D,R-Z TWOTRAN calculation. The worth curve obtained from this approach is shown in Figure 3.9-3. This calculation estimates the maximum differential reactivity worth to be about 1.85 times the average differential reactivity worth. The total reactivity worth of the regulating rod bank in this homogenized calculation was $12.56 due to approximate cross section weighting utilized.

The effect of the homogenized regulating rod bank on the homogenized core peak/average fission density is shown in Figure 3.9-4. The unperturbed core peak/average for the model used was 1.70. The effect of operation with the regulating rod bank approximately 50% withdrawn is to increase the core peak fission density about 8% for a given energy release.

As mentioned previously, monte carlo results were used to establish predicted values of the regulating and transient rod bank worths since discrete rods and the correct hexagonal geometry could be modeled. In evaluating the relatively small changes that

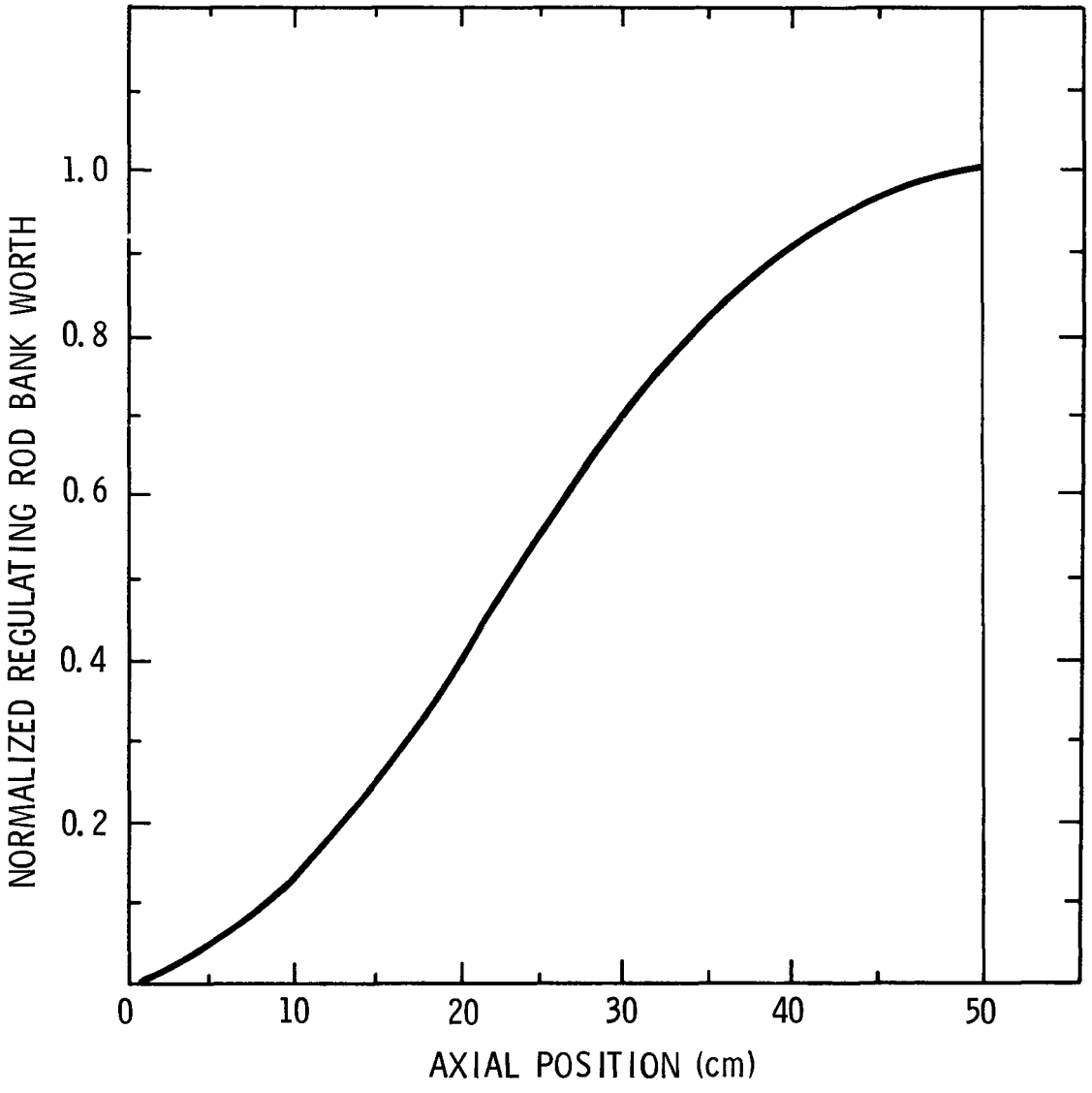

FIGURE 3.9-3. NORMALIZED REACTIVITY VS AXIAL POSITION FOR ROD BANK.

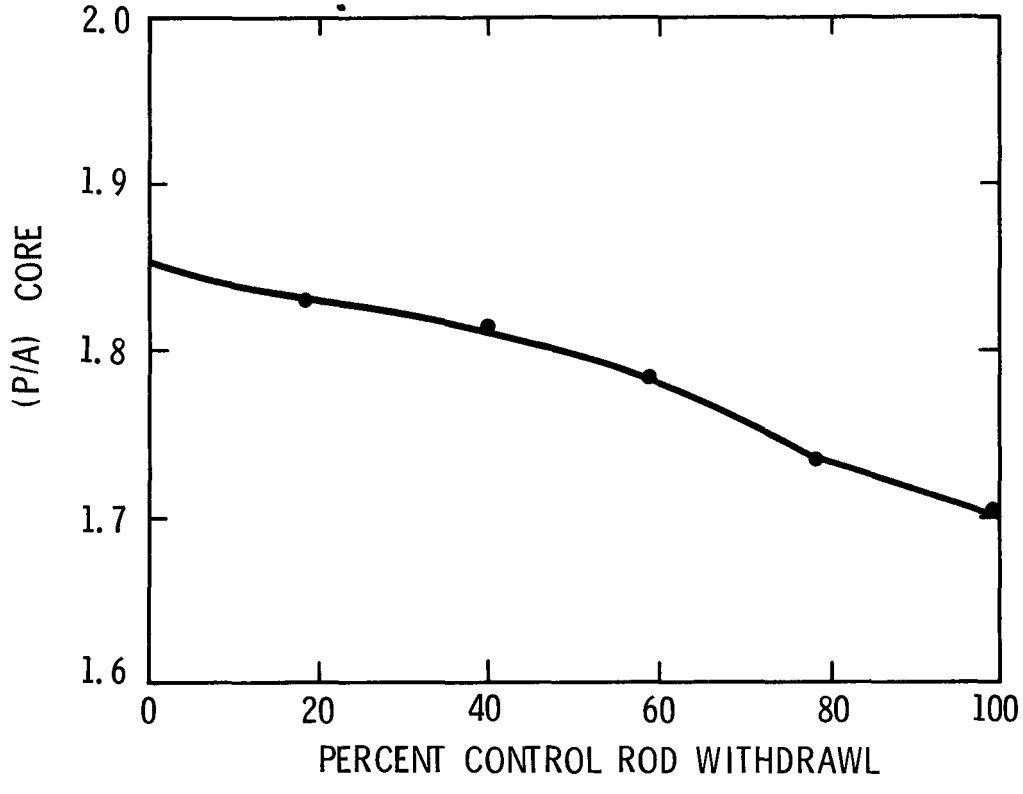

FIGURE 3.9-4. EFFECT OF REGULATING ROD BANK POSITION ON OVERALL CORE PEAK/AVERAGE FISSION DENSITY FOR HOMOGENIZED CORE. (R-Z, S_4, P_1).

occur in the reactivity worth of a rod due to core size or configuration, the statistical uncertainty of the monte carlo analysis becomes significant for reasonable computing times. The sensitivity to these effects was examined using two-dimensional discrete ordinates methods in an R-θ geometry. In addition to comparative calculations for regulating, transient, and safety bank reactivity worths, the effects of core size, control or transient bank asymmetry, cavity experiments and reflector configuration on calculated bank worths were also examined.

The model used in the R-θ control rod calculations is shown schematically in Figure 3.9-5. Cavity liner, fuel, and reflector boundaries are assigned to preserve the correct amount of material present in the core. Poison section dimensions are assigned so that the annular section representing the poison element in R-θ geometry contains the same amount of poison as the actual cylindrical poison rod. The regulating and transient positions are located at the correct distance from core center to represent the hexagonal corner and flat, respectively. The design poison section radii used for these sensitivity calculations were 0.57 cm and 1.46 cm for the transient and control rods, respectively. Monte carlo calculations predict the regulating and transient rod bank worths for these radii to be $11.0 and $2.8, respectively.

Calculations for the transient rod bank worth based on the above model are summarized in Table 3.9-1. The calculated reactivity worth of the transient bank is approximately 12% lower than the comparable monte carlo results. This difference can be

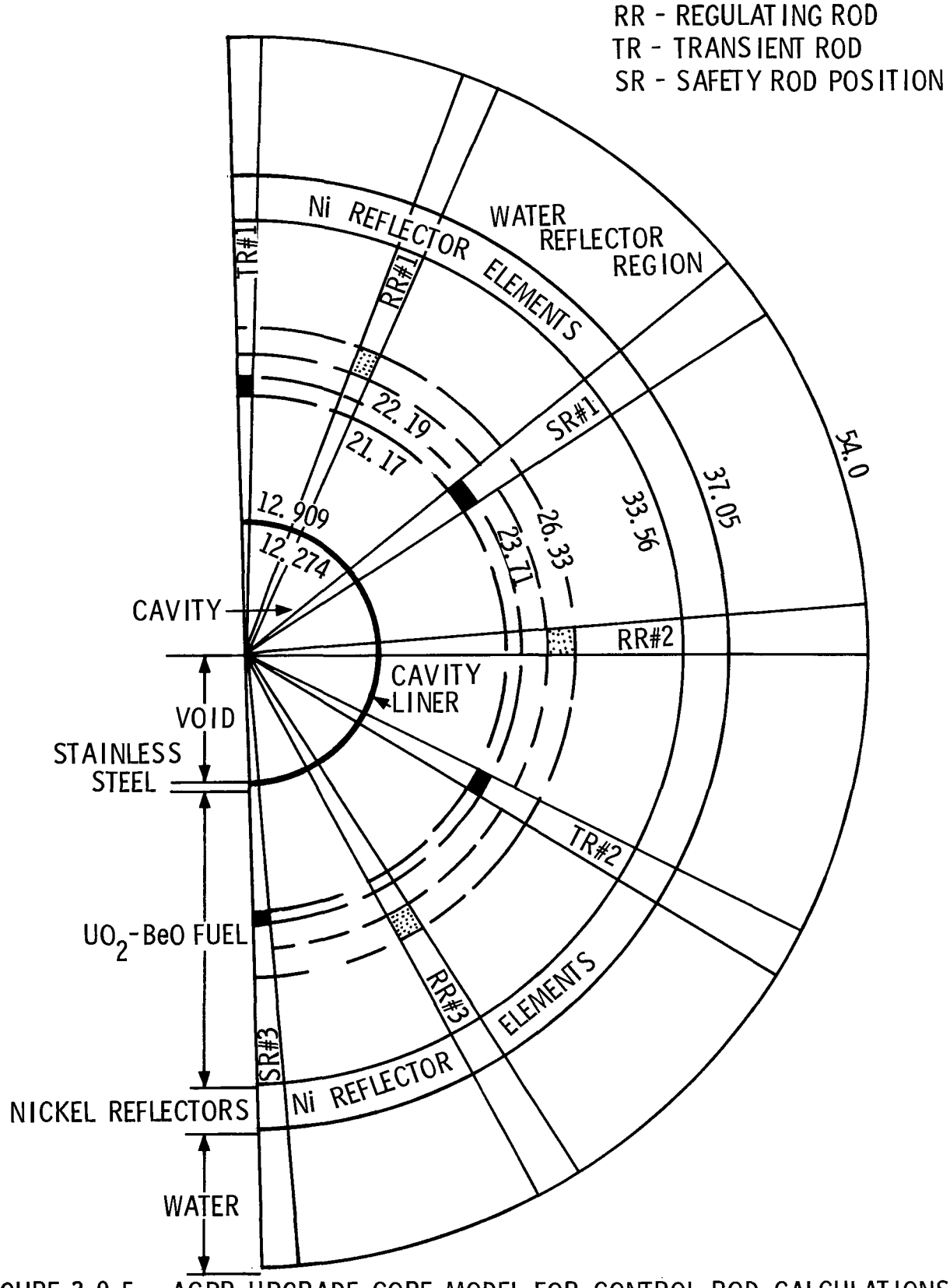

FIGURE 3.9-5. ACPR UPGRADE CORE MODEL FOR CONTROL ROD CALCULATIONS. (R-θ , S_4, P_1, 9 Grp).

attributed primarily to the approximations involved in R-θ geometry and to a lesser extent the coarse mesh quadrature and cross sections used in these survey calculations.

The general trends observed show that the transient rod bank worth increases with increased moderation in the cavity with the regulating rod bank in. The transient rod bank worth decreases with increasing core size and the addition of the Ni reflecting elements tends to increase the transient rod bank worth in comparison with an H_2O reflector region. The magnitude of this effect is not large ($\simeq$ 10%) and the calculated transient rod bank worth in a representative initial water reflected core configuration is calculated to be only about 6% greater than the 200 element Ni reflected core value.

The worth of an individual transient rod when withdrawn sequentially as in a multiple pulse operation, increases about 7% per rod when two rods are withdrawn and about 15% when only one rod is withdrawn. These values apply when the remaining transient rods are left inserted.

The effect of moderating experiments in the cavity on the worth of the transient rod bank was mitigated by preferential loading of outer fuel elements away from the transient rod positions in the original ACPR. This fuel loading scheme reduces the worth of the transient rod bank about 12% and may reduce the transient rod cavity moderator interaction in the ACPR Upgrade if sufficient grid space is available for such a loading scheme to be implemented.

TABLE 3.9-1
NORMALIZED TRANSIENT ROD BANK WORTH CALCULATIONS
(R-Θ, S_4, P_1, 9 Grp)

Core Configuration	Regulating Rod Positions	Transient Rod Bank Worth
Standard Core 200 Elements Ni Reflector	OUT	1.0*
	IN	0.89
Standard Core 1.27 cm Poly in Cavity	IN	1.03
	OUT	0.87
Standard Core 2.54 cm Poly in Cavity	IN	1.08
	OUT	0.90
231 Element Core Ni Reflector	OUT	0.79
129 Element Core Ni Reflector	OUT	1.06
129 Element Core H_2O Reflector	IN	1.12
	OUT	0.95
207 Element Core Ni Reflector (Staggered Fuel Loading)		
0.0 cm Poly	OUT	0.78
1.27 cm Poly	OUT	0.79

*All transient rod bank worth values are relative to the transient bank worth for the standard core with regulating rods in.

TABLE 3.9-1 (cont'd)

Core Configuration	Regulating Rod Positions	Transient Rod Bank Worth
Standard Core		
200 Elements		
Ni Reflector		
0 - TR - IN	IN	1.0**
1 - TR - IN	IN	1.07
2 - TR - IN	IN	1.17
Standard Core		
200 Elements		
Ni Reflector		
0 - TR - IN	OUT	0.89
1 - TR - IN	OUT	0.91
2 - TR - IN	OUT	1.01

**Individual transient rods are relative to one-third of the transient rod bank worth for standard core, regulating rods in.

These standard configuration transient rod worths are $0.93 -- Monte Carlo, $0.87 -- TWOTRAN.

The results of R-Θ calculations for the regulating rod bank are summarized in Table 3.9-2. The reactivity value of the regulating bank (for transient rods out) is $10.19 as compared with $11.00 for the monte carlo analysis. The effect of moderating materials in the cavity tends to increase the bank worth up to about 10% for a 2.54 cm thick polyethylene annulus. The initial core configuration (small core, water reflected) calculation indicates that the regulating bank worth will be reduced about 5% from the 200 element Ni reflected core value.

The effect of core size on the predicted worth of the regulating or transient rod banks is shown in Figure 3.9-6 for the nickel reflected configuration. With the Ni reflector elements in place, the regulating rod bank worth is relatively insensitive to the core size. As core size decreases, the regulating rods represent an increasing volume fraction of the core but also approaches the outer fuel boundary as the core size approaches 132 elements. The two opposing effects combine to produce a shallow maximum in the control bank worth for a nominal 5-row core. Since the magnitude of this effect is small ($\simeq$ 5% or 10¢ per rod), the effect of core size on regulating rod configurations is not anticipated to be a significant factor in core characterization.

Since the transient rod bank is located at a smaller effective radius than the regulating rod bank, the smaller core dimensions do not place the transient rods near the core periphery, and the transient rod bank worth decreases with increasing core size. For a final (nickel reflected) core size ranging from 5 to 6 rows, the magnitude of this effect is +6% and -6%, respectively. Since this

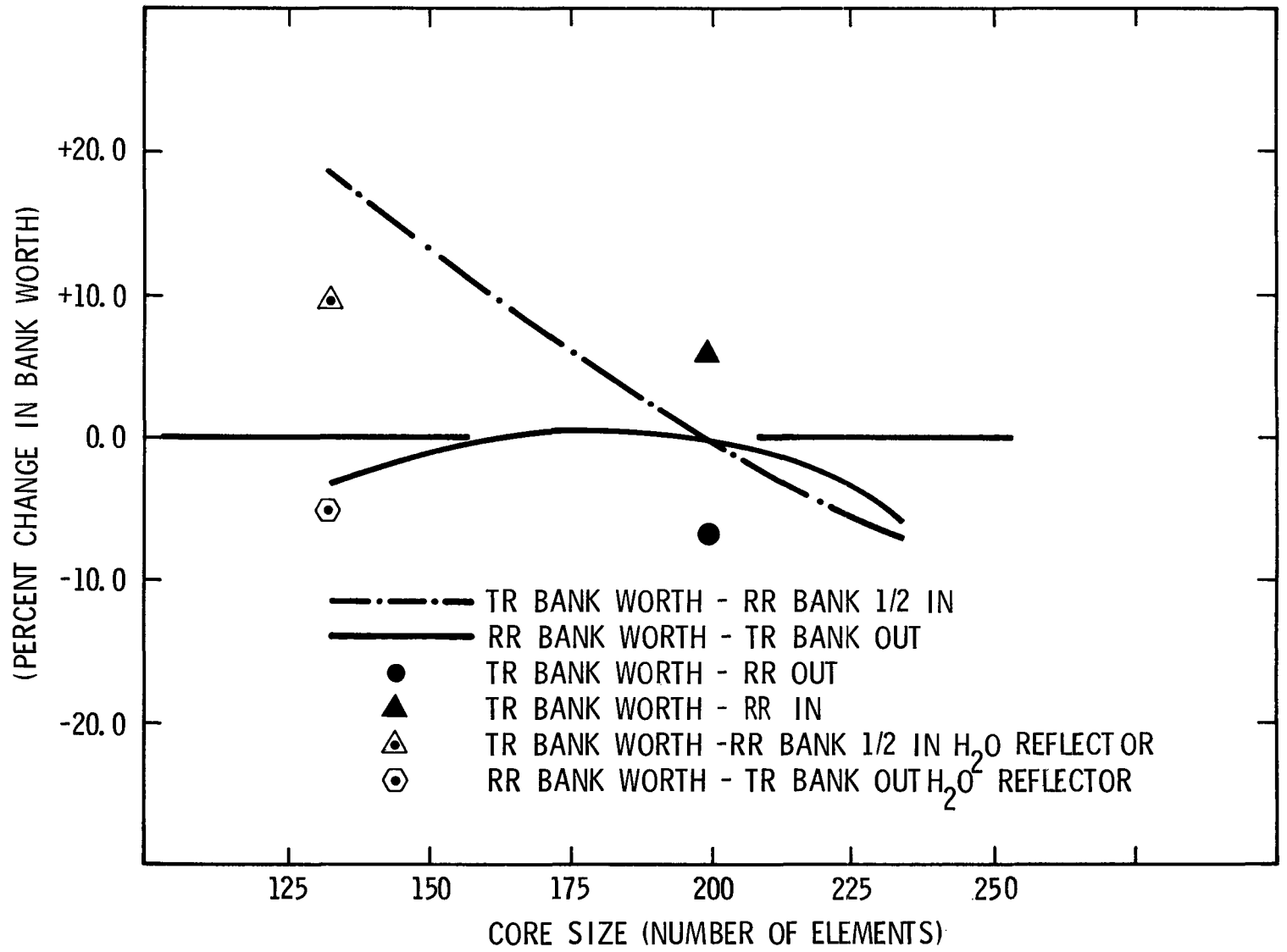

FIGURE 3.9-6. EFFECT OF CORE SIZE AND CONFIGURATION ON PREDICTED WORTH OF TRANSIENT AND REGULATING ROD BANK WORTH.

TABLE 3.9-2

NORMALIZED CALCULATED REGULATING ROD

BANK WORTH CALCULATIONS

(R-θ, S_4, P_1, 9 Grp)

Core Configuration	Transient Rod Position	Regulating Rod Bank Worth
Standard Core 200 Elements Ni Reflector	IN	1.03
	OUT	1.0*
Standard Core 1.27 cm Poly	IN	1.06
	OUT	1.02
Standard Core 2.54 cm Poly	IN	1.15
	OUT	1.10
129 Element Core H_2O Reflector	IN	0.99
	OUT	0.95

*All Regulating Rod Bank Worths are relative to the bank worth for the standard core with transient rods out. ($11.00 Monte Carlo, $10.19 TWOTRAN)

corresponds to a energy yield (and approximate temperature) change of approximately 10%, the core size influence on the transient rod bank worth will have to be accounted for, particularly in the initial, smaller core configurations. Replacing the nickel reflecting elements with water results in a decrease of approximately 9% in the transient rod bank worth.

The use of the R-θ S_N model to examine the sensitivity of control rods to core configuration is a significant approximation in some cases. In general, the qualitative trends of rod worth agree with the monte carlo analysis where comparative calculations were available. The S_N calculations are intended to serve only as a guide in initial characterization of the control rods and the interaction of control rod bank worths and core configuration.

3.10 Reflector Elements

The ACPR Upgrade core utilizes nickel reflector elements surrounding the outer fuel to reduce fission density peaking at the outer fuel surface and reduce the neutron generation time. The effect of changing the reflector material on the outer surface peaking is shown in Figure 3.10-1. The Ni elements effectively eliminate local peaking effects at the outer fuel surface. Allowing water to occupy the space adjacent the outer fuel row results in a large peaking effect of about 20% higher than the inner fuel surface. Other reflector materials examined, such as Al, C, and Zr reduced peaking to a lesser degree than did Ni. Stainless steel reflector elements are similar to Ni elements.

The use of more absorbent, higher mass number reflector materials entails a reactivity and performance penalty, but also results in a significant reduction in neutron generation time and improved kinetics. The effect on neutron generation time of several reflector element materials is summarized in Table 3.10-1.

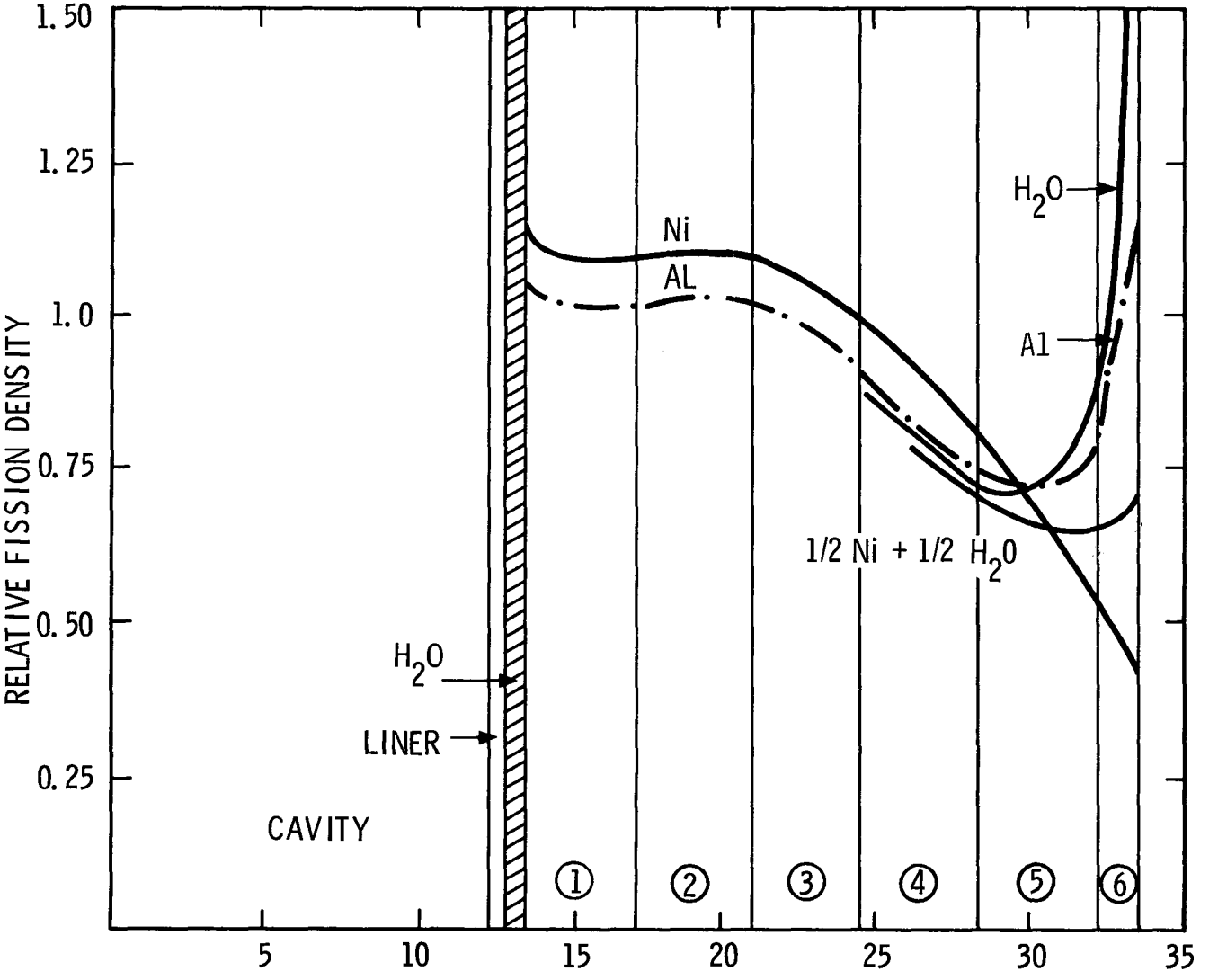

FIGURE 3.10-1. EFFECT OF REFLECTOR ELEMENT MATERIALS ON LOCALIZED FISSION DENSITY PEAKING EFFECTS AT THE OUTER FUEL SURFACE. (S_4, P_1, 9 Grp).

TABLE 3.10-1

NEUTRON GENERATION TIMES FOR VARIOUS REFLECTOR MATERIALS

(KENO-II, 9 Grp, R-Z)

Reflector Element Material	Neutron Generation Time (± 2%)
Ni	24.0
SS	24.5
1/2 Ni, 1/2 H O	24.8
Al	37.7
H_2O	35.4
Graphite	37.0

4. ACPR UPGRADE KINETICS

The dynamic characteristics of the ACPR Upgrade were of primary importance and concern in the reactor physics design studies. The goal of the Upgrade design effort was to produce a core design with maximum performance improvement while retaining the short pulse width capability of the original ACPR. The calculations summarized in this section represent estimates of kinetic performance based on the temperature coefficients obtained from existing cross-section data. Since the prompt fuel temperature coefficients calculated from different cross-section data sets result in values differing by 20%, kinetic behavior was calculated using a range of values for the overall temperature coefficient. The majority of survey calculations, however, was performed using the lowest values obtained from the temperature-dependent calculations.

The calculations performed in support of the ACPR Upgrade Safety Analysis Report[11] utilized a minimum temperature coefficient based on fuel temperature effects only. The survey calculations included in this report used estimates of fuel temperature coefficients from Section 3.6 (BeO-1, and BeO-2), a total feedback coefficient which was defined from the BeO-2 data set, and an approximate estimate of prompt coolant/moderator temperature effects ($\alpha_T = \alpha_{Fuel} + \alpha_{Coolant}$).

4.1 Analytic Methods

Two different computational approaches were used in the analysis of ACPR Upgrade kinetics. The primary analytic tools used were the Sandia reactor kinetics codes SAK and PK1D. SAK is a one-dimensional space-time diffusion code coupled with a one-dimensional general heat transfer model. The space-time dependent multigroup diffusion calculation yields a power generation rate in each core region which is used as input to a unique heat transfer model for that region. The temperature in the fuel element is then calculated, and the average region temperature is then used in a cross section vs. temperature interpolation table to obtain new temperature-dependent cross sections for the next diffusion calculation time step. The flexibility of the SAK calculation is essential for the multi-region core concepts originally under consideration for the ACPR Upgrade. For the single region core design selected for the Upgrade, it was found that adequate results could be obtained from a straightforward point kinetics analysis coupled with one-dimensional heat transfer. Temperature coefficients required for the point kinetics were obtained from temperature dependent SAK runs, or from two-dimensional S_N calculations using uniform temperature cross sections throughout the fueled regions. In general these two approaches gave similar results with the diffusion results indicating a somewhat larger ($\simeq 5\%$) temperature coefficient than the transport results. Temperature-dependent cross-section sets for these analyses were obtained from AMPX cell calculations. Doppler broadening effects were included for both ^{235}U and ^{238}U.

Clad and niobium liner temperature effects and axial fuel expansion effects were not included. Neutron generation times were obtained from the monte carlo criticality code KENO-II for the variety of core configurations considered. The point kinetics code used in these calculations was PK1D. The calculational sequence of PK1D is similar to that described for SAK with the exception that power density distributions are assigned based on dimensional transport calculations, and temperature-induced reactivity effects are obtained from a predetermined temperature coefficient rather than a time-dependent neutronics calculation. Although the majority of kinetics calculations were performed with PK1D for the single region core, comparative SAK results were obtained for most types of transients considered.

4.2 Effective Delayed Neutron Fraction

The effective delayed neutron fraction β_{eff} was calculated with 2D - S_N using the relation,

$$k_p(1 + \beta_{eff}) = k_d(1 + \beta_o) \qquad \beta_o = 0.0065$$

where k_p and k_d are the eigenvalues obtained from the prompt fission and prompt fission + delayed neutron source spectrum, respectively. The result using 9-group cross sections was a value of $\beta_{eff} = 0.0072 \pm 0.0002$. Calculations based on a finer group structure cross section set, indicated a slightly higher value, of 0.0073 ± 0.0003. Other kinetics parameters used in the analysis are summarized in Table 4.4-1.

4.3 Heat Transfer Model

The ACPR Upgrade core design consists of nominally 200 fuel elements. The one-dimensional heat transfer model associated with the ACPR Upgrade fuel element design is shown in Figure 4.3-1. Representative thermal conductivities and specific heats used for the element materials are given in Table 4.3-1. The calculation provides radiation heat transport across the fuel liner gap and liner-clad gap. The coolant heat transfer at the outer clad surface was described by the function,

$$h(T) = 0.04 + 9.2\ (10^{-5}) \left(T_{surf} - T_{bulk}\right)^2 \left(\frac{watts}{cm^2\ ^\circ C}\right)$$

This function accounts approximately for the initial conduction heat transfer, followed by natural convection and incipient boiling heat transfer encountered at higher heat fluxes. Since the pulse is essentially adiabatic, the heat transfer model described here is primarily important for describing thermal conditions after the pulse or in slow transient operations, and in defining fuel temperature profiles for thermal stress calculations.

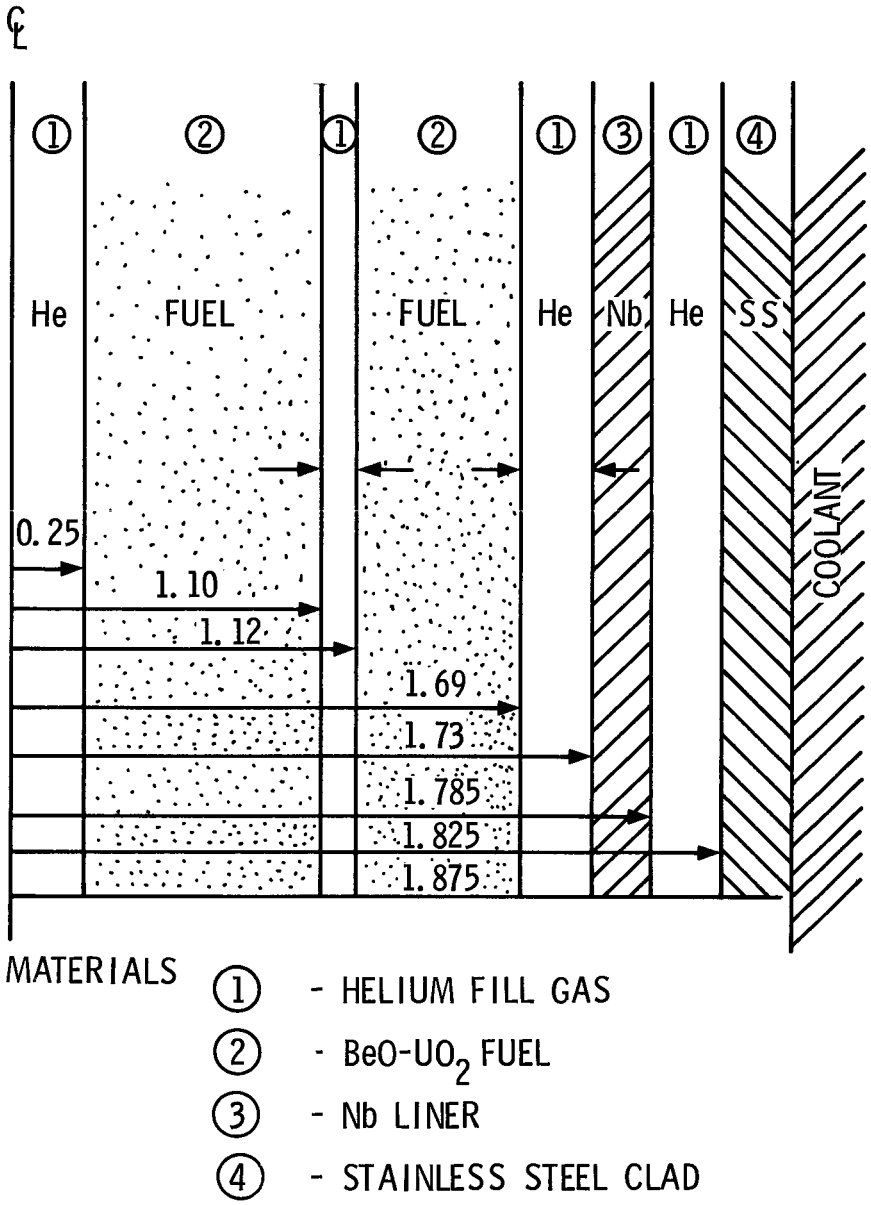

FIGURE 4.3-1. SCHEMATIC ONE DIMENSIONAL HEAT TRANSFER MODEL FOR UO_2- BeO FUEL ELEMENT DESIGN.

TABLE 4.3-1

TEMPERATURE-DEPENDENT THERMAL PROPERTIES FOR UO_2-BeO FUEL ELEMENT HEAT TRANSFER MODEL

	k (watt/cm °C)				C_p (J/cm^3 °C)			
Temp. (°C)	He	Nb	SS	BeO-UO_2	He	Nb	SS	BeO - UO_2
0	$1.44(10^{-3})$	0.05	0.37	2.70	0.00092	2.30	4.01	2.75
300	$2.32(10^{-3})$	0.056	0.37	0.95	0.00092	2.39	4.30	4.48
600	$3.20(10^{-3})$	0.062	0.37	0.52	0.00092	2.51	4.60	4.82
900	$4.08(10^{-3})$	0.068	0.37	0.34	0.00092	2.64	4.89	5.17
1200	$4.96(10^{-3})$	0.074	0.37	0.24	0.00092	2.80	5.18	5.51

4.4 Pulse Characteristics

The general characteristics of the ACPR Upgrade transient behavior were examined with both SAK and PK1D models. The one-dimensional SAK model is based on the two-dimensional transport model of Figure 3.1-1. The reactor parameters used in the point kinetics model are summarized in Table 4.4-1.

The quantities of interest in the ACPR Upgrade transient behavior are the neutron fluences, fuel temperatures, pulse widths, peak power and pulse vs. tail energy as a function of system yield, minimum period, or reactivity insertion. These quantities were evaluated primarily with the point kinetics model with detailed pulse shape comparisons from the one-dimensional space-time analysis. The survey calculations shown in this section used one of the following expressions for the prompt negative temperature coefficient:

1. $\alpha_{F1}(T) = -0.50 + 0.00017\ \Delta T\ (¢/°C)$,

2. $\alpha_{F2}(T) + -0.43 + 0.00012\ \Delta T\ (¢/°C)$,

3. $\alpha_{Tot}(T) = \alpha_{F2}(T) + \alpha_{coolant}(T)$,

   where $\alpha_{coolant}(T) = -0.18(¢/°C)$,

   (See Section 3.6.)

The cross section data utilized in $\alpha_{F2}(T)$ is considered to be the most accurate.

TABLE 4.4-1 REACTOR PARAMETERS USED IN ACPR UPGRADE POINT KINETICS ANALYSIS

Parameter	Computational Model	Value
Effective Delayed Fraction (β_{eff})	TWOTRAN	0.0073
Reactivity Withdrawal Time	--	50 msec
Neutron Generation Time (ℓ)	KENO-II	24 μsec
Prompt Fuel Temperature Coefficient (¢/°C)	SAK--(BeO - 1)	$\alpha_3 = 0.56 + 0.00019\Delta T$
	TWOTRAN--(BeO - 1)	$\alpha_1 = 0.50 + 0.00017\Delta T$
	TWOTRAN--(BeO - 2)	$\alpha_2 = 0.43 + 0.00012\Delta T$
Coolant Temperature Coefficient (¢/°C) (Single Pulse)	TWOTRAN	$\alpha = 0.18$
Power Distribution	TWOTRAN	1.23 - Row 1 1.19 - Row 2 1.16 - Row 3 1.02 - Row 4 0.73 - Row 5,6 1.81 - Hot Spot
Average Cell Fission Distribution	XSDRN-PM MORSE	P/A - 1.3
Core Fission Distribution	TWOTRAN	P/A - 2.37
Fuel Volume cc/element	--	435

The coolant temperature coefficient was discussed in Section 3.6 and represents an approximate treatment based on stagnant coolant over the time span of the transient. Figures 4.4-1 through 4.4-6 show a representative pulse for the ACPR Upgrade ($\Delta\rho$ = 0.0146). The poison is withdrawn in 0.050 seconds using a $\sin^2(at)$ time-dependent reactivity function. Figure 4.4-1 shows the power shape during the pulse, and Figure 4.4-2 shows the longer time (14 seconds) power trace. The lower line on Figure 4.4-2 shows the effect of reinserting transient rods at 2 seconds after the pulse. Figure 4.4-3 and 4.4-4 display the yield and average core temperature as a function of time, respectively. For this relatively small pulse ($2.0), the fraction of the total energy yield in the pulse tail is significant if the rods are not reinserted after the pulse. Figure 4.4-5 shows the maximum fuel temperature vs. time curve, and Figure 4.4-6 shows the net system reactivity as a function of time. These calculations utilized the negative temperature coefficient $\alpha_{Tot}(T)$, including both fuel and moderator temperature feedback effects.

A series of kinetics calculations were performed using α_{F1}, α_{F2}, and α_{Tot} temperature coefficients. These calculations assumed that transient rods were not reinserted until 20 seconds after the pulse. Figures 4.4-7 through 4.4-12 show the relationships between core energy release and reactivity insertion, peak power, maximum and average core temperatures, fluence, and initial pulse tail power, respectively, with the prompt negative temperature coefficients described above.

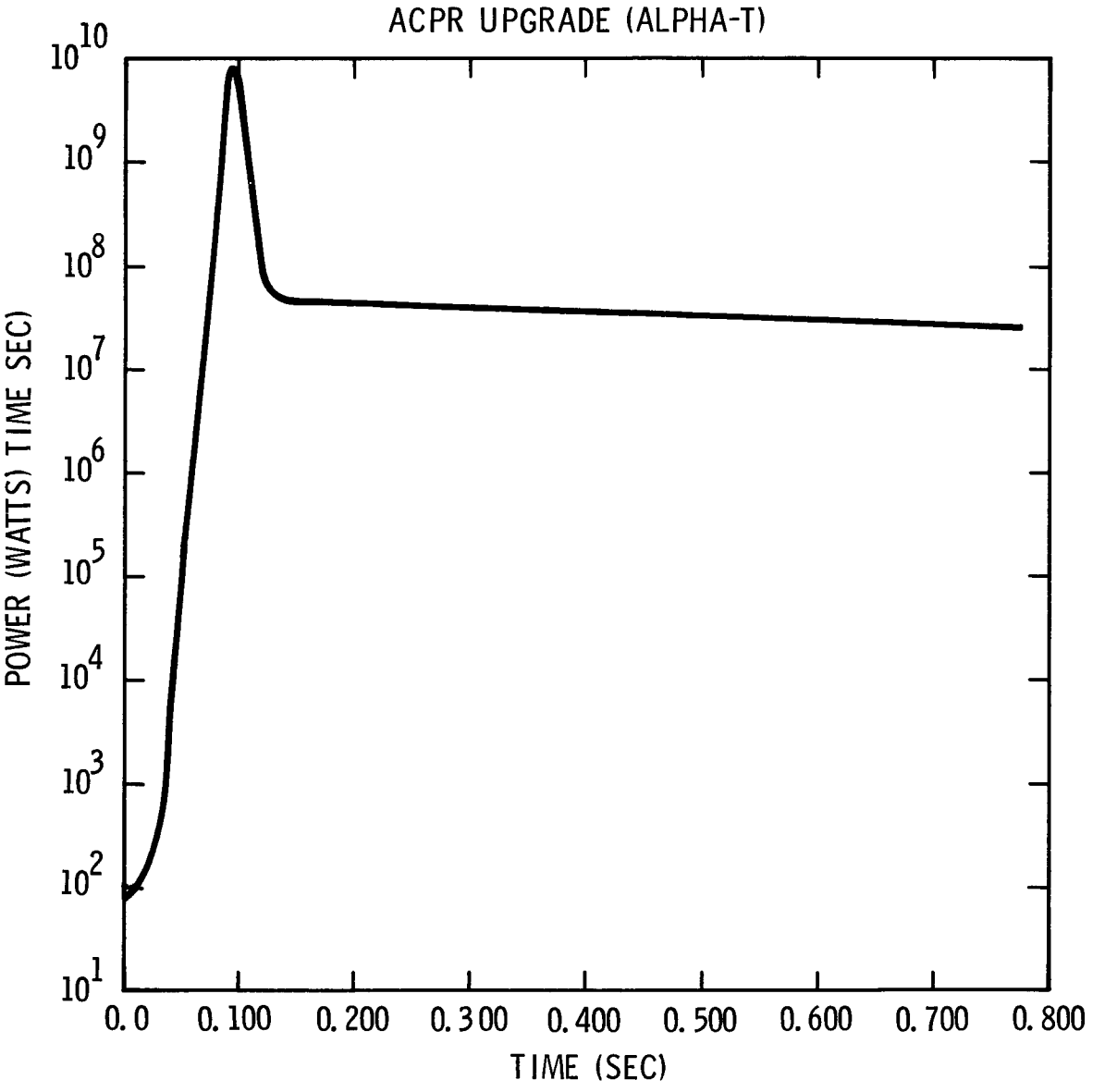

FIGURE 4.4-1. REACTOR POWER TRACE FOR A \$2.0 ACPR UPGRADE PULSE. (PK1D, α_{Tot}).

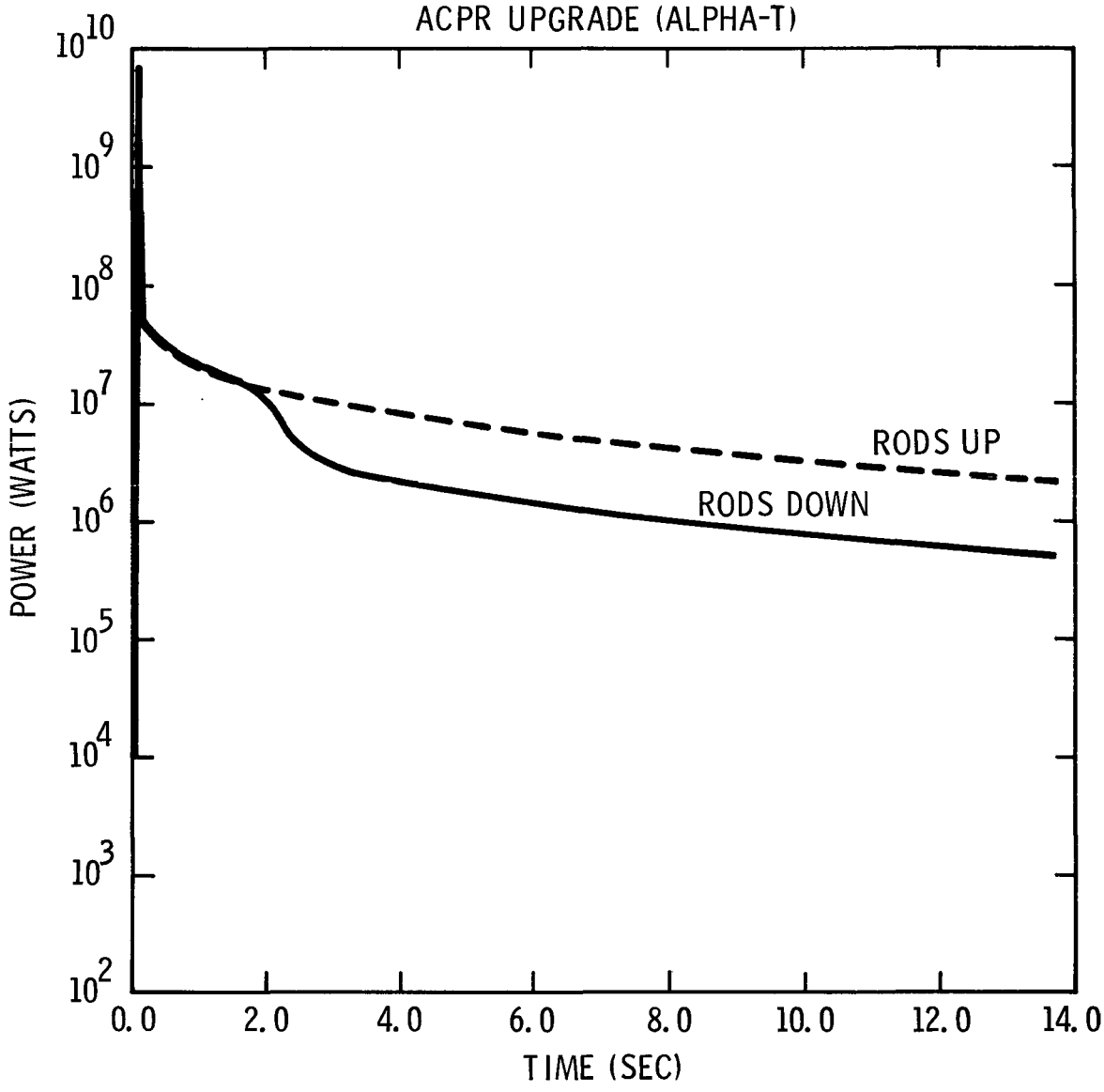

FIGURE 4.4-2. REACTOR POWER TRACE FOR A \$2.0 ACPR UPGRADE PULSE FOR TRANSIENT RODS HELD OUT AND REINSERTED AT 1.5 SECONDS (PK1D, α_{TOT}).

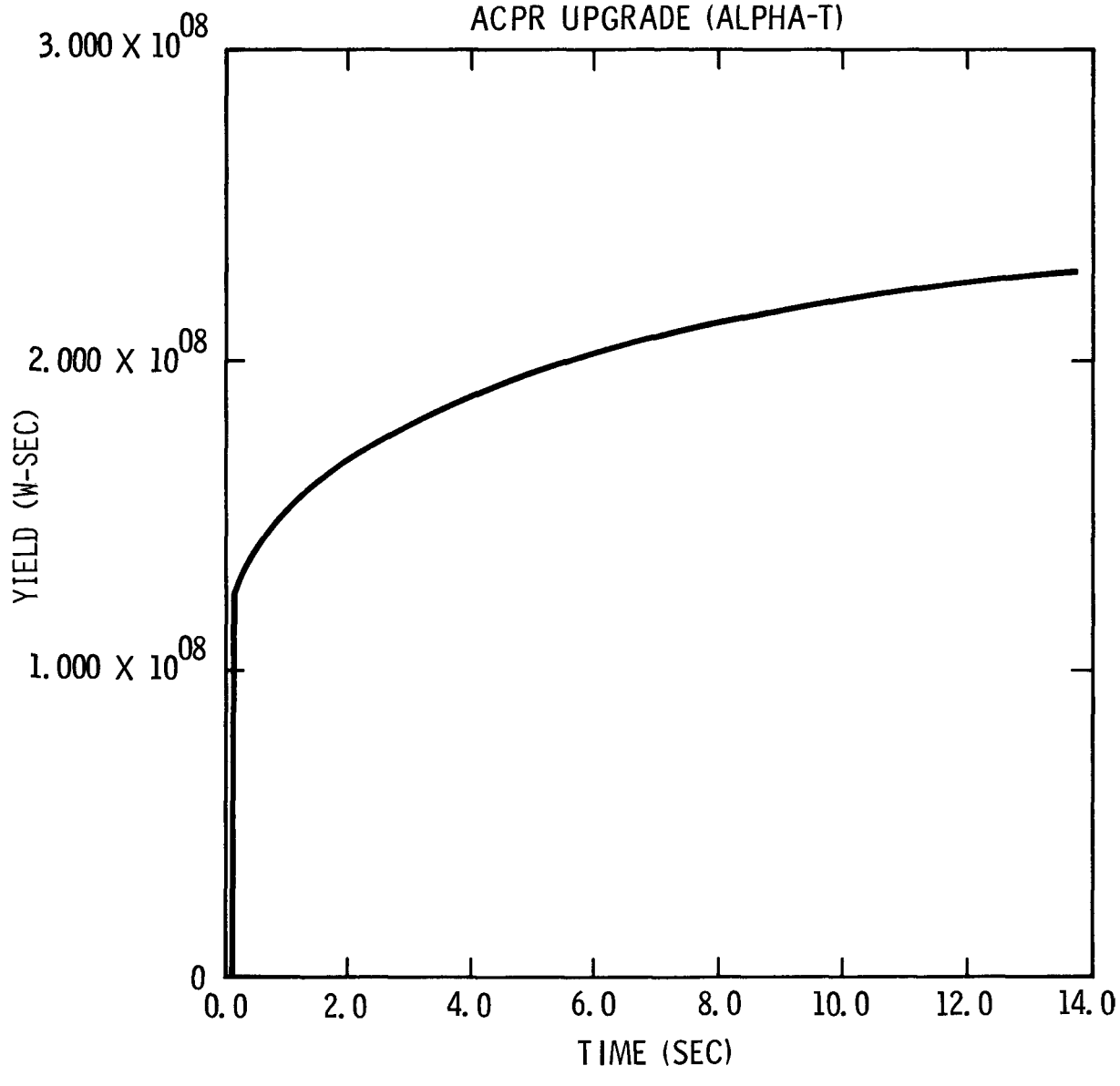

FIGURE 4.4-3. TOTAL REACTOR ENERGY YIELD FOLLOWING A $2.0 ACPR UPGRADE PULSE. (PK1D, α_{TOT})

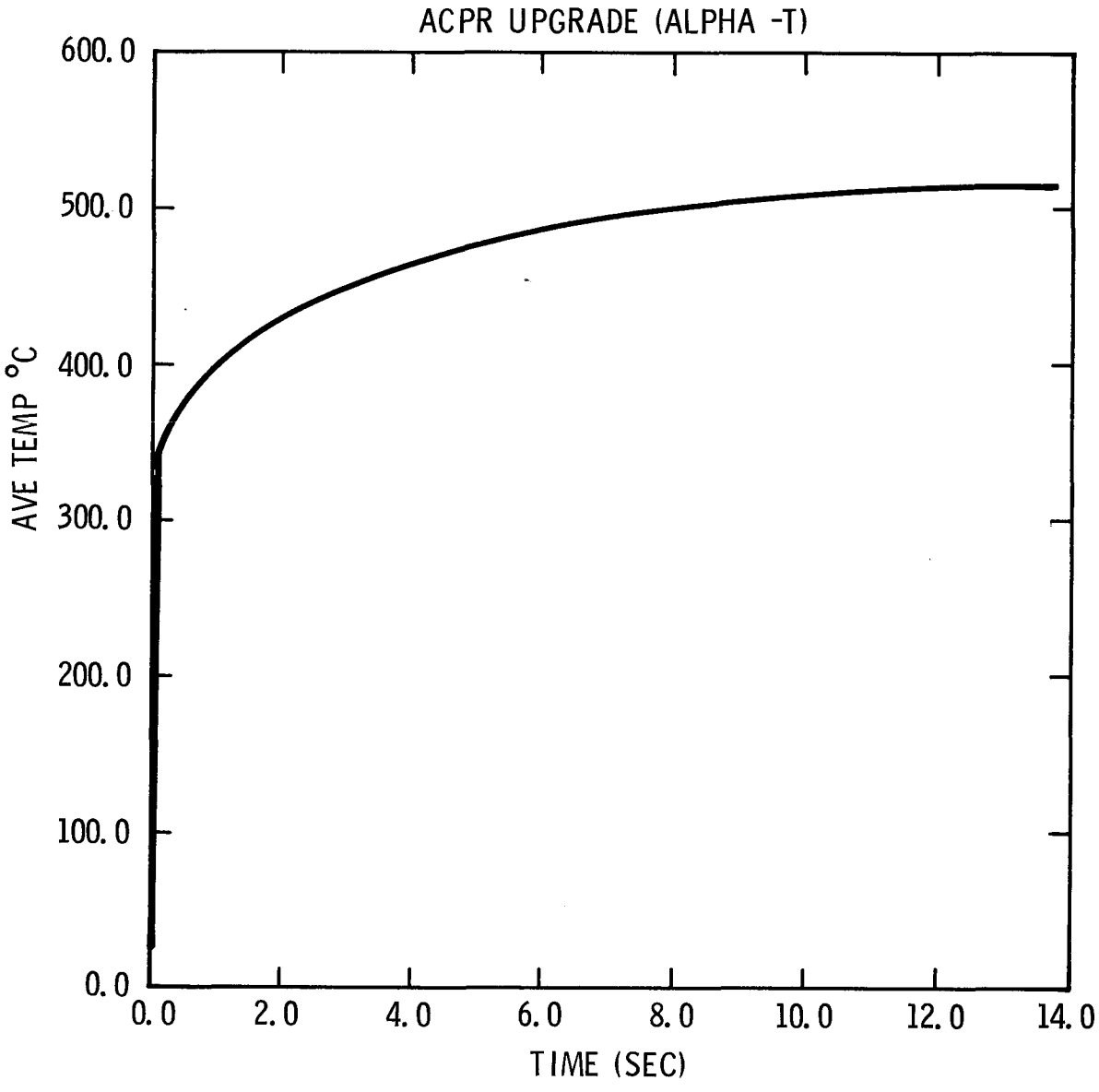

FIGURE 4.4-4. AVERAGE CORE TEMPERATURE FOLLOWING A $2.0 ACPR UPGRADE PULSE (PK1D - α_{TOT}).

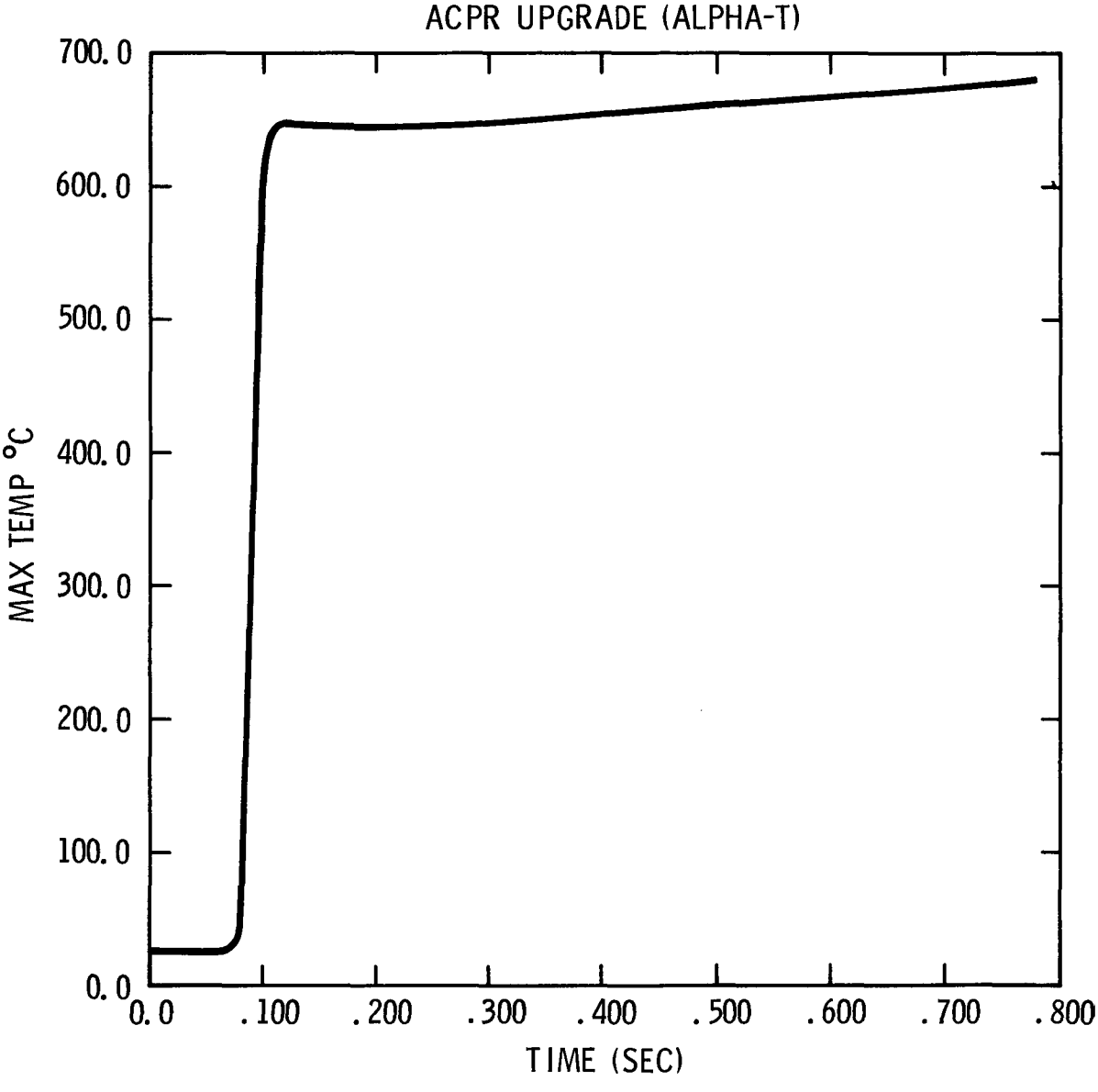

FIGURE 4.4-5. MAXIMUM FUEL TEMPERATURE CALCULATED FOR A $2.0 PULSE FOR ACPR UPGRADE (PK1D - α_{TOT}).

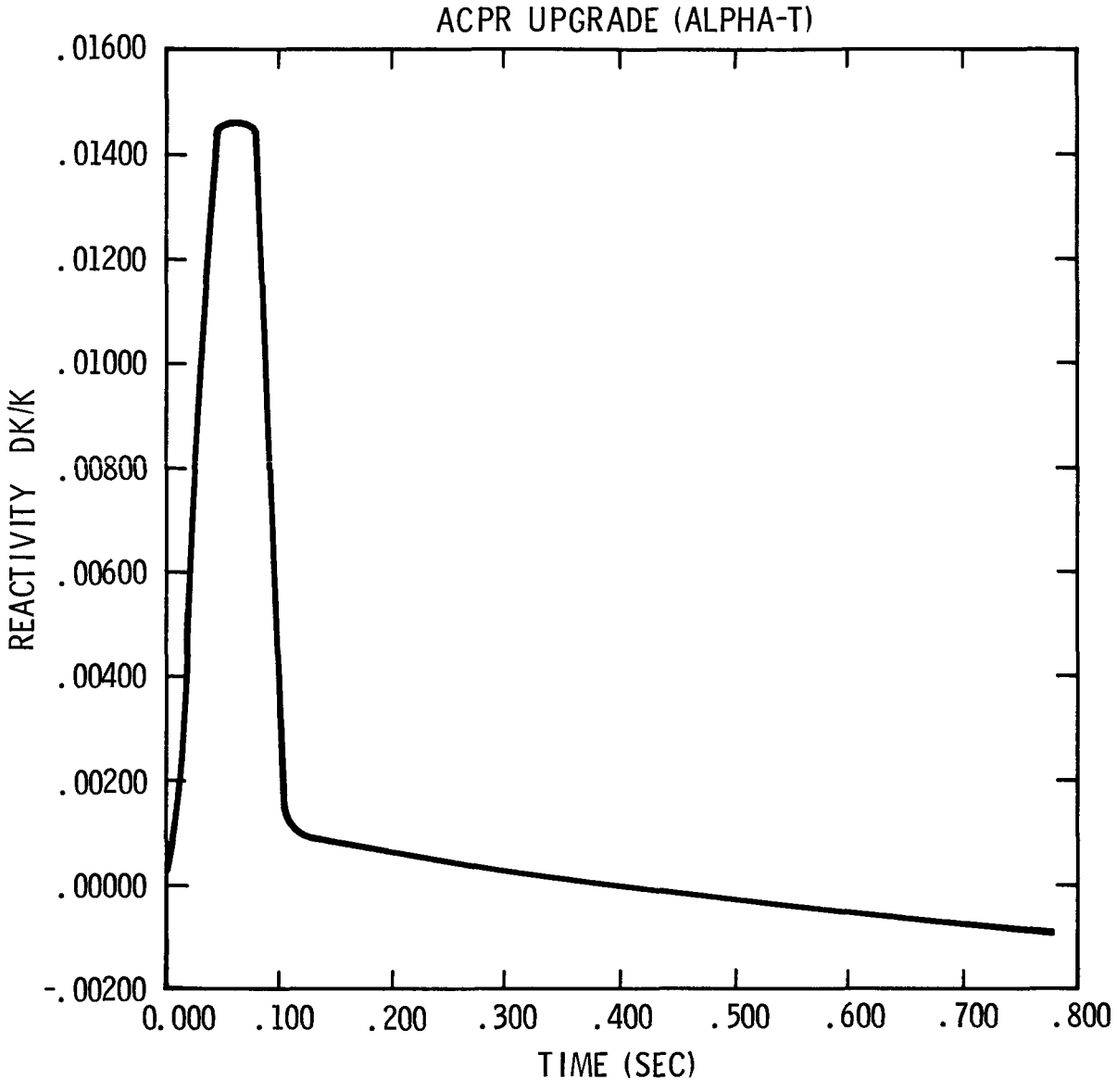

FIGURE 4.4-6. TOTAL SYSTEM REACTIVITY AS A FUNCTION OF TIME FOLLOWING A \$2.0 ACPR UPGRADE PULSE. (PK1D - α_{Tot}).

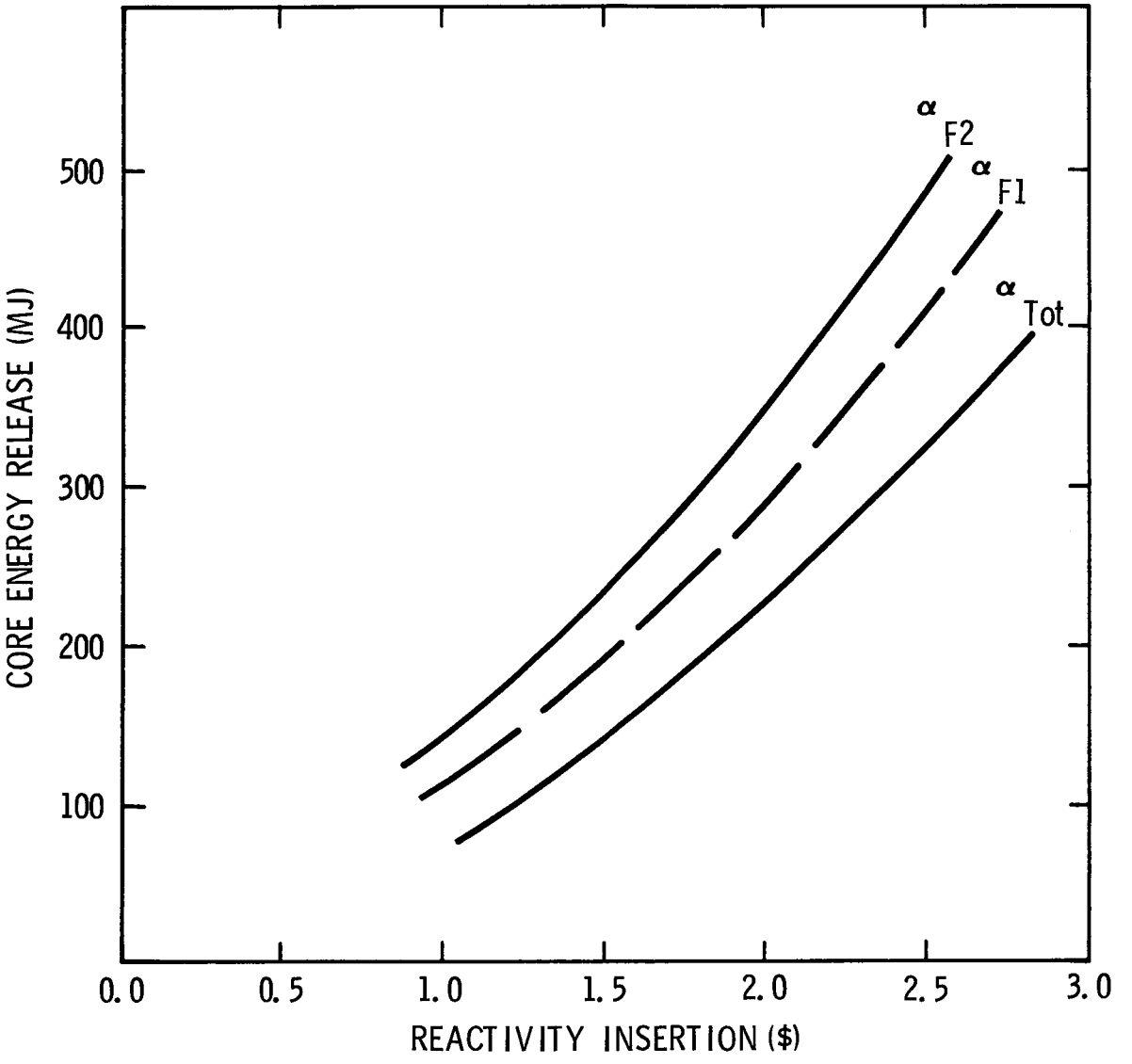

FIGURE 4.4-7. CORE ENERGY RELEASE vs. REACTIVITY INSERTION FOR $\alpha_{F1\ \&\ F2}$ AND α_{TOT} TEMPERATURE COEFFICIENTS. (ENERGY, RELEASE VALUES CALCULATED FOR RODS HELD OUT FOR 20 SEC AFTER PULSE INITIATION).

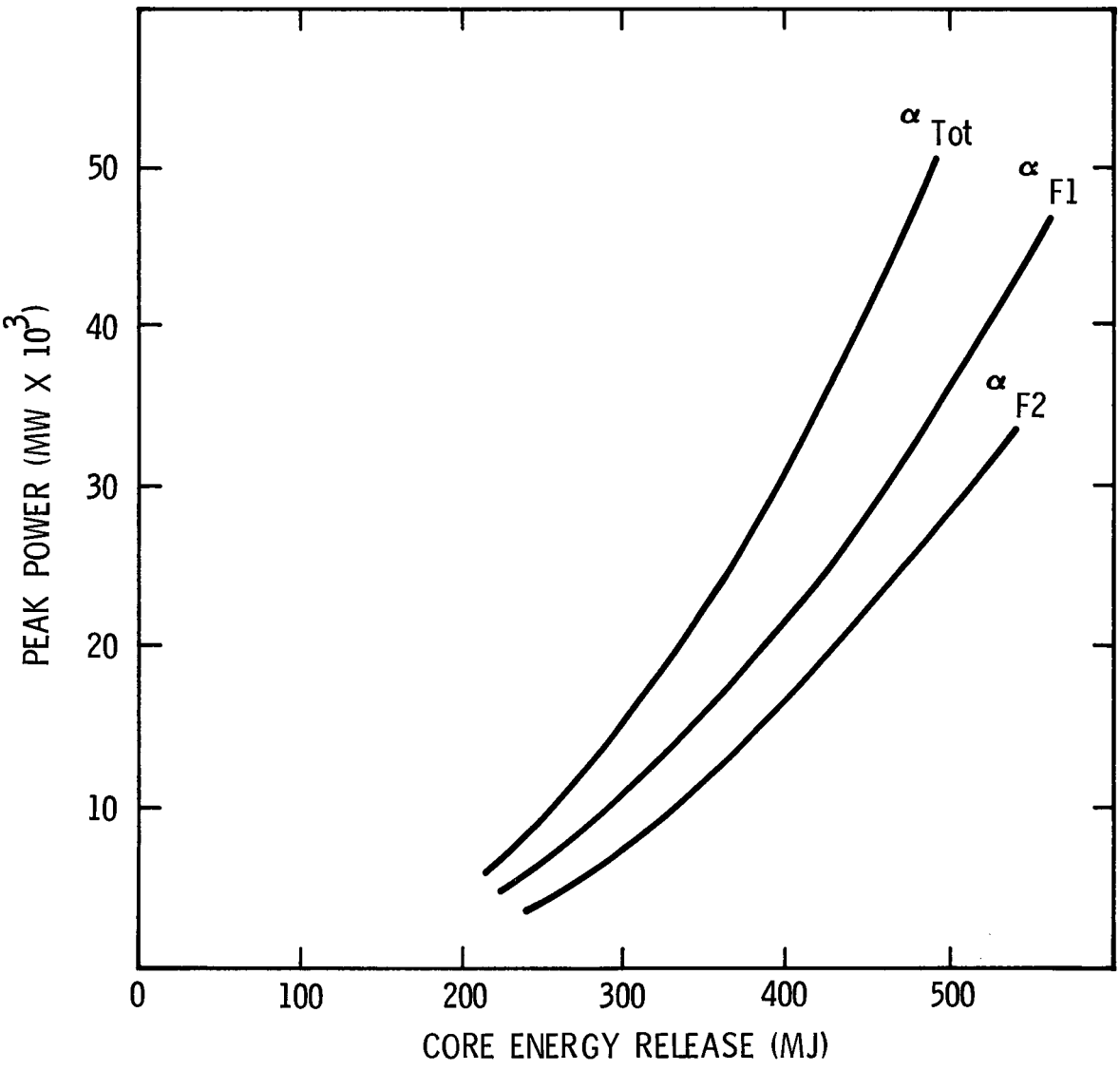

FIGURE 4.4-8. PEAK POWER OCCURRING IN PULSE vs. ENERGY RELEASE RODS HELD OUT FOR 20 SEC.)

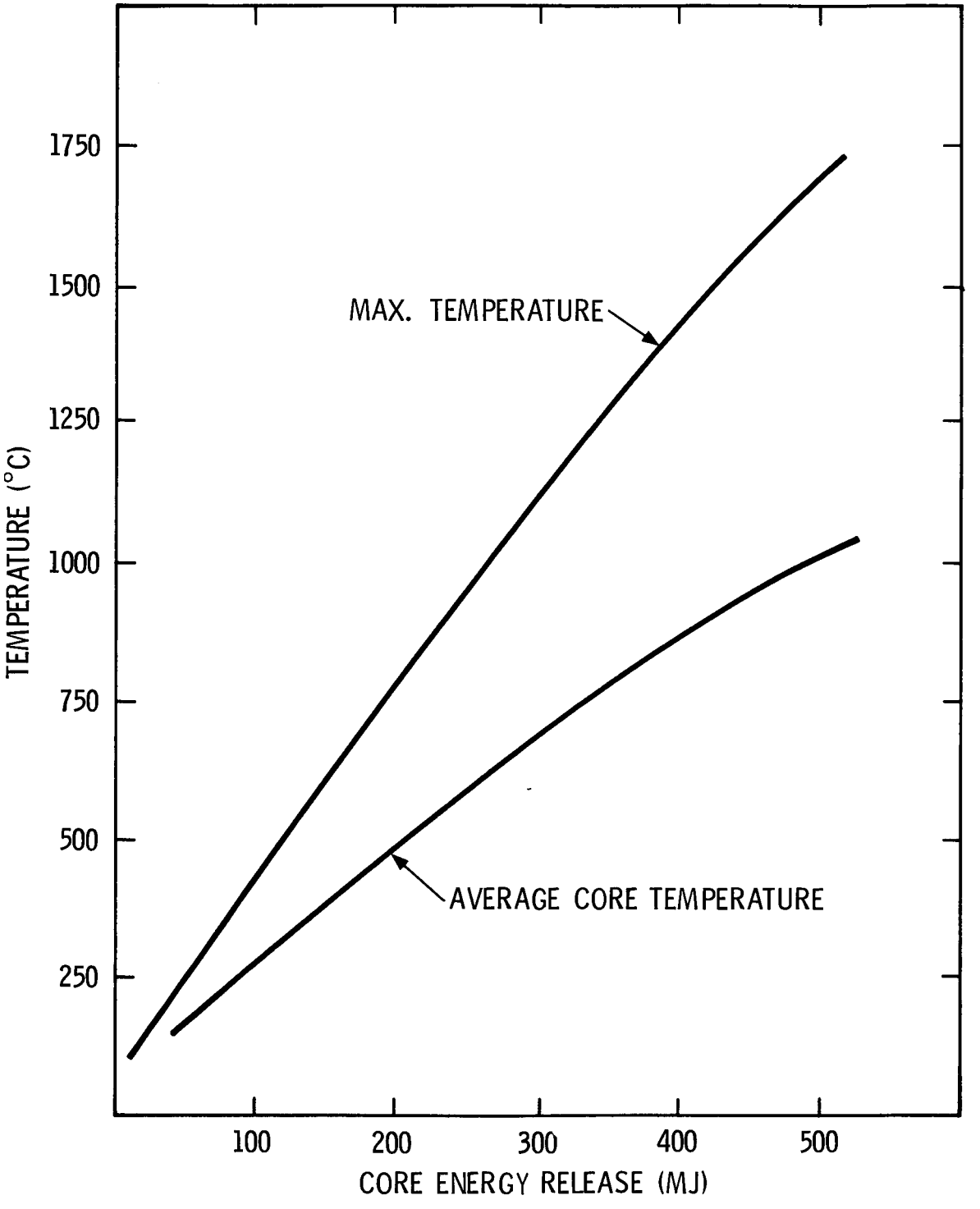

FIGURE 4.4-9. MAXIMUM FUEL TEMPERATURE OCCURRING IN PULSE vs. CORE ENERGY RELEASE (RODS HELD OUT OR RODS REINSERTED) (CORE PEAK/AVERAGE = 1.8).

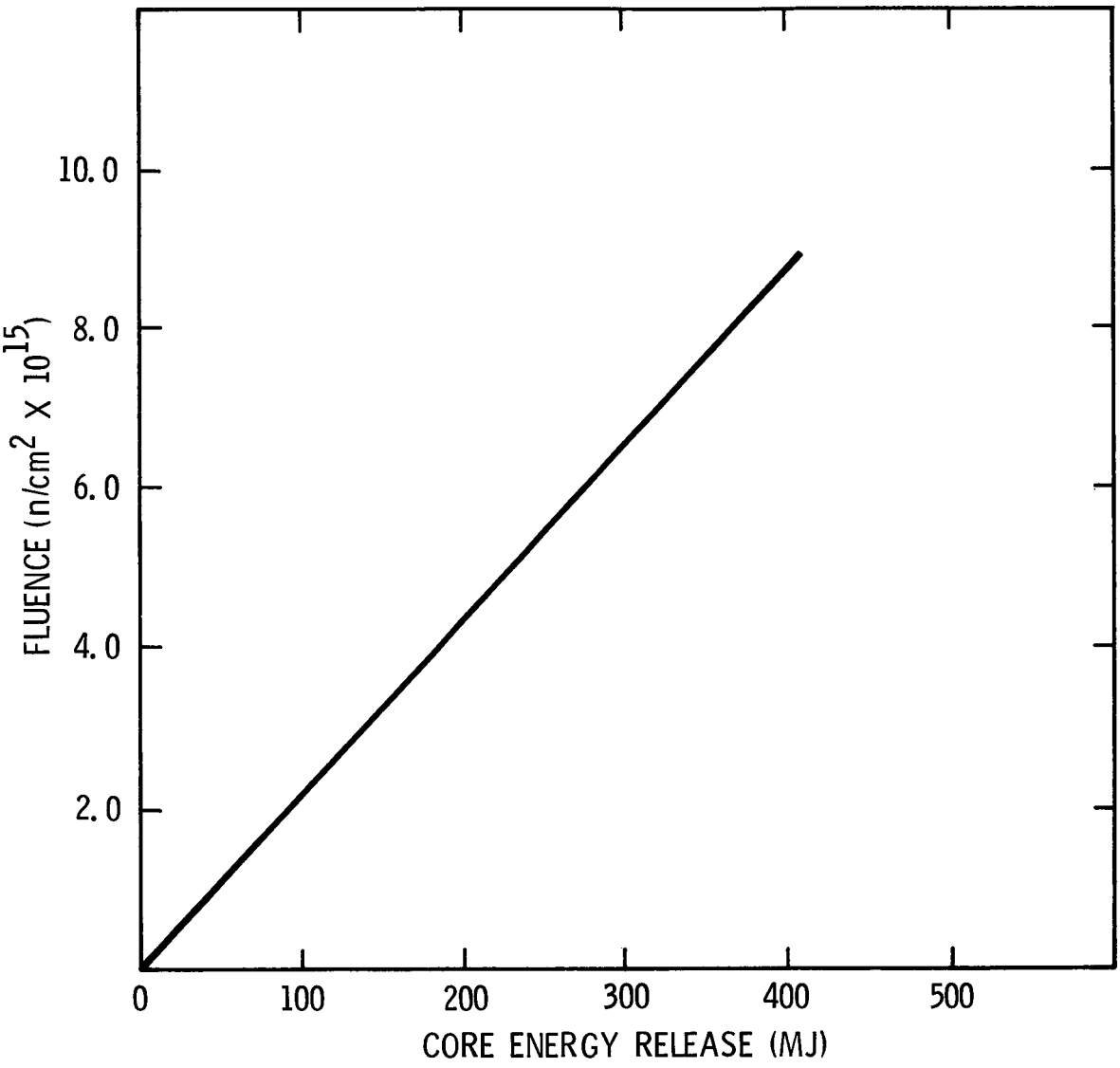

FIGURE 4.4-10. TOTAL PULSE FLUENCE vs. ENERGY RELEASE. (NORMALIZED TO S_8 -- TWØTRAN RESULTS -- TABLE 3.5-1).

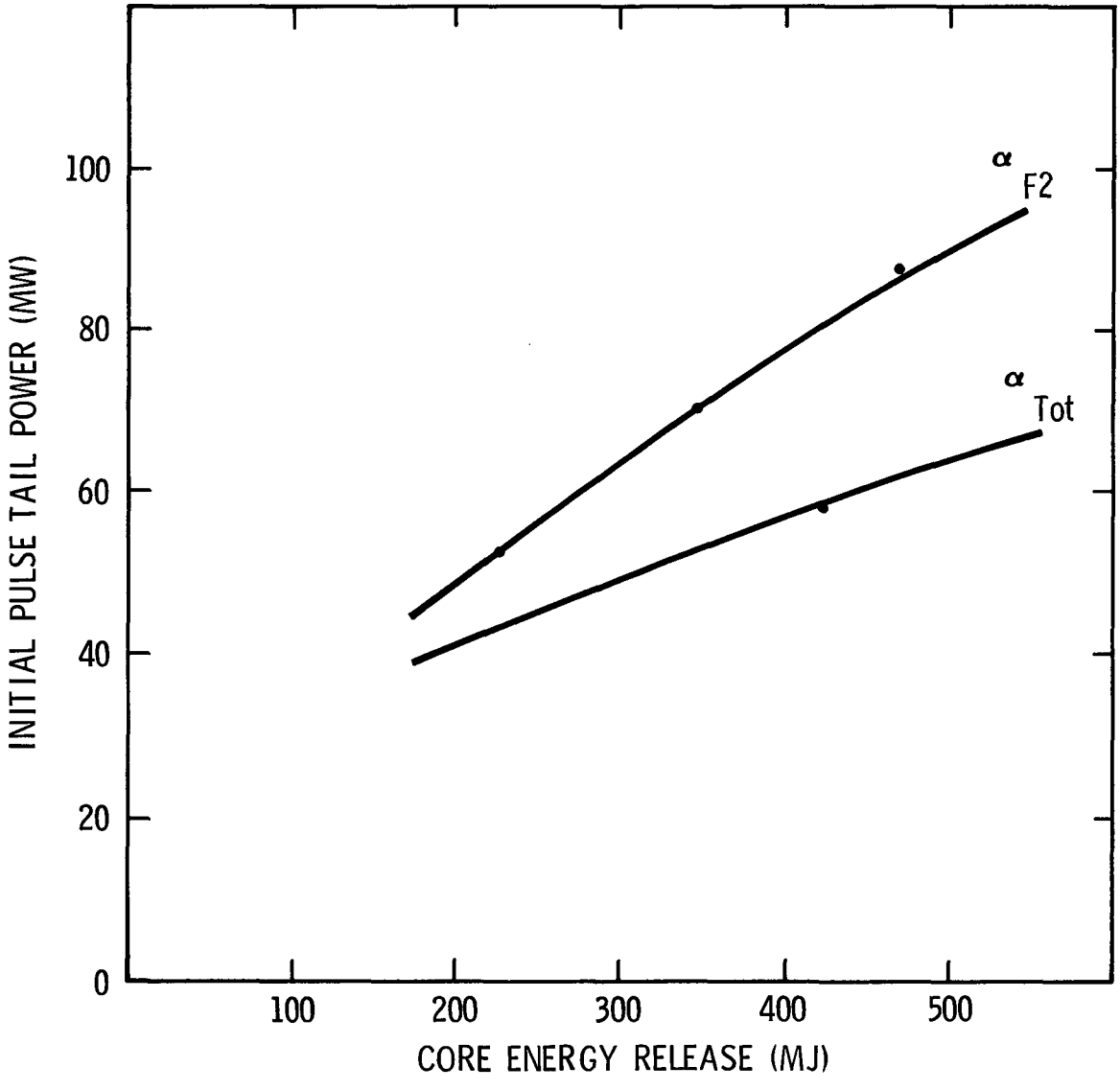

FIGURE 4.4-11. INITIAL POWER LEVEL IN PULSE TAIL vs. CORE ENERGY RELEASE (RODS HELD OUT FOR 20 SEC).

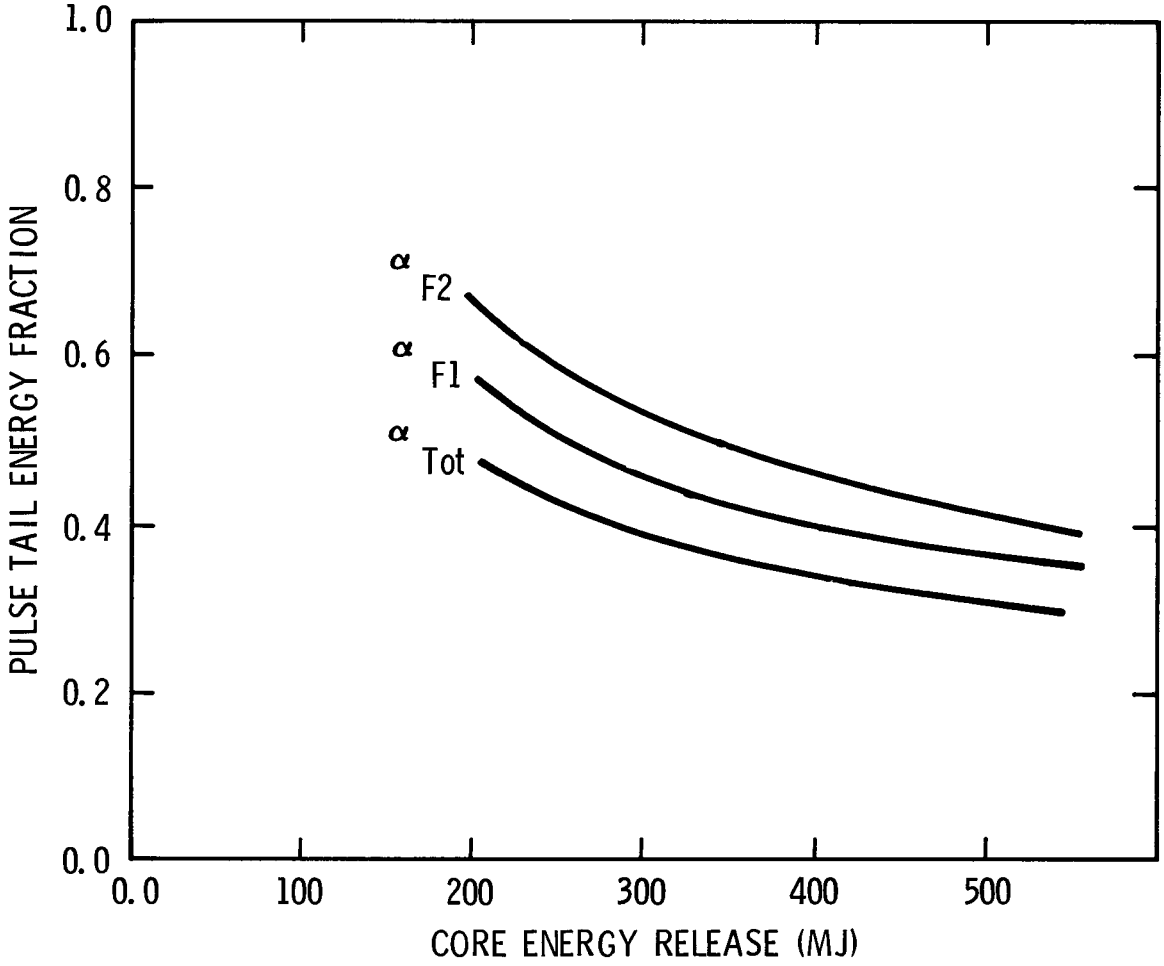

FIGURE 4.4-12. FRACTION OF ENERGY IN PULSE TAIL vs. TOTAL CORE ENERGY RELEASE. (RODS HELD UP 20 SEC)

4.5 Pulse Tail Characteristics

For transient operations that attempt to produce near adiabatic heating effects, it is desirable to minimize the fraction of the reactor yield occurring in the tail. Although the inherent nuclear characteristics of the BeO based fuel will result in higher tail energy fractions than occurred in the hydride fueled ACPR, the effects of this increased tail energy fraction can be mitigated with control or transient rod reinsertion shortly after the pulse. The effect of the magnitude of the reactivity reinsertion and the delay time after the pulse have been examined for representative pulses. As can be seen from Figure 4.5-1, the magnitude of the reactivity reinsertion does not strongly affect the tail energy fraction as long as the amount reinserted is comparable to the pulse reactivity. The fraction of energy yield in the pulse tail is dependent on the time delay in reinserting reactivity. This effect is shown in Figure 4.5-2 for 1.0 and 0.1 second reinsertion times. This dependence is stronger for smaller pulses which have inherently greater tail energy fractions.

For the transient rod pneumatic drives used in the ACPR Upgrade, the minimum delay time after the transient rods have seated (full out) that the transient rod bank reinsertion can be initiated is estimated to be approximately 1.5 sec. Approximately one second is required for the transient rod to fall by gravity to the full in position in the core. The relatively long delay time for the transient rod bank is due to the time required to purge the pneumatic drive system and allow the rods to begin to fall.

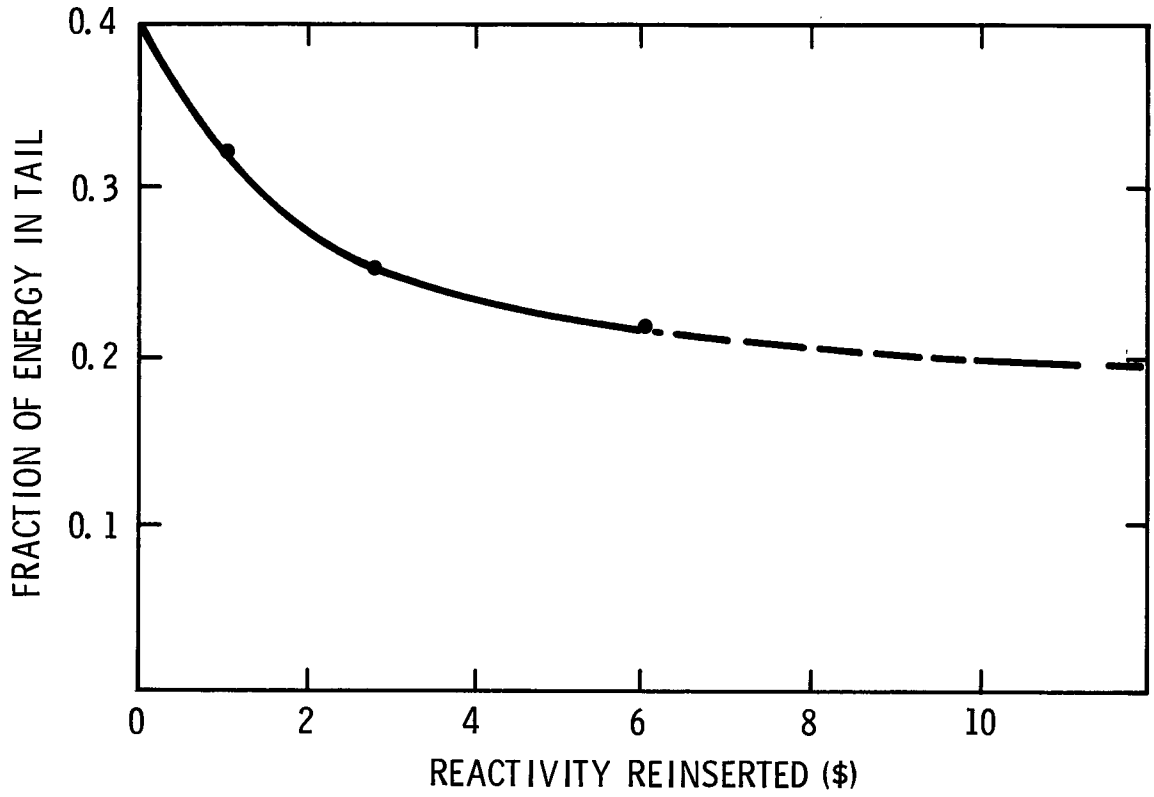

FIGURE 4.5-1. EFFECT OF THE MAGNITUDE OF REACTIVITY REINSERTED IN 1.0 SEC AT A DELAY TIME OF 1.5 SEC, ($2.50 PULSE) IN FRACTION OF ENERGY YIELD IN TAIL. (α_{F1}).

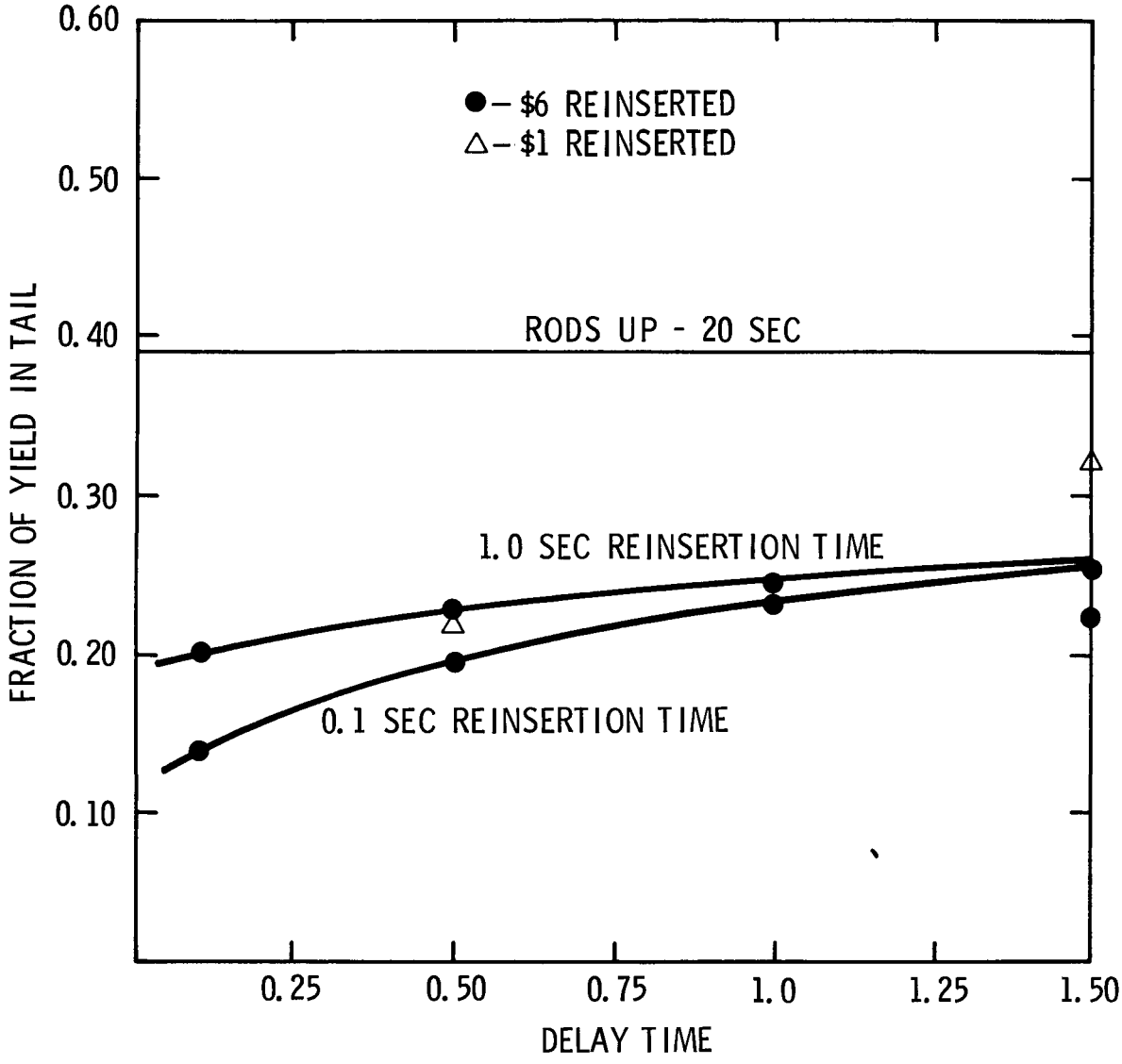

FIGURE 4.5-2. FRACTION OF ENERGY IN TAIL AS A FUNCTION OF DELAY TIME FOR REINSERTING REACTIVITY. ($2.50 PULSE, α_{F1}).

The control and safety banks require a relatively short delay time ($\simeq$ 0.2 sec) before the control magnets release the rods. Approximately one second is required for the rod to fall by gravity into the core. The effect of delay time on total energy yield is shown in Figure 4.5-3. The effects of rod reinsertion on the fraction of total energy release in the pulse tail are less significant when larger values of the temperature coefficient are utilized, resulting in lower total energy fractions in the pulse tail.

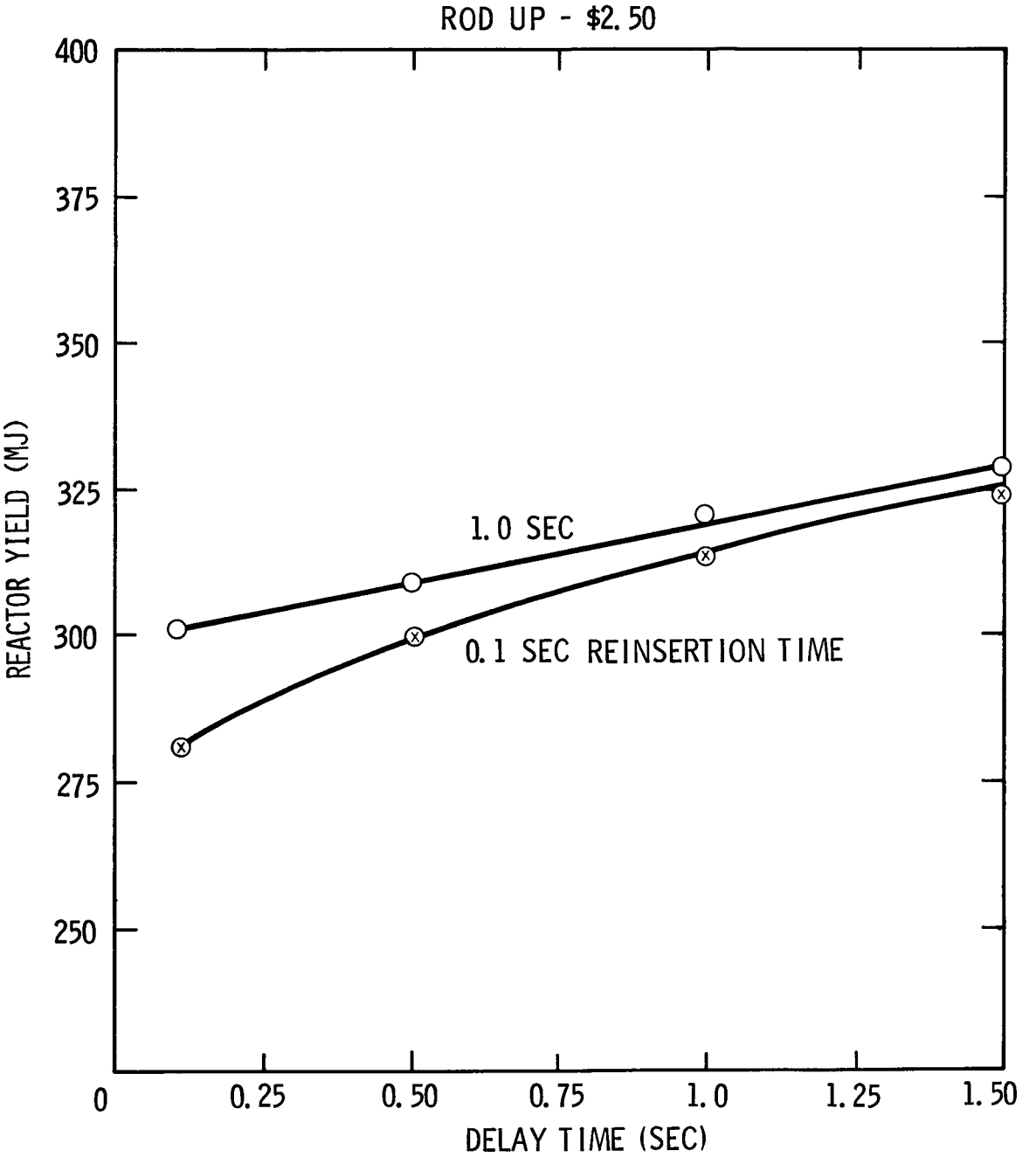

FIGURE 4.5-3. TOTAL REACTOR ENERGY YIELD AS A FUNCTION OF DELAY TIME FOR REACTIVITY REINSERTION ($2.50 PULSE)($\alpha_{F1}$).

4.6 Multiple Pulse Operations

The ACPR Upgrade, like the original ACPR, can be operated in a sequenced pulse mode. Either a double or triple pulse operation can be initiated by a sequenced ejection of the three transient rods. The double pulse can be performed with a single rod pulse followed by a two rod pulse (or a fraction of a two rod pulse) to simulate a preheat and prompt burst condition in reactor safety tests. The total reactor yield for a given reactivity insertion is reduced in comparison with a comparable single pulse by about 5 to 10% for a typical double pulse operation such as is illustrated in Figures 4.6-1 through 4.6-3. Peak temperatures are slightly reduced due to the extended period of time available for thermal relaxation.

A similar calculation is shown in Figures 4.6-4 through 4.6-6 for a triple pulse operation. The reduction in the yield for this triple pulse is about 15%. The triple pulse mode is limited in the Upgrade to a relatively small third pulse due to the limited reactivity available in a single transient rod. In addition, these illustrative calculations utilized a temperature coefficient based on fuel temperature alone, and actual yields in these modes will be further reduced when coolant temperature effects are accounted for. Many reactor operations which utilize a triple pulse can also be simulated by a transient rod runout operation.

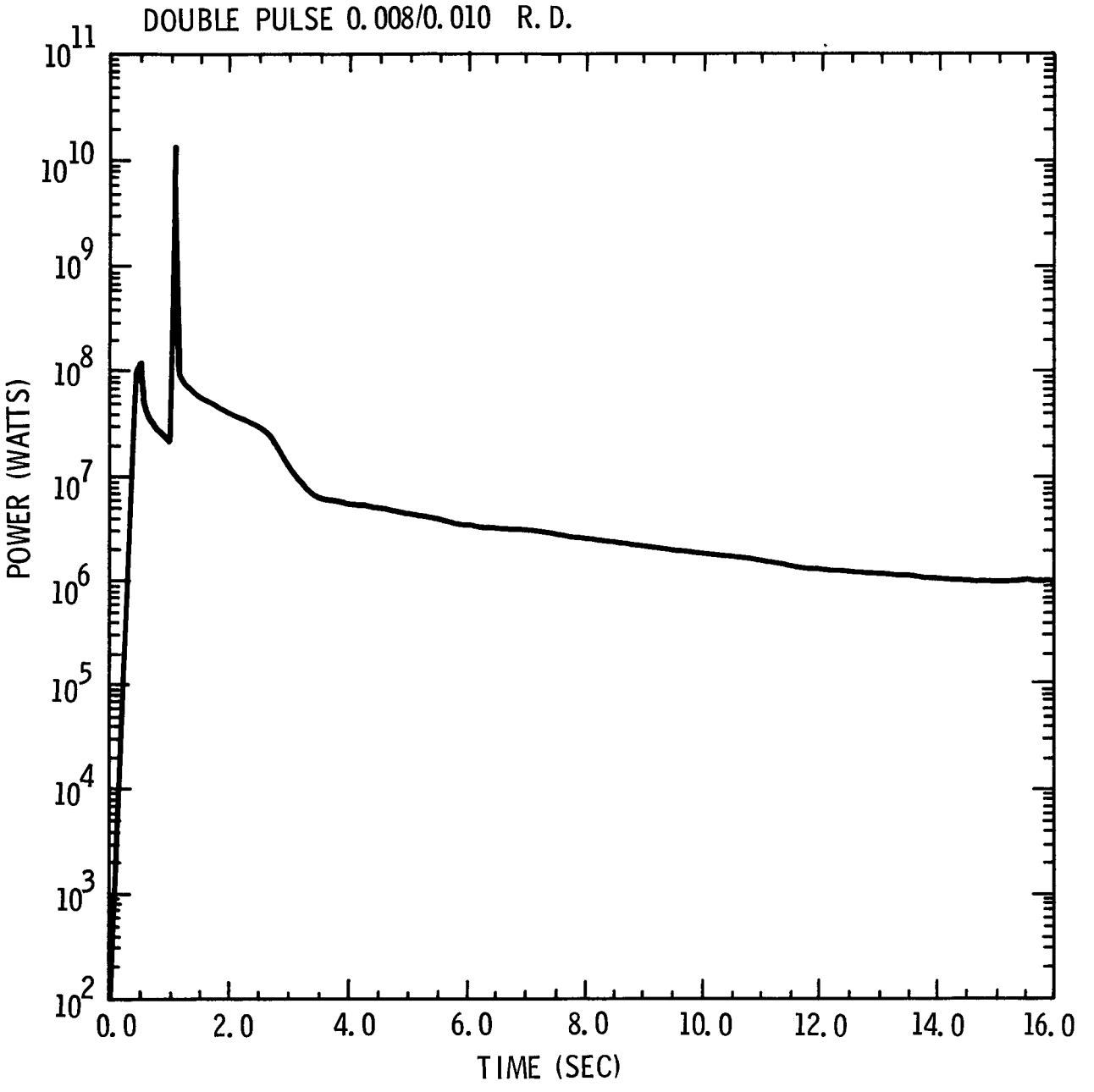

FIGURE 4.6-1. ACPR UPGRADE DOUBLE PULSE. (\$1.1/\$1.37, α_{F2}, PK1D).

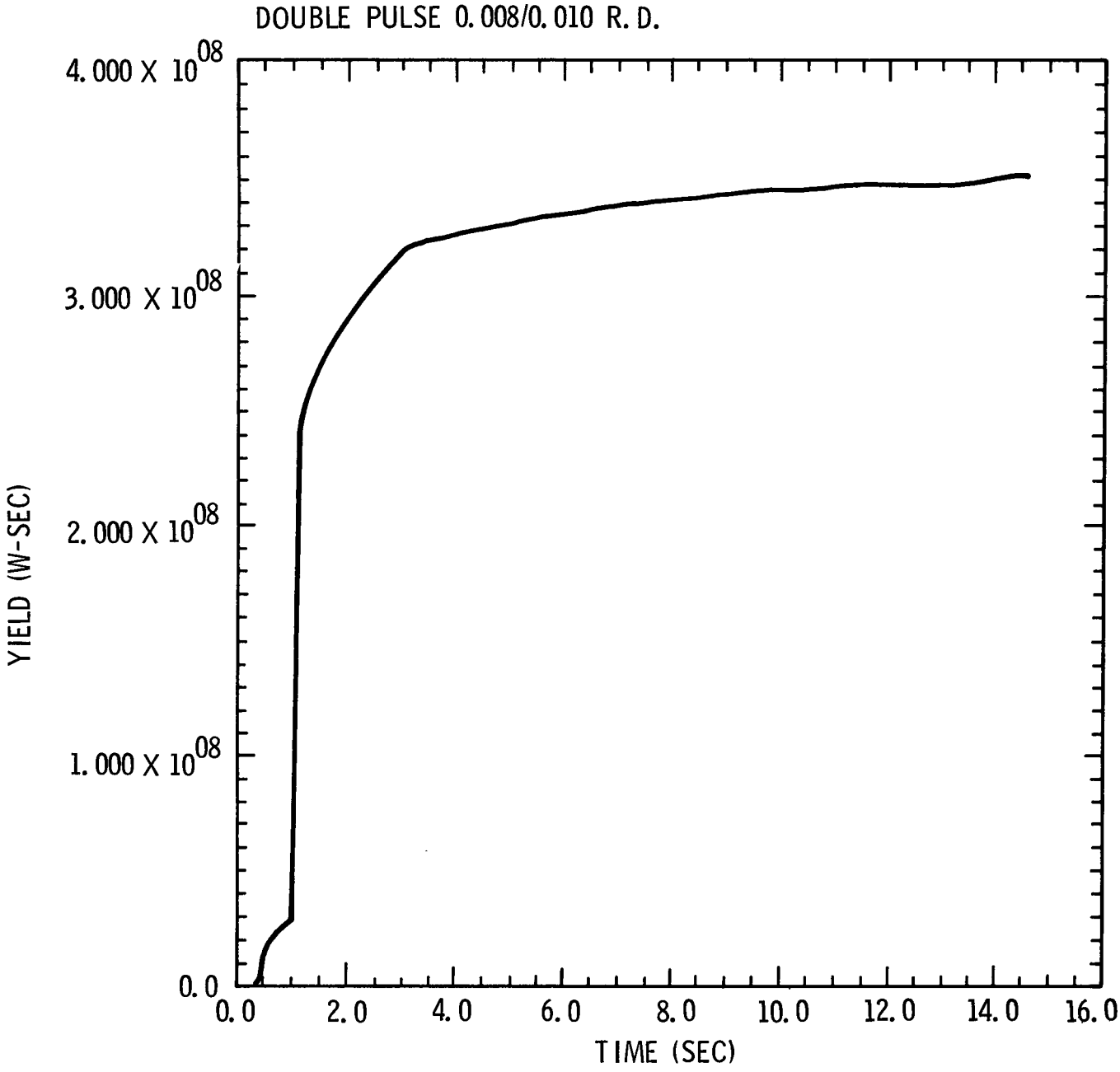

FIGURE 4.6-2. YIELD FOR ACPR UPGRADE DOUBLE PULSE.

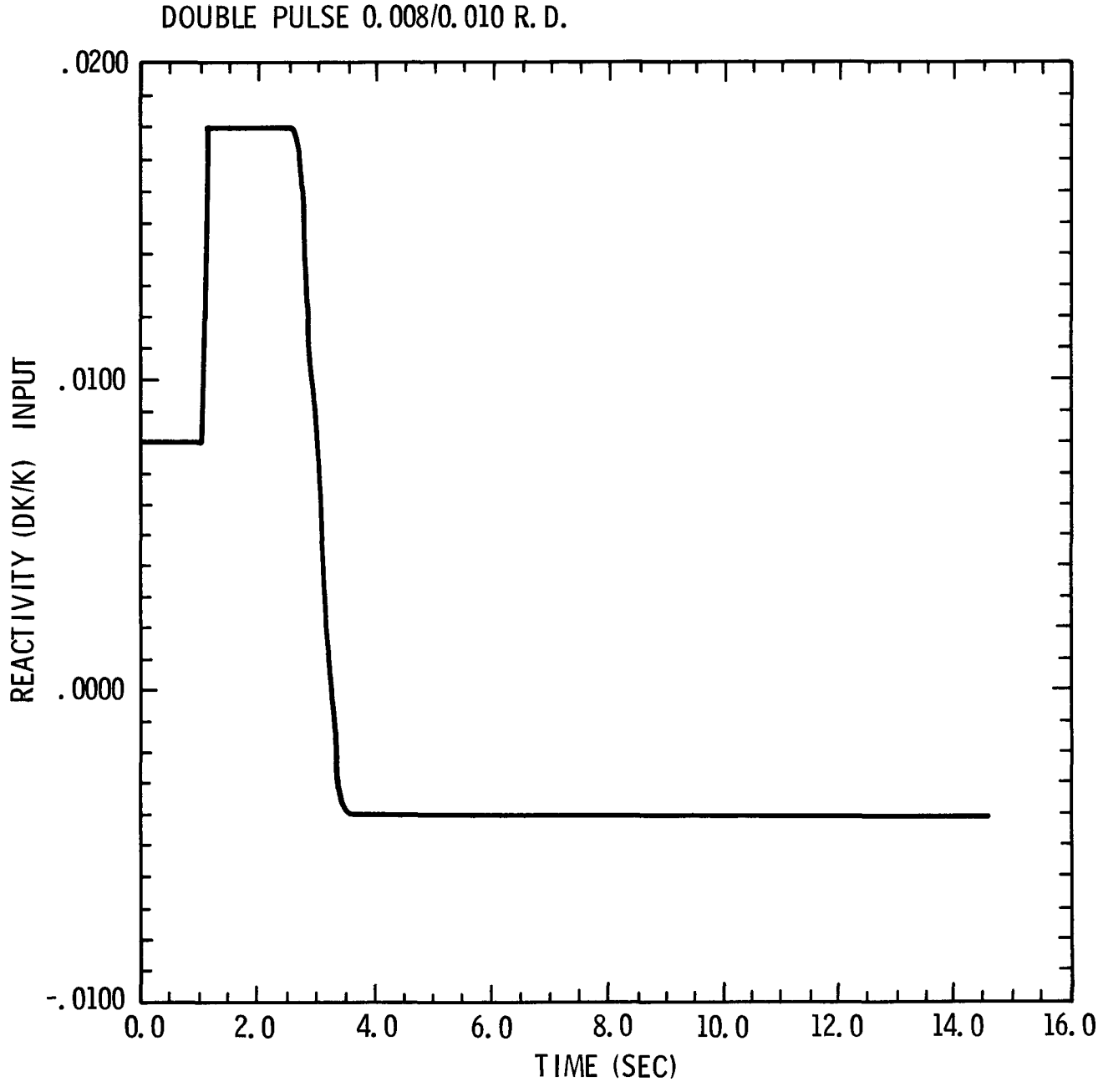

FIGURE 4.6-3. REACTIVITY INSERTION FOR ACPR UPGRADE DOUBLE PULSE.

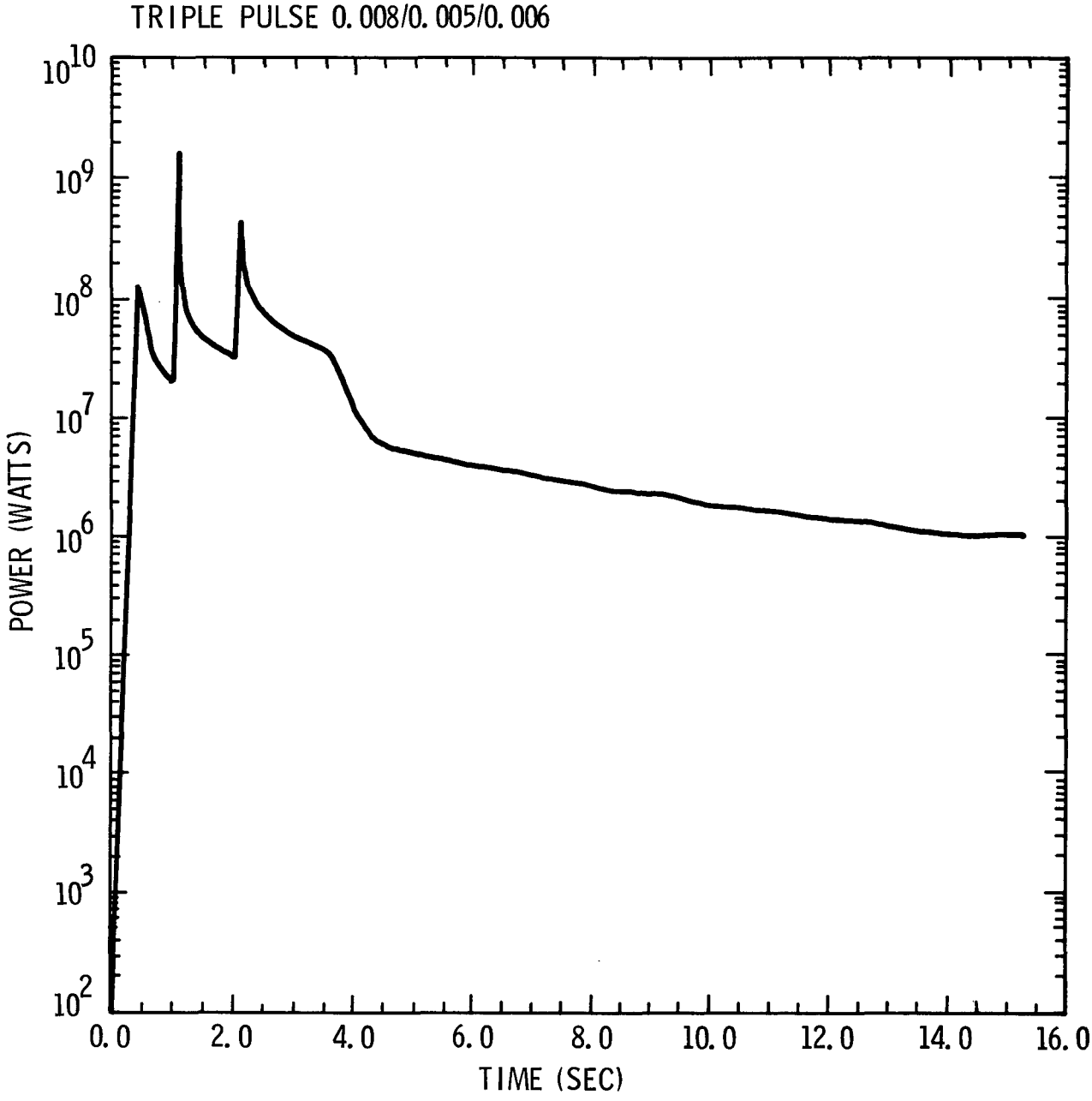

FIGURE 4.6-4. ACPR UPGRADE TRIPLE PULSE. ($1.1/$0.68/$0.82, α_{F2}, PK1D).

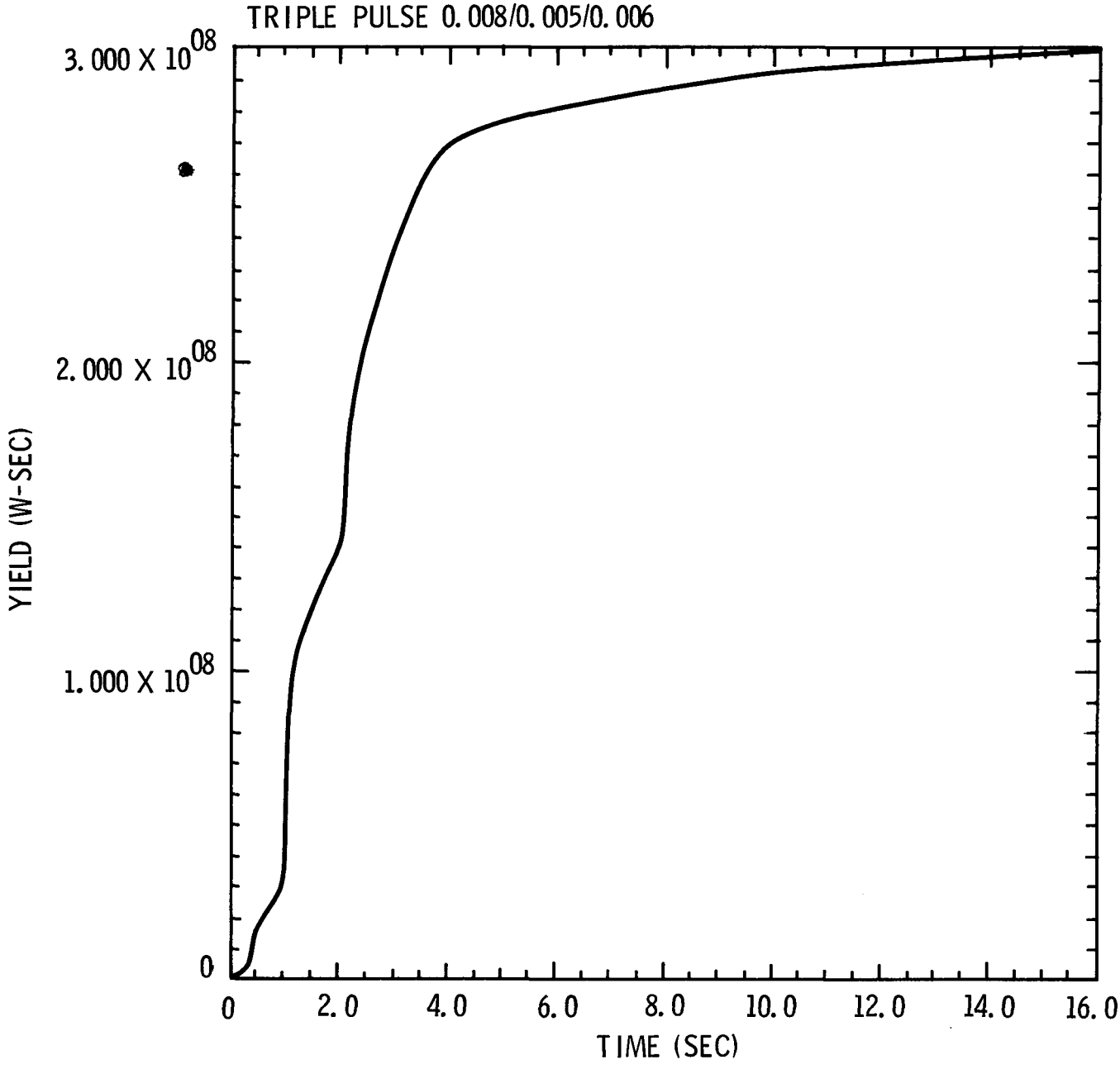

FIGURE 4.6-5. REACTOR YIELD vs TIME FOR ACPR UPGRADE TRIPLE PULSE.

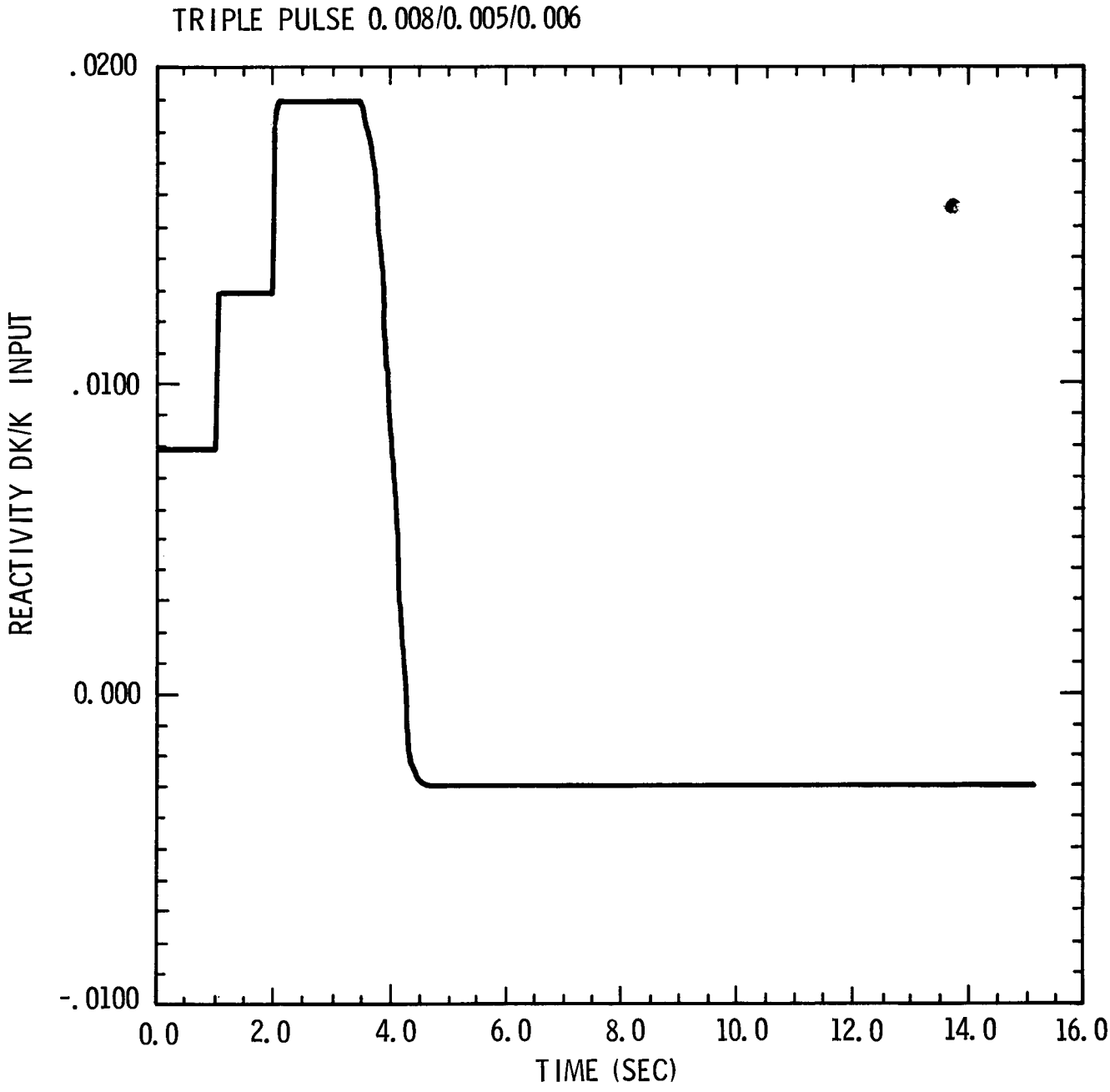

FIGURE 4.6-6. REACTIVITY INSERTION PROGRAM FOR ACPR UPGRADE TRIPLE PULSE.

4.7 Transient Rod Runout

The upgraded ACPR control system allows the transient rods to be either pneumatically ejected in approximately 50 msec or withdrawn manually in approximately 8 sec. The transient rod runout is essentially a sub-transient operation which results in a reduced yield over an extended period of time. The potential exists in the Upgrade control system to program reactivity withdrawal rates to provide a flexible power history for a variety of operations. Initially, however, the transient rods can be withdrawn either as a bank or sequentially one after the other. The transient rod withdrawal rate can be affected by interrupting the withdrawal for limited time durations during the operation.

The yield resulting from a continuous transient rod withdrawal is shown in Figure 4.7-1. The transient bank withdrawal involves sufficient reactivity to provide a small initial pulse, and the continued withdrawal maintains a sufficient power level to provide a very approximate high power square wave operation. The reduction in overall yield from this mode of operation is about 35% in comparison with a single pulse operation. The reactivity program for this illustrative operation is shown in Figure 4.7-2.

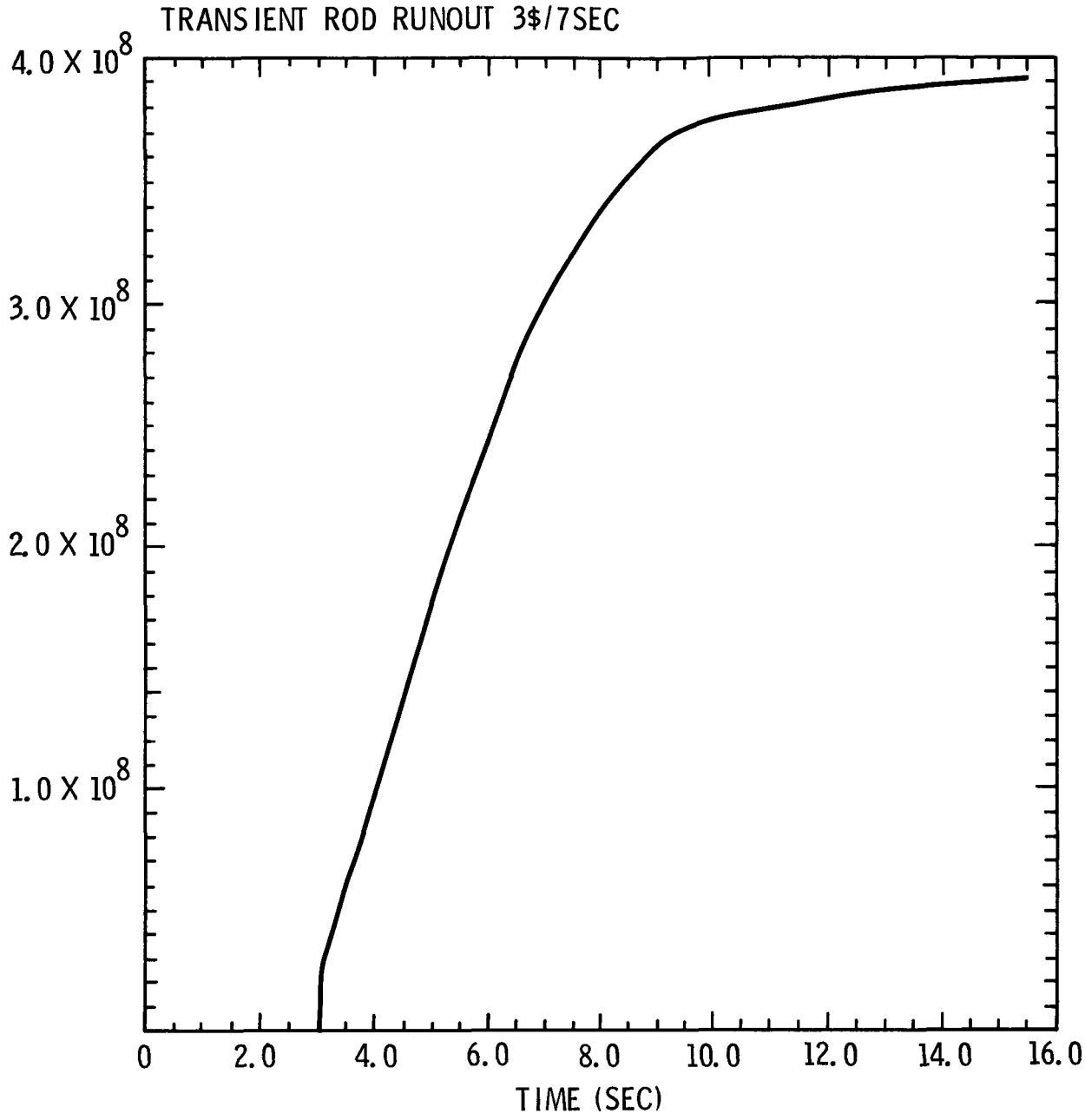

FIGURE 4.7-1. REACTOR YIELD vs TIME FOR TRANSIENT ROD RUNOUT OPERATION. ($3.0, 7 SECOND WITHDRAWL, PK1D, α_{F2}).

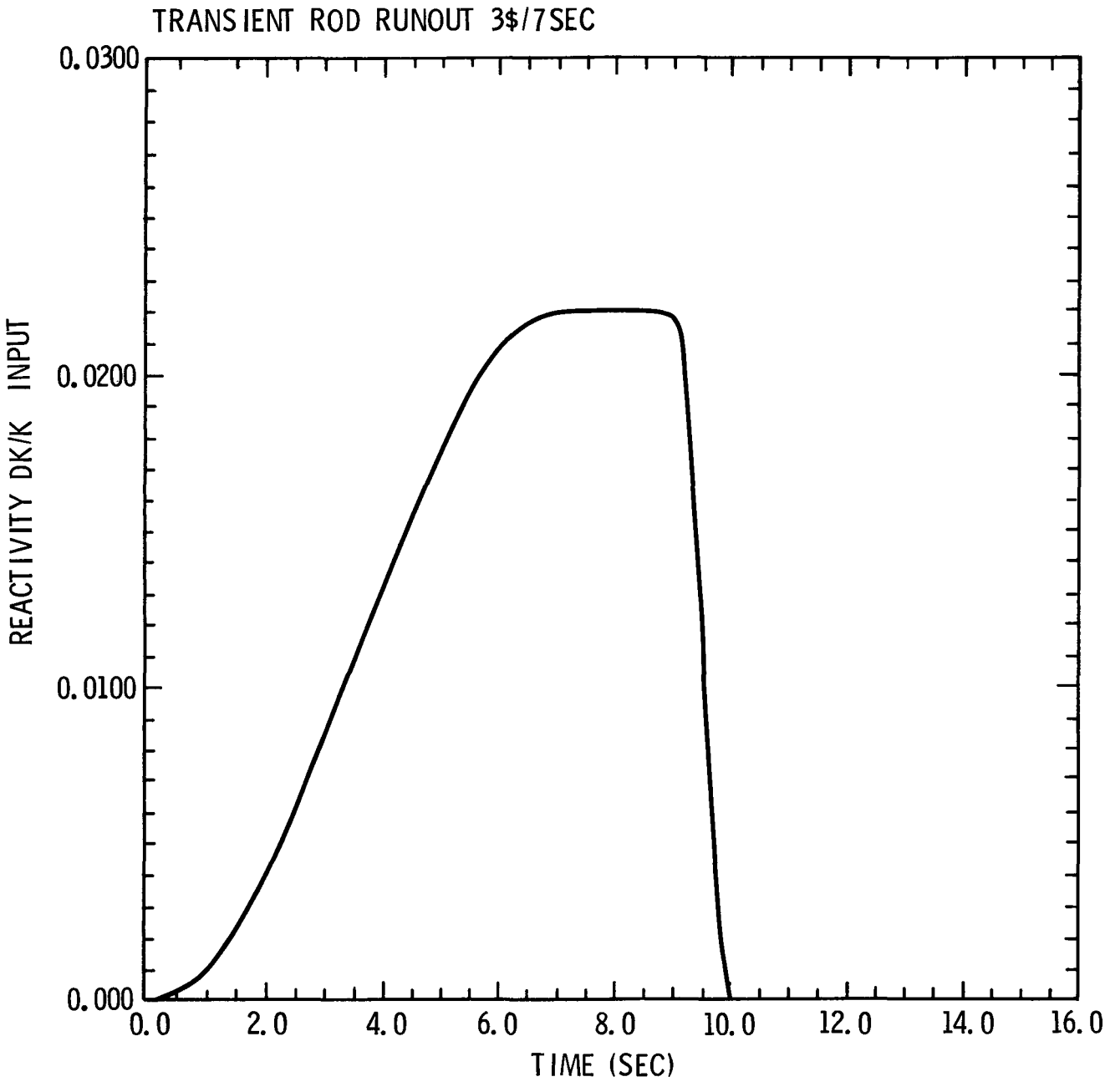

FIGURE 4.7-2. REACTIVITY PROGRAM FOR TRANSIENT ROD RUNOUT OPERATION

4.8 Be Photoneutron Production

The presence of significant quantities of Be in the ACPR Upgrade core will result in the production of photoneutrons due to the (γ-n) reaction of hard fission product γ-rays with Be. The threshold for this reaction in Be is 1.66 MeV with a mean photoneutron half life of 2.31 hrs. The decay of photoneutron activity can be described in terms of 9 precursor groups with effective decay constants as shown in Table 4.8-1.[12] The total photoneutron yield indicated in the table is relatively small, $\Sigma\beta_i$ = 0.00015, in comparison with the delayed neutron fraction from fission, which is 0.0065. This photoneutron yield was derived from measurements of irradiated ^{235}U samples inside Be spheres which represents the most prolific photoneutron production rate. The photoneutron yield in the ACPR Upgrade will be reduced from the above amount due to the fuel volume fraction (0.554), the atom fraction of Be in the fuel (0.48), and leakage from the core boundaries. For scoping purposes the relative yield, or "effectiveness" factor, for the photoneutrons on reactor operation will be apparent primarily in a somewhat slower response to small reactivity changes, (increased asymtotic period waiting times); and as a low yield, long half life delayed neutron group manifesting itself in the tail of transient operations at long times. It does not appear that photoneutron production will strongly affect the conduct of operations but will be observed to some degree as part of the overall system response and pulse repetition rates.

TABLE 4.8-1

GROUP CONSTANTS FOR DELAYED PHOTONEUTRONS FROM Be

Group	Group Half-Life	$\lambda(sec^{-1})$	Group Fraction $j(x10^{-5})$
1	12.8d	6.24×10^{-7}	0.057
2	77.7h	2.48×10^{-6}	0.038
3	12.1h	1.59×10^{-5}	0.260
4	3.11h	6.20×10^{-5}	3.20
5	43.2m	2.67×10^{-4}	0.36
6	15.5m	7.42×10^{-4}	3.68
7	3.2m	3.60×10^{-3}	1.85
8	1.3m	8.85×10^{-3}	3.66
9	0.51m	2.26×10^{-2}	2.07
			Total = 15.175

4.9 Summary

The kinetics calculations summarized in this section are intended to serve as a guideline in anticipating the operational capabilities of the ACPR Upgrade. The parameters used in the kinetics analysis were based on the best available data, but there are obvious uncertainties in key parameters, particularly the temperature coefficient of reactivity. Within these uncertainties, the kinetics of the ACPR Upgrade can be reasonably well defined as being within the range of transient characteristics necessary for flexible reactor operation. Final characterization of core kinetics will be performed during the initial pulse tests when calculated and measured quantities can be compared.

5. CAVITY EXPERIMENT CALCULATIONS

The performance goals of the ACPR Upgrade have generally been stated in terms of cavity fluence for a maximum pulse in comparison with the original ACPR. The primary interest, however, is the energy deposition capability of the ACPR Upgrade for experiment configurations involving fissile materials. Since each fissile experiment must be analyzed and approved before being performed, detailed calculations must be performed in support of specific experiments. The purpose of this section is to establish deposition levels for typical fissile experiments.

5.1 Single Fuel Pin Experiments

Scoping calculations were performed for a single fuel pin with a fueled radius of 0.24 cm and consisting of 20% enriched UO_2. For the purpose of these calculations the containment was a 0.5 cm thick cylinder of stainless steel. Moderator thicknesses of from 0.1 cm to 2.54 cm were used to determine energy deposition as a function of moderator thickness. These calculations were performed with the BeO-1 set of cross sections. The changes due to cross-section set differences appear to be small ($\sim$ 6%) and do not significantly alter the nature of the results.

The results of these calculations are summarized in Figures 5.1-1 and 5.1-2. The maximum and minimum energy depositions are shown in Figure 5.1-1 as a function of moderator thickness. All calculations are based on unit energy release in the core. These results indicate that an average energy deposition of 3000 J/g in a 20% enriched UO_2 fuel pin would require a 400 MJ pulse for

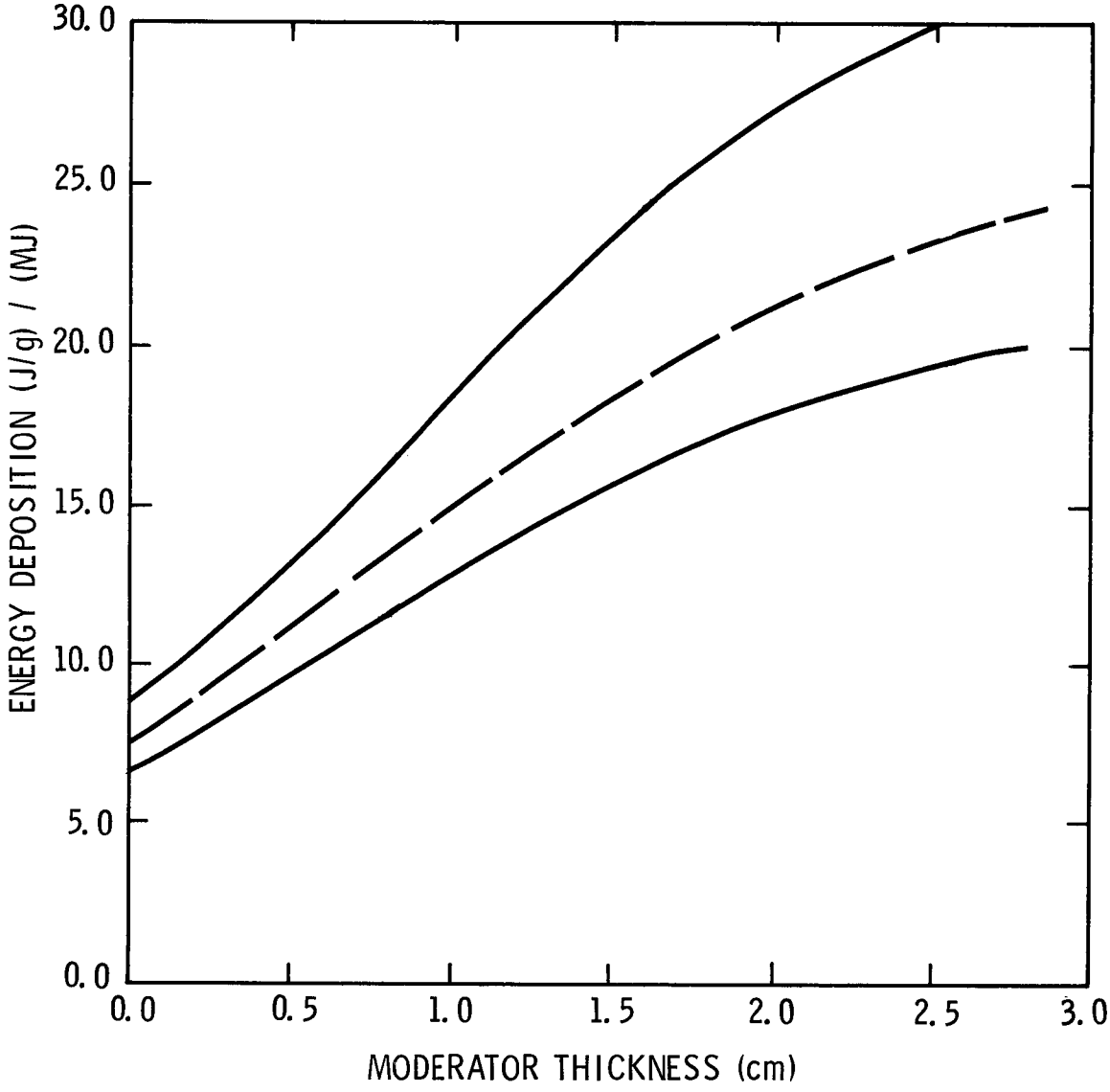

FIGURE 5.1-1.
ENERGY DEPOSITION AT THE AXIAL MIDPLANE IN A 0.24 cm RADIUS, 20% ENRICHED UO_2 FUEL PIN WITH STAINLESS STEEL CONTAINMENT IN ACPR UPGRADE. (S_8, P_1, 9Grp, TWØTRAN).

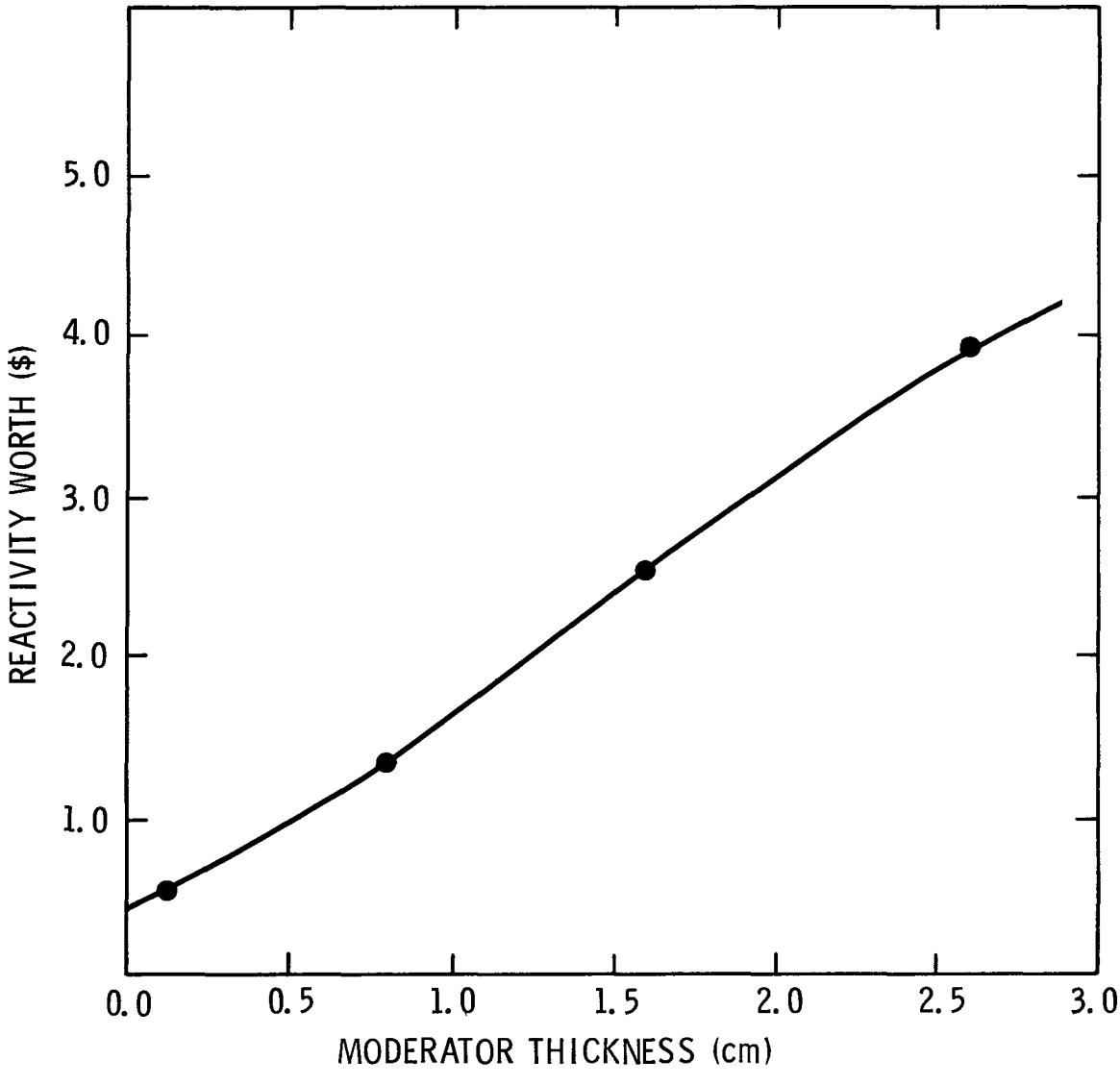

FIGURE 5.1-2.
REACTIVITY WORTH OF AN ILLUSTRATIVE SINGLE PIN EXPERIMENT WITH MODERATOR IN ACPR UPGRADE.

a bare experiment, but only a 125 MJ release for a 2.54 cm thick polyethylene moderator. Energy deposition profiles range from 1.28 to 1.6 for bare to 2.54 cm moderator cases. The details of the profiles and depositions are obviously dependent on the specifics of the experiment, and these figures are intended to serve only as an indication of energy deposition potential.

The reactivity worth of the single-pin experiments in the ACPR Upgrade is shown in Figure 5.1-2. The experiments were modeled as 52 cm in height with no axial reflectors in the cavity. Most of the negative reactivity worth is due to the moderator thermalization causing increased absorption in the cavity liner.

5.2 Multiple Fuel Pin Tests

The increased pulse fluence available with the Upgrade will make it possible to perform multiple fuel pin tests. Calculations have been performed to examine up to 7 fuel pins in a bundle in the ACPR Upgrade. These calculations utilized 20% enriched UO_2 fuel pins of 0.24 cm radius. Seven-pin bundles were modeled both as homogeneous fuel-sodium-steel regions and as discrete fuel pins in a sodium matrix using three-dimensional monte carlo analysis. The monte carlo calculations were performed to provide energy deposition profile information. The results of the homogeneous bundle S_N calculations are given in Figure 5.2-1. Although the average energy deposition in the bundle is assumed to be a reasonable estimate, the central pin energy deposition and profile are both underestimated. This is due to the complete shielding of the central pin in the homogeneous case, while the actual seven pin bundle geometry allows the central pin to be partially unshielded by outer pins. The energy deposition in the larger bundle is reduced from that available in a single pin. These calculations suggest that the central pin energy deposition will be reduced to about 60% of the single pin average energy deposition for the unmoderated case.

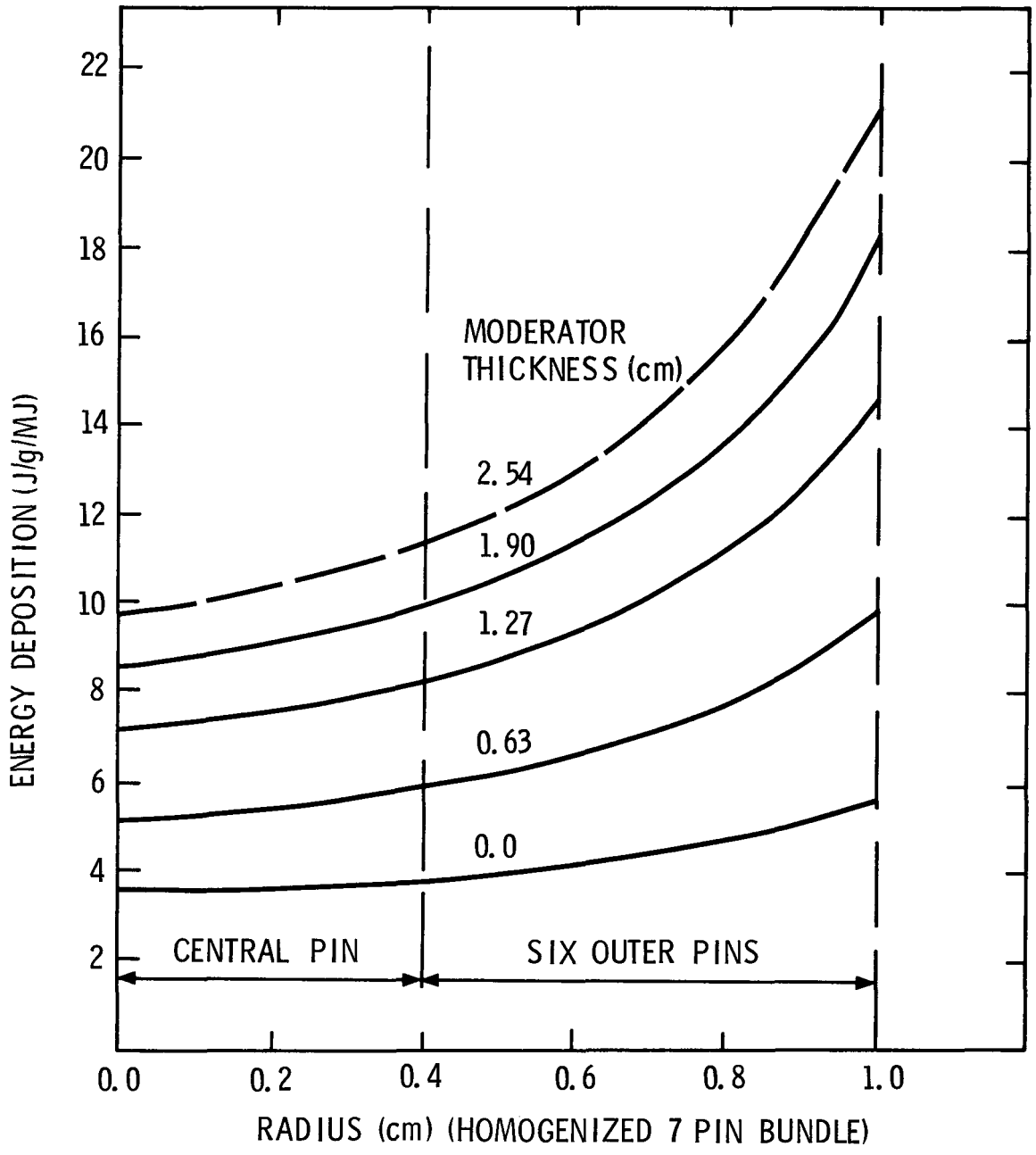

FIGURE 5.2-1. ENERGY DEPOSITION PROFILES IN HOMOGENIZED 7 PIN BUNDLE. (S_4, P_1, 9 Grp, 20% ENRICHED UO_2).

Energy deposition profiles in a discrete pin seven-pin bundle are shown in Figure 5.2-2. These profiles were obtained from a monte carlo model of a seven-pin bundle which models an isotropic cavity surface source in place of the actual reactor model. No azimuthal corrections have been made to account for the inner pin energy distribution due to outer pin shielding. The peak/average factors for the outer pin cases of 0.0, 0.63, and 1.71 cm polyethylene moderator thicknesses are 1.35, 1.40, and 1.51, respectively.

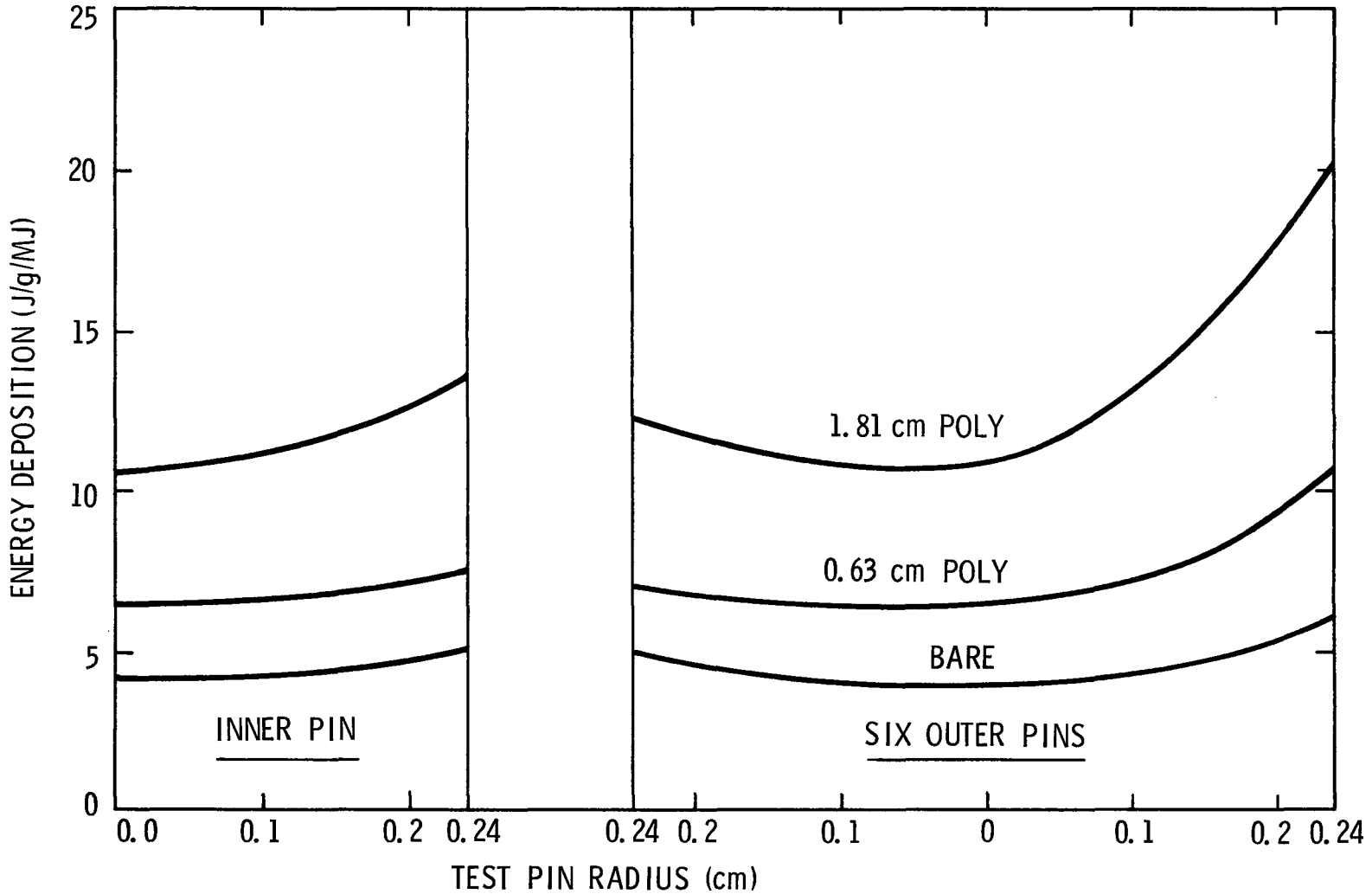

FIGURE 5.2-2. ENERGY DEPOSITION IN SEVEN PIN BUNDLE IN ACPR UPGRADE. (20% ENRICHMENT, MONTE CARLO, 9 GRP.)

5.3 PAHR-Type Experiments

The ACPR has been utilized in the Sandia Advanced Reactor Safety Research Program to conduct studies of the coolability of internally-heated debris beds of UO_2, Na, and steel. The increase in steady-state power allows a considerably higher decay heat simulation than was available with the hydride fueled case. A typical PAHR-type experiment was modeled with an R-Z TWOTRAN calculation and the average bed power is shown as a function of core power in Figure 5.3.1. Although the actual energy deposition and profile obtained in the bed are comparable to the hydride core values per unit power, the additional reactor power available in the Upgrade allows additional neutron filtering to be utilized. These types of experiments will be modeled in more detail as part of the Advanced Reactor Safety Research Program.

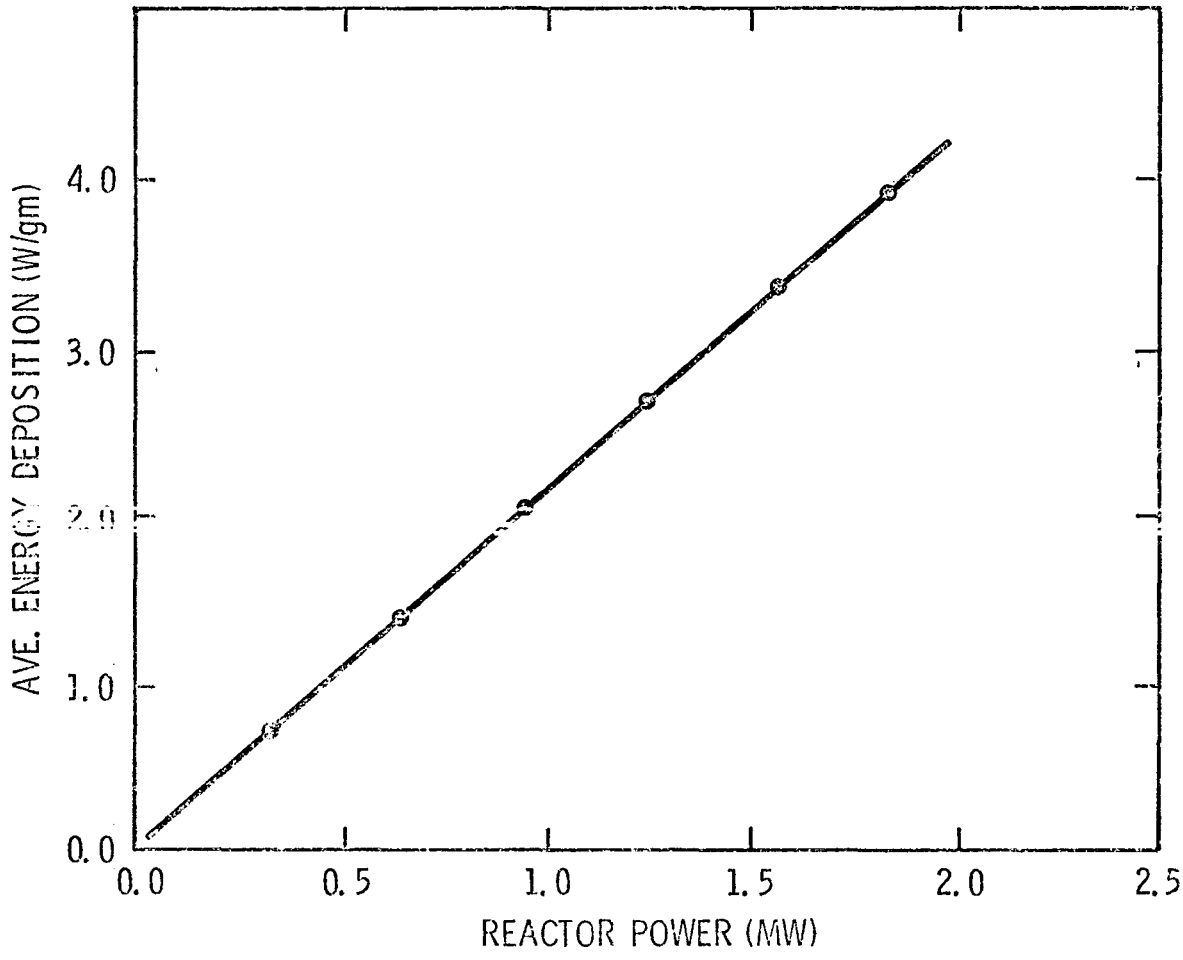

FIGURE 5.3-1. AVERAGE DEBRIS BED ENERGY DEPOSITION IN ACPR UPGRADE. (BORON-TUNGSTEN FILTER, 52% UO_2, 93% ENRICHMENT).

5.4 UO_2-BeO Fuel Pellet Tests

The testing of the UO_2-BeO fuel pellets in the hydride fueled ACPR required an excessive loading of ^{235}U in order to obtain realistic fuel temperatures. Prototypic fuel pellets tested in the hydride fueled ACPR were calculated to reach a peak (adialatic) fuel temperature of only 800°C. It is anticipated that additional fuel tests will be performed in the early stages of operation. A calculation of the prototypic fuel in the ACPR Upgrade produces a peak energy deposition of 12 J/g per MJ energy release in the core. For a 300 MJ pulse, this corresponds to a maximum surface temperature (adiabatic) of 2000°C. The ACPR Upgrade will provide sufficient fluence to subject prototypic pellets to realistic pulse temperatures at relatively low core temperatures.

5.5 External Exposure Capability

The increased fluence available from the ACPR Upgrade will be sufficient to provide some test capabilities in an exposure chamber located outside the core. Although the pulse fluence or flux is reduced in an external location, the increased experiment space available and the possibility of asymmetric heating of certain types of experiments are significant advantages.

Appendix I

ACPR Upgrade Data Sheets

1) Material Assignments and Compositions
2) Fuel Cell Dimensions
3) Grid Configuration

Material Assignments (See Figure 3.1-1)

#1 - R1, R2 - Fuel R4, R5 R6	V_F - $BeO-UO_2$	- 0.554
	V_F - Nb	- 0.032
	V_F - SS	- 0.0392
	V_F - H_2O	- 0.268
#2 - R3 - Fuel	V_F - $BeO-UO_2$	- 0.508
(lower fuel volume fraction in Row 3 accounts for 3 void followers in Row 3)	V_F - Nb	- 0.032
	V_F - SS	- 0.0392
	V_F - H_2O	- 0.268
#3 - Ni Reflector Elements	V_F - Ni	- 0.732
	V_F - H_2O	- 0.268
#4b - Bottom Reflector	V_F - BeO	- 0.448
	V_F - SS	- 0.181
	V_F - H_2O	- 0.268
#4t - Top Reflector	V_F- BeO	- 0.38
	V_F - SS	- 0.154
	V_F - H_2O	- 0.268

#5b Bottom End Fitting	V_F - SS	- 0.225
	V_F - H_2O	- 0.775
#5t Top End Fitting	V_F - SS	- 0.324
	V_F - H_2O	- 0.676
#6b Bottom Grid Plate	V_F - Al	- 0.47
	V_F - SS	- 0.067
	V_F - H_2O	- 0.463
#6t Top Grid Plate	V_F - Al	- 0.207
	V_F - SS	- 0.134
	V_F - H_2O	- 0.659
#7 - Void (Air)	V_F	= 1.0
#8 - SS Liner SS - 304	V_F - SS	= 1.0
#9 - H_2O Annulus Bottom Reflector	V_F - H_2O	= 1.0
#10 - Outer Reflector Region	V_F - H_2O	- 1.0
	V_F - Al	- 0.0
#11 - Top Water Reflector	V_F - H_2O	- 0.83
	V_F - SS	- 0.17
#12 - Cavity Plug Aluminum	V_F - Al - 1.0	- 1.0

Fuel Materials

Enrichment	-	35%
w/o UO_2 in BeO	-	21.5 w/o
BeO	-	3.01 g/cc
UO_2	-	10.9 g/cc
Percent of Theoretical Density	-	99%

Stainless Steel

N_{Fe}	-	0.061×10^{-24} atoms/cc
N_{Cr}	-	0.0174×10^{-24} atoms/cc
N_{Ni}	-	0.0071×10^{-24} atoms/cc

ACPR Upgrade - Control Element Data

Fuel Element Data

Control Element Data

Element	Number	Location	Follower	Poison Radius
Control	6	3rd Row - Hex. Corner	Fuel	1.46 cm
Safety	2	3rd Row - Hex. Flat	Fuel	0.57 cm
Transient	3	3rd Row - Hex. Flat	Void	0.57 cm

Core Loading -- 200 Elements (Nominal)

200 Element Core -- Consists of:

a) 3 Transient Rod Void Followers

b) 2 Safety Rod Fuel Followers

c) 6 Control Rod Fuel Followers

d) 189 Fuel Elements

e) 55 Ni-Reflector Elements Surrounding Fuel

FIGURE I-1. FUEL CELL DIMENSIONS

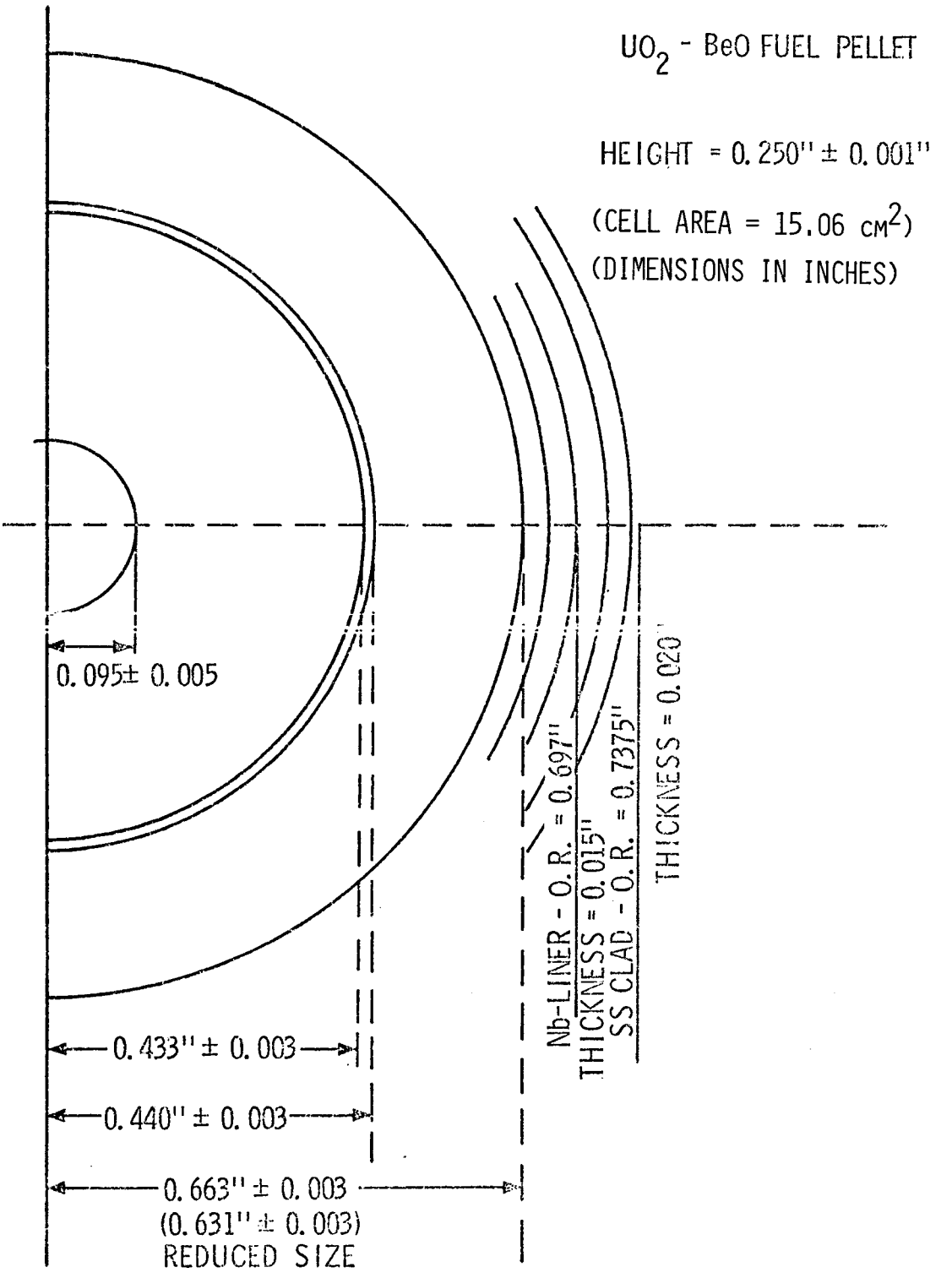

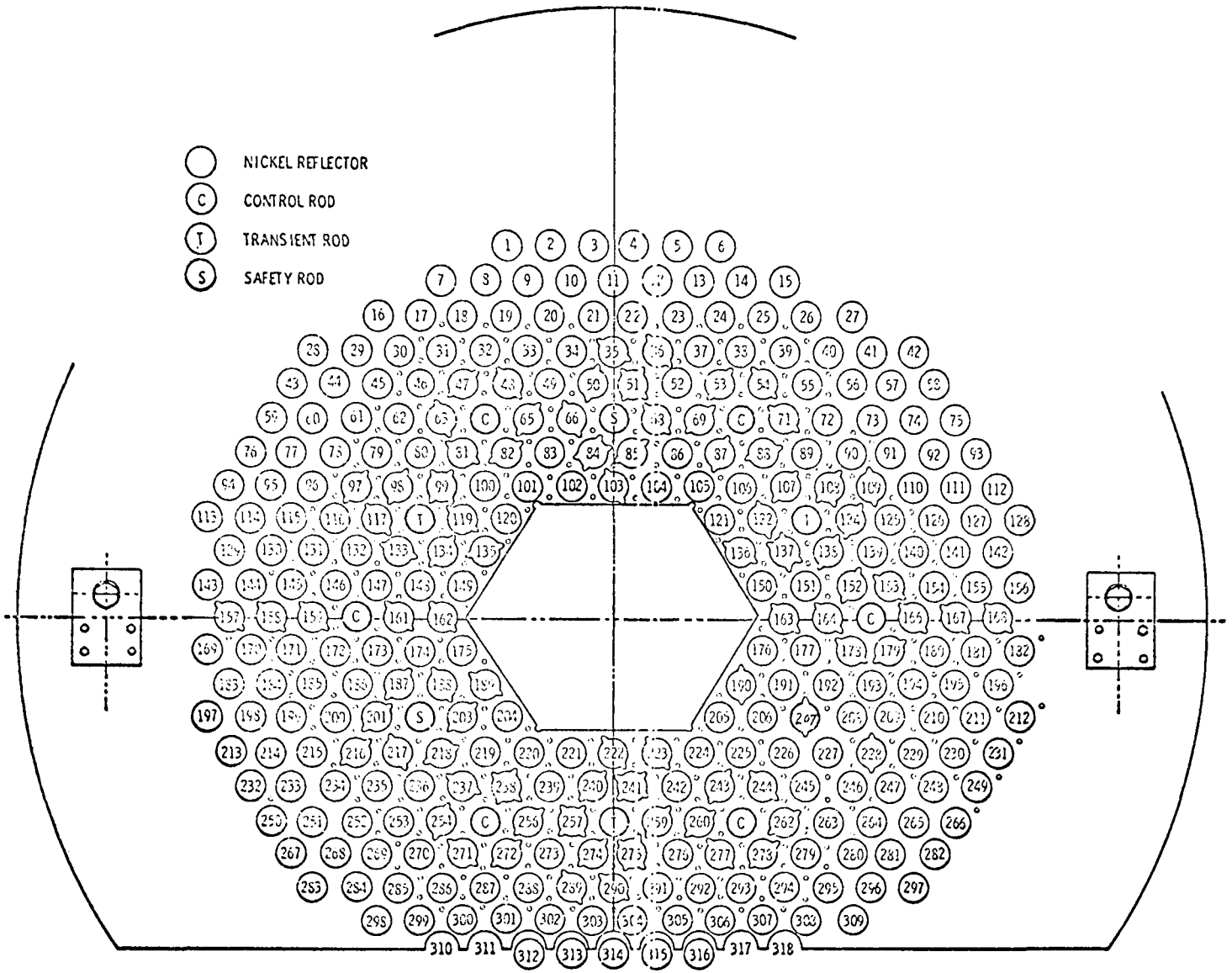

FIGURE I-2. ACPR UPGRADE CORE GRIDPLATE.

Appendix II

Approach to Critical Experiment

The approach to critical experiment for the ACPR Upgrade will be performed with a centrally-located neutron source and fission detectors located at positions both within and outside of the final configuration fuel boundary. Fuel elements will be loaded into positions of highest worth (inner row on hexagonal flats) first and will sequentially be loaded into positions of lower worth (outer row hexagonal corners). The initial fuel loading configuration will not include the Ni-reflector elements surrounding the outer row of fuel. The absence of the Ni-reflector elements in the initial experiment will perturb the overall core fission density distribution, excess reactivity, and kinetic parameters. Since only low-power steady-state operations of a preliminary nature are to be performed in this configuration, detailed reactor physics calculations were not performed for the initial configuration. Calculations were performed to evaluate k_{eff} as a function of core size and control rod worths for water-reflected configurations. The table below summarizes the quantities examined for the initial core loading.

Initial Core Loading Parameters

Parameter	Core Configuration		Value
k_{eff}	125 elements (H_2O Reflector)		0.952
k_{eff}	149 calculated 155* corrected		1.003
TR Bank Worth	H_2O Reflector - 150	+7%	$ 3.00
RR Bank Worth	H_2O Reflector - 150	-4%	$10.50
Element Worth Row 5	H_2O Reflector		$ 0.23
Element Worth Row 5	Ni Reflector		$ 0.28

*See Appendix 3.

Appendix III

During the course of the ACPR Upgrade design calculations, several types of calculations were performed for the original ACPR which could be compared to existing calculations or measured data. This appendix summarizes the results of these calculations in order to establish the validity of the calculational methods used in predicting ACPR Upgrade performance values and physics characteristics. The reactor parameters of primary interest were the following:

1. Eigenvalue (Excess Reactivity) - S_N, MC
2. Pulse Performance and Fission Peaking Factors - S_N
3. Temperature Coefficient of Reactivity - S_N
4. Neutron Generation Time and Energy Spectrum - S_N, MC
5. Control Rod Worth - MC

The cross sections used in these comparative calculations were generated from ENDF/B-III or IV using AMPX. In some instances, there were non-negligable modeling differences in the calculation of ACPR and ACPR Upgrade quantities which makes direct comparisons more difficult. In these cases an attempt has been made to estimate the magnitude and direction of the change in calculated quantities which might be anticipated from these modeling differences.

Eigenvalue Calculations

Effective multiplication constants were determined for the hydride-fueled ACPR using both discrete ordinates and monte carlo

methods. The irregular loading of the outer region of ACPR was not modeled exactly, and first order corrections were applied to existing models to estimate the core multiplication. The S_N method results in a k_{eff} of 1.075 for an S_8, P_1, 18-energy group problem in R-Z geometry. The monte carlo analysis gives a value of 1.09 for a hexagonal, 9-group problem. Older cross section sets using KENO-II resulted in lower eigenvalues ($\simeq 1.04$). The measured excess reactivity for the 156-element core was about \$8.0, or a k_{eff} of 1.062. In arriving at calculated values, the effects of central rods above the core, cavity reflector plugs, and fission product poisons were not included. The analytic methods and cross section data used for the hydride-fueled ACPR estimates the effective multiplication constant to be about 2% higher than the measured value. Modeling approximations of the irregular core and cross section uncertainties were considered to be the primary source of uncertainty. Although systematic corrections were not made to Upgrade calculations based on these results, estimates of critical size were biased by 2%.

Pulse Performance Estimates

Estimates of the neutron fluence for a given energy release in the core were obtained from S_4 and S_8, 9 energy group, discrete ordinates calculations. In terms of fluence (n/cm^2) per unit energy release (MJ), the following values were obtained:

T(°K)	S_4 $\frac{n/cm^2}{MJ}$	S_8 $\frac{n/cm^2}{MJ}$
300°K	1.43×10^{13}	1.64×10^{13}
800°K	1.57×10^{13}	1.78×10^{13}

The highest fluence estimate obtainable from these calculations for a 108 MJ release is 1.85×10^{15} n/cm^2. Calculations of certain fueled experiments have indicated a fluence approximately 5 to 10% higher than this value. It is not certain whether this difference is due to approximations in the analytic model, or uncertainties in the actual energy release in the core. The average core temperature rise resulting from a 108 MJ release is 580°C. The least severe peaking factors calculated for ACPR occur with all control elements withdrawn. Using this overall core peak-to-average value of 1.82, the maximum temperature rise in the core is calculated to be 900°C. If a more severe cell peaking factor of 2.2 is employed, accounting for a fuel cell adjacent a transient rod void, the estimated peak adiabatic temperature rise in the core is 1020°C.

Prompt Temperature Coefficient

The prompt temperature coefficient of reactivity for ACPR was calculated using temperature-dependent cross-section sets in TWOTRAN. The ENDF/B ZrH thermal scattering kernal was used to form hydride cross sections. The average fuel temperature coefficient over the range of 27°C to 527°C was calculated to

be -1.07¢/°C. The generally accepted value of the total prompt coefficient for the ACPR was -1.25¢/°C, a value approximately 15% higher. Only a weak temperature dependence is observed with the hydride temperature coefficient. Since the temperature feedback is strongly dependent on the hydride thermal scattering kernal, it is possible that the difference between measured and calculated values is due to the U-$ZrH_{1.62}$ cross sections. The Upgrade fuel temperature coefficient is not as strongly dependent on the thermal scattering kernal, but is dominated by Doppler broadening of ^{238}U resonances. It was not assumed that the same calculational procedure would result in an underestimate of the ACPR temperature coefficient.

Neutron Generation Time and Spectrum

The ACPR neutron generation time was calculated using KENO-II. Both calculated and measured values of the neutron generation time are 34 usec. The calculated neutron energy spectrum for ACPR was characterized as 52% above 10 KeV in the cavity.

Control Rod Calculations

A comparison calculation was performed with MORSE to evaluate the regulating rod bank worth. The core was modeled with 165 element positions, with transient rod positions voided, and with an axial H_2O reflector region instead of the actual graphite water reflector of the ACPR. The calculated value of the six regulating rods modeled with air followers was $6.1. The measured value of six fuel followers vs. air followers is approximately $0.40/rod. These results indicate a regulating rod bank worth of $8.50.

Considering the modeling approximations involved, the above value is probably fortuitiously close to the actual value of $8.4. The results do indicate, however, that the monte carlo model provides a reasonable estimate of the regulating rod bank worth for the ACPR Upgrade.

Fissile Experiments

Survey calculations were performed to compare calculated energy depositions in PAHR and PBE experiments to measured values. Using an S_4, P_1 9-group, R-Z geometry TWOTRAN model, the energy deposition in a D' series PAHR experiment was calculated to be 1.21 watts/gm of UO_2 at 600 kW. The same model was employed to model a 20% enriched UO_2 single pin with 1" of polyethylene moderator. The calculated peak value for the energy deposition is 2720 J/g, as compared to a measured value of 2900 J/gm.[13]

In all cases, uncertainties in both modeling and measurement would suggest the calculated vs measured values agree well within these uncertainties. The general agreement of fissile experiments with calculated values also gives support to pulse performance estimates given previously since all cases were normalized to a 108 MW sec yield in ACPR.

REFERENCES

1. Experimental Fast Reactor Safety Research Program - Detailed Work Plan - Draft, SAND74-0384, Sandia Laboratories, Albuquerque, NM, March 1975.

2. P. S. Pickard and J. P. Odom, Two-Region Core Design Concepts for the Upgrade of the Annular Core Pulse Reactor, SAND78-2145, Sandia National Laboratories, Albuquerque, NM, May 1979.

3. Annular Core Pulse Reactor Upgrade Quarterly Report, January-March 1977, SAND77-0610, Sandia National Laboratories, Albuquerque, NM, June 1977.

4. N. M. Greene et al., AMPX: A Modular Code System for Generating Coupled Multigroup Neutron-Gamma Libraries from ENDF/B, ORNL-TM-3706, Oak Ridge National Laboratory, Oak Ridge, TN, March 1976.

5. P. S. Pickard and W. H. Vandevender, Users' Manual for the CDC-6600 Version of AMPX, SAND77-1148, Sandia National Laboratories, Albuquerque, NM, November 1977.

6. K. D. Lathrop, DTF-IV, A Fortran Program for Solving the Multigroup Transport Equation with Anisotropic Scattering, LA-3373, Los Alamos Scientific Laboratories, Los Alamos, NM, November 1965.

7. K. D. Lathrop and F. W. Brinkley, Theory and Use of the General Geometry TWOTRAN Program, LA-4432, Los Alamos Scientific Laboratories, Los Alamos NM, April 1970.

8. G. E. Whitesides and N. F. Cross, KENO-IV Multigroup Monte Carlo Criticality Program, CTC-5, Union Carbide Corporation, Nuclear Division, Oak Ridge, TN, 1969.

9. M. B. Emmett, The MORSE Monte Carlo Radiation Transport Code System, ORNL-4972, Oak Ridge National Laboratory, Oak Ridge, TN, February 1975.

10. P. S. Pickard and J. P. Odom, Sandia Reactor Kinetics Codes: SAK and PKlD, SAND77-1211, Sandia National Laboratories, Albuquerque, NM, January 1978.

11. Sandia Annular Core Pulse Reactor (ACPR) Upgrade Safety Analysis Report, SAND77-0208, Sandia National Laboratories, Albuquerque, NM, January 1977.

12. G. R. Keepin, Physics of Nuclear Kinetics, Addison-Wesley Publishing Co. 1965.

13. Advanced Reactor Safety Research Quarterly Report, April-June 1978, SAND78-2001, Sandia National Laboratories, Albuquerque, NM, May 1979.

DO NOT MICROFICH

Distribution:

US NRC Distribution Contractor (CDSI) (155 copies)
7300 Pearl Street
Bethesda, MD 20014
130 copies for AN
25 copies for NTIS

4400 A. W. Snyder
4410 D. J. McCloskey
4412 G. J. Kolb (5)
4413 N. R. Ortiz
4415 D. R. Strip
4420 J. V. Walker
4420 D. Soblick
4421 K. R. Boldt
4421 J. T. Hitchcock
4423 P. S. Pickard (5)
4423 A. C. Marshall
4424 J. P. Odom
4450 J. A. Reuscher
4451 T. R. Schmidt
4451 B. F. Estes
4451 C. D. Harmon
4451 V. E. James
4451 F. M. Morris
4451 F. G. Trussel
4451 J. L. Zubersky
4452 M. F. Aker
4452 J. Bryson
4452 D. McKeon
4452 J. S. Philbin
8214 M. A. Pound
3141 L. J. Erickson (5)
3151 W. L. Garner (3)

★U.S. GOVERNMENT PRINTING OFFICE: 1982-0-576-021/563